Pharmacological hallmarks of allostery at the M4 muscarinic receptor elucidated through structure and dynamics

Ziva Vuckovic[1,7], Jinan Wang[2,7], Vi Pham[1,7], Jesse I. Mobbs[1,3,7], Matthew J. Belousoff[1,3], Apurba Bhattarai[2], Wessel A.C. Burger[1,3], Geoff Thompson[1], Mahmuda Yeasmin[1], Katie Leach[1,3], Emma T. van der Westhuizen[1], Elham Khajehali[1], Yi-Lynn Liang[1], Alisa Glukhova[1,3], Denise Wootten[1,3], Craig W. Lindsley[4], Andrew B. Tobin[5], Patrick M. Sexton[1,3], Radostin Danev[6], Celine Valant[1*], Yinglong Miao[2*], Arthur Christopoulos[1,3*], and David M. Thal[1,3*]

[1]Drug Discovery Biology, Monash Institute of Pharmaceutical Sciences, Monash University, Parkville, VIC 3052, Australia;
[2]Center for Computational Biology and Department of Molecular Biosciences, University of Kansas, Lawrence, KS 66045, USA;
[3]ARC Centre for Cryo-electron Microscopy of Membrane Proteins, Monash Institute of Pharmaceutical Sciences, Monash University, Parkville, VIC 3052, Australia;
[4]Department of Pharmacology, Warren Center for Neuroscience Drug Discovery and Department of Chemistry, Warren Center for Neuroscience Drug Discovery, Vanderbilt University, Nashville, Tennessee 37232, USA;
[5]The Centre for Translational Pharmacology, Institute of Molecular, Cell and Systems Biology, College of Medical, Veterinary and Life Sciences, University of Glasgow, Glasgow G12 8QQ, United Kingdom;
[6]Graduate School of Medicine, University of Tokyo, N415, 7-3-1 Hongo, Bunkyo-ku, 113-0033 Tokyo, Japan
[7]Authors contributed equally

*Correspondence: celine.valant@monash.edu (C.V.), miao@ku.edu (Y.M.), arthur.christopoulos@monash.edu (A.C.), david.thal@monash.edu (D.M.T.)

Abstract

Allosteric modulation of G protein-coupled receptors (GPCRs) is a major paradigm in drug discovery. Despite decades of research, a molecular level understanding of the general principals that govern the myriad pharmacological effects exerted by GPCR allosteric modulators remains limited. The M_4 muscarinic acetylcholine receptor (M_4 mAChR) is a well-validated and clinically relevant allosteric drug target for several major psychiatric and cognitive disorders. Here, we present high-resolution cryo-electron microscopy structures of the M_4 mAChR bound to a cognate G_{i1} protein and the high affinity agonist, iperoxo, in the absence and presence of two different positive allosteric modulators, LY2033298 or VU0467154. We have also determined the structure of the M_4 mAChR-G_{i1} complex bound to its endogenous agonist, acetylcholine (ACh). Structural comparisons, together with molecular dynamics, mutagenesis, and pharmacological validations, have provided in-depth insights into the role of structure and dynamics in orthosteric and allosteric ligand binding, global mechanisms of receptor activation, cooperativity, probe-dependence, and species variability; all key hallmarks underpinning contemporary GPCR drug discovery.

Introduction

Over the past 40 years, there have been major advances to the analytical methods that allow for the quantitative determination of the pharmacological parameters that characterise G protein-coupled receptor (GPCR) signaling and allosteric modulation (**Figure 1A,B**). These analytical methods are based on the operational model of agonism (Black and Leff, 1983) and have been extended or modified to account for allosteric modulation (Leach et al., 2007), biased agonism (Kenakin, 2012), and even biased allosteric modulation (Slosky et al., 2021). Collectively, these models and subsequent key parameters (**Figure 1B**) are used to guide allosteric drug screening, selectivity, efficacy and ultimately, clinical utility, and provide the foundation for modern GPCR drug discovery (Wootten et al., 2013). Yet, a systematic understanding of how these pharmacological parameters relate to the molecular structure and dynamics of GPCRs remains elusive.

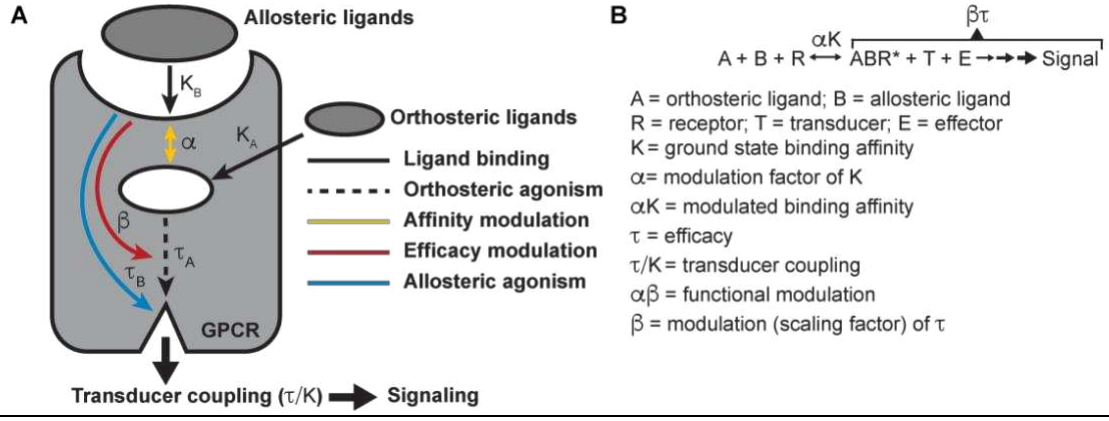

Figure 1. Pharmacological characterization of the PAMs, LY298 and VU154, with ACh and Ipx. (**A**) Schematic of the pharmacological parameters that define effects of orthosteric and allosteric ligands on a GPCR. (**B**) A simplified schematic diagram of the Black-Leff operational model to quantify agonism, allosteric, and agonist bias with pharmacological parameters defined (Black and Leff, 1983).

The muscarinic acetylcholine receptors (mAChRs) are an important family of five Class A GPCRs that have long served as model systems for understanding GPCR allostery (Conn et al., 2009). The mAChRs have been notoriously difficult to exploit therapeutically and selectively due to high sequence conservation within their orthosteric binding domains (Burger et al., 2018). However, the discovery of highly selective positive allosteric modulators (PAMs) for some mAChR subtypes has paved the way for novel approaches to exploit these high value

drug targets (Chan et al., 2008; Gentry et al., 2014; Marlo et al., 2009). X-ray crystallography and cryo-electron microscopy (cryo-EM) have been used to determine inactive state structures for all five mAChR subtypes (Haga et al., 2012; Kruse et al., 2012; Thal et al., 2016; Vuckovic et al., 2019) and active state structures of the M_1 and M_2 mAChRs (Maeda et al., 2019). For the M_2 mAChR this includes structures co-bound with the high-affinity agonist iperoxo (Ipx) and the PAM LY2119620 in complex with a G protein mimetic nanobody (Kruse et al., 2013) and the transducers G_o (Maeda et al., 2019) and β-arrestin1 (Staus et al., 2020). These M_2 mAChR structures were foundational to validating the canonical mAChR allosteric site but are limited to only one agonist (iperoxo) and one PAM (LY2119620) and do not account for the vast pharmacological properties of ligands targeting mAChRs. A recent nuclear magnetic resonance (NMR) study at the M_2 mAChR revealed differences in the conformational landscape of the M_2 mAChR when bound to different agonists, but no clear link was established between the properties of the ligands and the conformational states of the receptor (Xu et al., 2019).

The M_4 mAChR subtype is of major therapeutic interest due to its expression in regions of the brain that are rich in dopamine and dopamine receptors, where it regulates dopaminergic neurons involved in cognition, psychosis, and addiction (Bymaster et al., 2003; Dencker et al., 2011; Foster et al., 2016; Tzavara et al., 2004). Importantly, these findings have been supported by studies utilizing novel PAMs that are highly selective for the M_4 mAChR (Bubser et al., 2014; Chan et al., 2008; Leach et al., 2010; Suratman et al., 2011). Among these, LY2033298 (LY298) was the first reported highly selective PAM of the M_4 mAChR and displayed antipsychotic efficacy in a preclinical animal model of schizophrenia (Chan et al., 2008). Despite LY298 being one of the best characterized M_4 mAChR PAMs, its therapeutic potential has been limited by numerous factors including its chemical scaffold, which has been difficult to optimize with respect to its molecular allosteric parameters (**Figure 1**) and variability of response between species (Suratman et al., 2011; Wood et al., 2017a). In the search for better chemical scaffolds, the PAM, VU0467154 (VU154), was subsequently discovered. VU154 showed robust efficacy in preclinical rodent models, however, it also exhibited species selectivity that prevented its clinical translation (Bubser et al., 2014). Collectively, LY298 and VU154 are exemplar tool molecules that highlight the promises and

the challenges in understanding and optimising allosteric GPCR drug activity for translational and clinical applications.

Herein, by examining the pharmacology of the PAMs LY298 and VU154 with the agonists ACh and Ipx across radioligand binding assays and two different signaling assays and analysing these results with modern analytical methods, we determined the key parameters that describe signaling and allostery for these ligands. To investigate a structural basis for these pharmacological parameters, we used cryo-electron microscopy (cryo-EM) to determine high-resolution structures of the M_4 mAChR in complex with a cognate G_{i1} heterotrimer and ACh and Ipx. We also determined structures of receptor complexes with Ipx co-bound with the PAMs LY298 or VU154. Moreover, because protein allostery is a dynamic process (Changeux and Christopoulos, 2016), we performed all-atom simulations using the Gaussian accelerated molecular dynamics (GaMD) enhanced sampling method (Draper-Joyce et al., 2021; Miao et al., 2015; Wang et al., 2021a) on the M_4 mAChR using the cryo-EM structures. The structures and GaMD simulations, in combination with detailed molecular pharmacology and receptor mutagenesis experiments, provide fundamental insights into the molecular mechanisms underpinning the hallmarks of GPCR allostery. To further validate these findings, we investigated the differences in the selectivity of VU154 between the human and mouse receptors and established a structural basis for species selectivity. Collectively, these results will enable future GPCR drug discovery research and potentially lead to the development of next generation M_4 mAChR PAMs.

Results

Pharmacological characterisation of M_4 mAChR PAMs with ACh and Ipx

Hallmarks of ligand binding. We first used radioligand binding assays (**Figure 2A**) to determine the *ground state binding affinities* of ACh and Ipx (K_A) for the orthosteric site and of LY298 and VU154 (K_B) for the allosteric site of the unoccupied human M_4 mAChR (**Figure 2B**), along with the degree of *binding cooperativity* (α) between the agonists and PAMs when the two are co-bound (**Figure 2C**). Analysis of these experiments revealed that LY298 and VU154 have very similar binding affinities for the allosteric site with values (expressed as negative logarithms; pK_B) of 5.65 ± 0.07 and 5.83 ± 0.12, respectively (**Figure 2B**), in accordance with

previous studies (Bubser et al., 2014; Leach et al., 2011). Both PAMs potentiated the ground state binding affinity of ACh and Ipx (**Figure 2D,E**), with the effect being greatest between LY298 and ACh (approx. 400-fold increase in binding affinity). Comparatively, the positive cooperativity between VU154 and ACh was only 40-fold. When Ipx was used as the agonist, the binding affinity modulation mediated by both PAMs was more modest, characterized by an approximate 72-fold potentiation for the combination of Ipx and LY298, and 10-fold potentiation for the combination of Ipx and VU154. These results indicate *probe-dependent* effects (Valant et al., 2012) with respect to the ability of either PAM to modulate the affinity of each agonist (**Figure 2D,E**). It is important to note that binding modulation is *reciprocal* and the affinities of LY298 and VU154 were also increased in the agonist bound state (**Figure 2E**). This results in LY298 having a 5-fold higher binding affinity than VU154 when agonists are bound (**Table S1**).

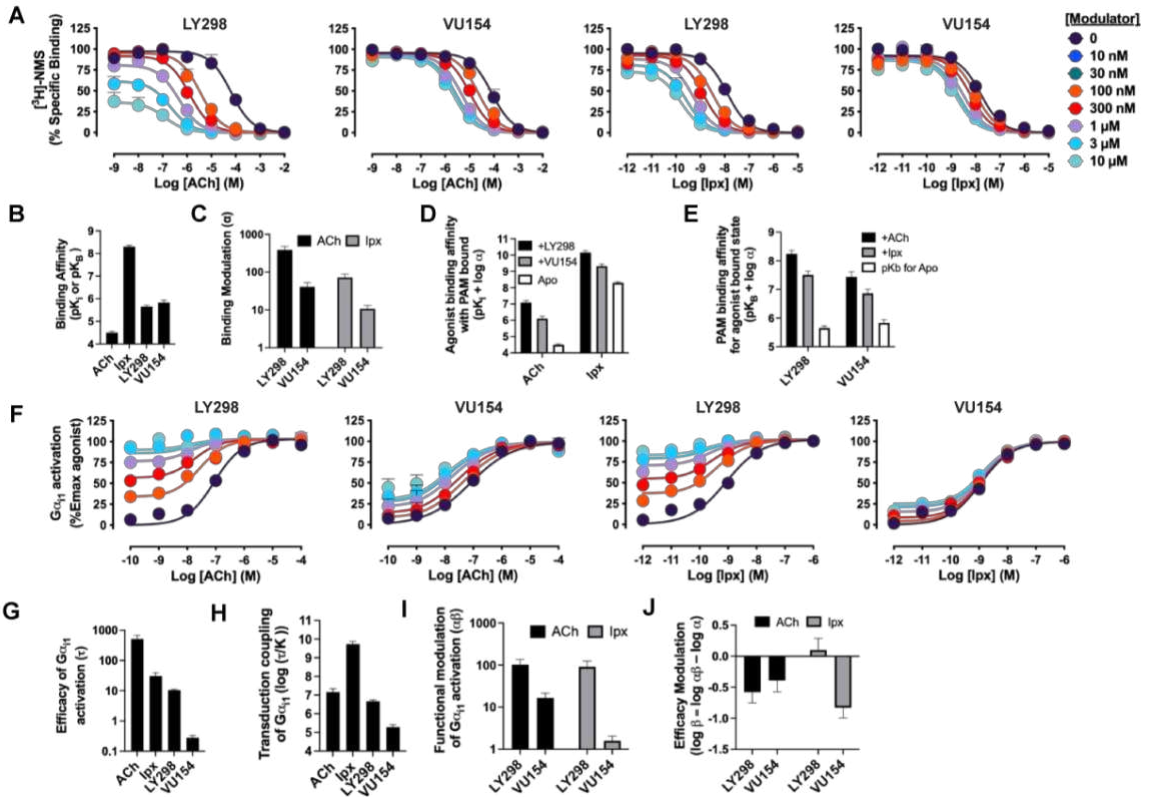

Figure 2. Pharmacological characterization of the PAMs, LY298 and VU154, with ACh and Ipx. (**A**) Concentration response curves of interactions between the orthosteric and allosteric ligands at the human M_4 mAChR in [^{3}H]-N-methylscopolamine ([^{3}H]-NMS) binding assays.(**B-E**) Quantification of data from (**A**) to calculate (**B**) equilibrium binding affinities (pK_i and pK_B), (**C**) the degree of binding modulation (α) between the agonists and PAMs, and the modified

affinities (**D**) αK_A and (**E**) αK_B. (**F**) Concentration response curves of interactions between the orthosteric and allosteric ligands at the human M_4 mAChR with an area under the curve analysis of $G\alpha_{i1}$ activation using the TruPath assay. (**G-J**) Quantification of data from (**A,F**) to calculate (**G**) the signaling efficacy (τ_A and τ_B) and (**H**) the the transduction coupling coefficients (log (τ/K)) of each ligand, (**I**) the functional cooperativity ($\alpha\beta$) between ligands, and (**J**) the efficacy modulation (β) between ligands. All data are mean ± SEM of 3 or more independent experiments performed in duplicate or triplicate with the pharmacological parameters determined from a global fit of the data. The error in (**D,E,J**) was propagated using the square root of the sum of the squares. See **Table S1**.

Hallmarks of GPCR function. We subsequently used the BRET-based TruPath assay (Olsen et al., 2020), as a proximal measure of G protein activation with $G\alpha_{i1}$ (**Figure 2F**). We also used a more amplified downstream signalling assay, extracellular signal-regulated kinases 1/2 phosphorylation (pERK1/2), that is also dependent on G_i activation (**Figure S1A**), to measure the cell-based activity of each PAM with each agonist. These signaling assays allowed us to determine the *efficacy* of the agonists (τ_A) and the PAMs (τ_B) (**Figure 2G, Figure S1B**). Importantly, efficacy (τ), as defined from the Black-Leff operational model of agonism (Black and Leff, 1983), is determined by receptor density (B_{max}), the ability of an agonist to promote an active receptor conformation, and the ability of a cellular system to generate a response (**Figure 1B**). Notably, in both signalling assays, the rank order of efficacy was ACh > Ipx > LY298 > VU154. We subsequently calculated the *transducer coupling coefficient* (τ/K) (**Figure 1B; Figure 2H; S1C**), a parameter often used to quantify agonist bias. The transducer coupling coefficient accounts for the ground state binding affinity of the agonist (K), either orthosteric or allosteric, and characterises the agonism of a specific pathway defined as the interaction between an agonist, receptor, and transducer, which indirectly interacts with effector and signaling proteins (Kenakin et al., 2012). Accordingly, in both assays, the rank order of transducer coupling was Ipx >> ACh ~ LY298 > VU154 due to Ipx having a higher ground state binding affinity for the receptor. Overall, these results indicate that although ACh is a more efficacious agonist than Ipx it has lower transducer coupling coefficient. In contrast, LY298 has both better efficacy and transducer coupling than VU154 (**Table S1**).

The signaling assays and use of an operational model of allosterism also allowed for the determination of the *functional cooperativity* ($\alpha\beta$) exerted by the PAMs (**Figure 2I; S1D**), which is a composite parameter accounting for both binding (α) and efficacy (β) modulation. Notably, VU154 displayed lower positive functional cooperativity with ACh than LY298. Strikingly, VU154 had negligible functional modulation with Ipx in contrast to the cooperativity observed with ACh in the TruPath assay. The 10-fold difference in $\alpha\beta$ values for VU154 between ACh and Ipx highlights the dependence of the orthosteric probe used in the assay (i.e. *probe dependence*); on this basis, VU154 would be classified as a NAL (not a PAM) with Ipx in the TruPath assay (**Table S1**).

The degree of *efficacy modulation* (β) that the PAMs have on the agonists can be calculated directly by subtracting the binding modulation (α) from the functional modulation ($\alpha\beta$) (**Figure 2J; S1E**). A caveat of this analysis is that errors for β are higher due the error being propagated between experiments. Ideally, the degree of efficacy modulation would be determined in an experimental system where the maximal efficacy of system is not reached by the agonists alone (Berizzi et al., 2016). Nevertheless, our analysis shows the PAMs LY298 and VU154 appear to have a slight negative to neutral effect on agonist efficacy in the G_{i1} Trupath and pERK1/2 assays (**Table S1**), suggesting that the predominant allosteric effect exerted by these PAMs is mediated through binding modulation.

Collectively, our extensive analysis on the pharmacology of LY298 and VU154 with ACh and Ipx offers detailed insight into the key differences between these ligands across a range of pharmacological properties: ligand binding, probe dependence, efficacy, agonist-receptor-transducer interactions, and allosteric modulation (**Figure 1, Table S1**). We hypothesised that structures of the human M_4 mAChR in complex with different agonists and PAMs combined with molecular dynamic simulations could provide high resolution molecular insights into the different pharmacological profiles of these ligands.

Determination of M_4R-G_{i1} complex structures

Similar to the approach used in prior determination of active-state structures of the M_1 and M_2 mAChRs (Maeda et al., 2019), we used a human M_4 mAChR construct that lacked residues

242 to 387 of the third intracellular loop to improve receptor expression and purification, and made complexes of the receptor with G_{i1} protein and either the endogenous agonist, ACh, or Ipx. Due to the higher affinity of Ipx compared to ACh (Schrage et al., 2013), we utilised Ipx to form additional M_4R-G_{i1} complexes with or without the co-addition of either LY298 or VU154. In all instances, complex formation was initiated by combining purified M_4 mAChR immobilized on anti-FLAG resin with detergent solubilized G_{i1} membranes, a single-chain variable fragment (scFv16) that binds G_i and Gβ, and the addition of apyrase to remove guanosine 5'-diphosphate (Maeda et al., 2018). For this study, we used a G_{i1} heterotrimer composed of a dominant negative form of human $G\alpha_{i1}$, and human $G\beta_1$ and $G\gamma_2$. (Liang et al., 2018a). Vitrified samples of each complex were imaged using conventional cryo-TEM on a Titan Krios microscope (Danev et al., 2021).

The structures of ACh-, Ipx-, LY298-Ipx-, and VU154-Ipx-bound M_4R-G_{i1} complexes were determined to resolutions of 2.8, 2.8, 2.4, and 2.5 Å, respectively (**Figure 3A-E, S2, Table S2**). For the ACh-bound M_4R-G_{i1} complex, an additional focus refinement yielded an improved map of the receptor and binding site (2.75 Å) for modelling (**Figure 3E**). The electron microscopy (EM) density maps for all complexes were sufficient for confident placement of backbone and sidechains for most of the receptor, G_{i1}, and scFv16, and the bound ligands with exception of the alkyne bond of Ipx (**Figure S3**). Notably, in the Ipx-bound structures, EM density for the alkyne bond of Ipx was missing (**Figure S3F**), matching previous cryo-EM Ipx-bound mAChR structures (Maeda et al., 2019). As such, it is difficult to place the alkyne bond of Ipx into one preferred pose, largely because of rotational freedom on the carbon between the alkyne bond and the rotatable trimethyl ammonium ion. This is highlighted by the different poses of the alkyne bond across the different Ipx-bound mAChR structures and is consistent with the reported docking of Ipx in the M_2 mAChR structure (**Figure S3F**) (Maeda et al., 2019).

In all four structures, EM density beyond the top of transmembrane helix 1 (TM1) and the third intracellular loop (ICL3) of the receptor was poorly observed and not modelled. Similarly, the EM density of the α-helical domain of $G\alpha_{i1}$ was poor and not modelled. These regions are highly dynamic and typically not modelled in many class A GPCR-G protein complex

structures. Apart from these regions, most amino acid side chains were well resolved in the final EM density maps (**Figure S3**).

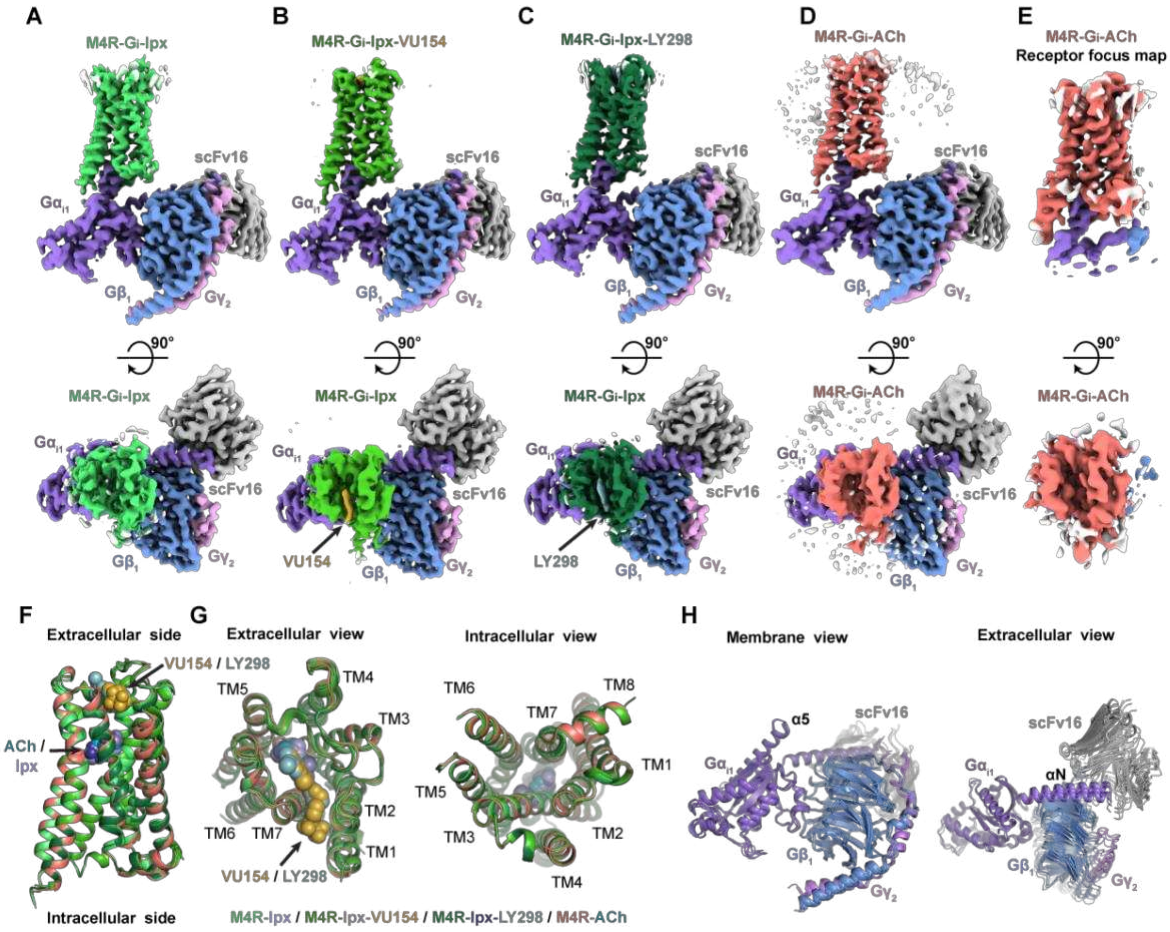

Figure 3. Cryo-EM structures of the M_4R-G_{i1}-scFv16 complexes. (**A-E**) Cryo-EM maps of (**A**) Ipx-bound, (**B**) VU154-Ipx-bound, (**C**) LY298-Ipx bound, and (**D,E**) ACh-bound M_4R-G_{i1}-scFv16 complexes with views from the membrane and the extracellular surface. (**F,G**) Comparison of the receptor models with bound ligands and views from the (**G**) extracellular and intracellular surface of the receptors. (**H**) Comparison of the positions of $G\alpha_{i1}G\beta_1G\gamma_2$-scFv16 with views from the membrane and extracellular surface.

Structure and dynamics of agonist binding

Recently, cryo-EM structures of M_4R-G_{i1} complexes bound to ipx, ipx and the PAM LY2119620, and an allosteric agonist c110, were determined (Wang et al., 2022). Surprisingly, comparison of the M_4R-G_{i1} complex structures reveal larger differences in the position of key orthosteric and allosteric site residues than the M_1R-G_{11} and M_2R-G_{oA} complex structures (**Figure S4-5**). Unfortunately, the quality of density in the EM maps around the orthosteric and allosteric

sites of these M_4R-G_{i1} structures (Wang et al., 2022) was poor resulting in several key residues being mismodelled in each site (**Figure S5**). Therefore, differences between the M_4R-G_{i1} structures are highly likely to not be due to genuine differences, and as such we compared to the M_1R-G_{11} and M_2R-G_{oA} complex structures in this study (Maeda et al., 2019).

Overall, our M_4R-G_{i1} complex structures are similar in architecture to that of other activated class A GPCRs including the M_1R-G_{11} and M_2R-G_{oA} complexes (**Figure S4**). Superposition of the M_4R-G_{i1} complexes revealed nearly identical structures with root mean square deviations (RMSD) of 0.4–0.5 Å for the full complexes and 0.3–0.4 Å for the receptors alone (**Figure 3F**). The largest differences occur around the extracellular surface of the receptors (**Figure 3G**) along with slight displacements in the position of the αN helix of $G\alpha_{i1}$ and $G\beta_1$, $G\gamma_2$, and scFv16 with respect to the receptor (**Figure 3H**). The EM density of side chains surrounding the ACh and Ipx binding sites (**Figure 4A-B**) was well resolved providing the opportunity to understand structural determinants of orthosteric agonist binding. The orthosteric site of the M_4 mAChR, in common with the other mAChR subtypes, is buried within the TM bundle in an aromatic cage that is composed of four tyrosine residues, two tryptophan residues, one phenylalanine residue, and seven other polar and nonpolar residues (**Figure 4C**). Notably, all 14 of these residues are absolutely conserved across all five mAChR subtypes, underscoring the difficulty in developing highly subtype-selective orthosteric agonists (Burger et al., 2018). Both ACh and Ipx have a positively charged trimethyl ammonium ion that makes cation-π interactions with $Y113^{3.33}$, $Y416^{6.51}$, $Y439^{7.39}$, and $Y443^{7.43}$ (**Figure 4C**) (superscript refers to the Ballesteros and Weinstein scheme for conserved class A GPCR residues) (Ballesteros and Weinstein, 1995). Likewise, both ACh and Ipx have a polar oxygen atom that can form a hydrogen bond to the indole nitrogen of $W164^{4.57}$ with the oxygen of Ipx also being in position to interact with the backbone of $N117^{3.37}$ (**Figure 4D**). Mutation of any of these contact residues reduces the affinity of ACh, validating their importance for agonist binding (Leach et al., 2011; Thal et al., 2016). The largest chemical difference between ACh and Ipx is the bulkier heterocyclic isoazoline group of Ipx that makes a π-π interaction with the conserved residue $W413^{6.48}$ (**Figure 4D**). The residue $W413^{6.48}$ is part of the CWxP motif, also known as the rotamer toggle switch, a residue that typically undergoes a change in rotamer between the inactive and active states of class A GPCRs (Shi et al., 2002).

To investigate the structural dynamics of the M_4 mAChR, we performed three independent 500 ns GaMD simulations on the ACh- and Ipx-bound M_4R-G_{i1} cryo-EM structures (**Table S3**). GaMD simulations revealed that ACh undergoes higher fluctuations in the orthosteric site than Ipx (**Figure 4E,F)**. Similarly, the interactions of $N117^{3.37}$, $W164^{4.57}$, and $W413^{6.48}$ with Ipx were more stable than those with ACh (**Figure 4I-P**). In the ACh-bound structure, $W413^{6.48}$ was in a conformation that more closely resembled the inactive-state tiotropium-bound structure (**Figure 4C,D**). GaMD simulations also showed that $W413^{6.48}$ sampled a larger conformational space in the ACh-bound structure than in the Ipx-bound structure (**Figure 4L,P**). The predominate χ_2 angle of $W413^{6.48}$ was approximately 60° and 105° in the ACh-bound and Ipx-bound simulations, respectively, corresponding to the cryo-EM conformations.

Located above ACh and Ipx is a tyrosine lid formed by three residues ($Y113^{3.33}$, $Y416^{6.51}$, and $Y439^{7.39}$) that separates the orthosteric binding-site from an extracellular vestibule (ECV) at the top of the receptor and the bulk solvent (**Figure 4C**). In the inactive conformation, the tyrosine lid is partially open due to $Y416^{6.51}$ rotating away from the binding pocket to accommodate the binding of bulkier inverse agonists such as tiotropium. In contrast, mAChR agonists are typically smaller in size than antagonists and inverse agonists, and this is reflected in a contraction of the size of the orthosteric binding pocket from 115 $Å^3$ when bound to tiotropium to 77 and 63 $Å^3$ when bound to ACh and Ipx, respectively (**Figure 4G,H**) (Tian et al., 2018). Together, the smaller binding pocket of Ipx and more stable binding interactions with nearby residues that include $W413^{6.48}$ likely explain why Ipx has greater than 1,000-fold higher binding affinity than ACh.

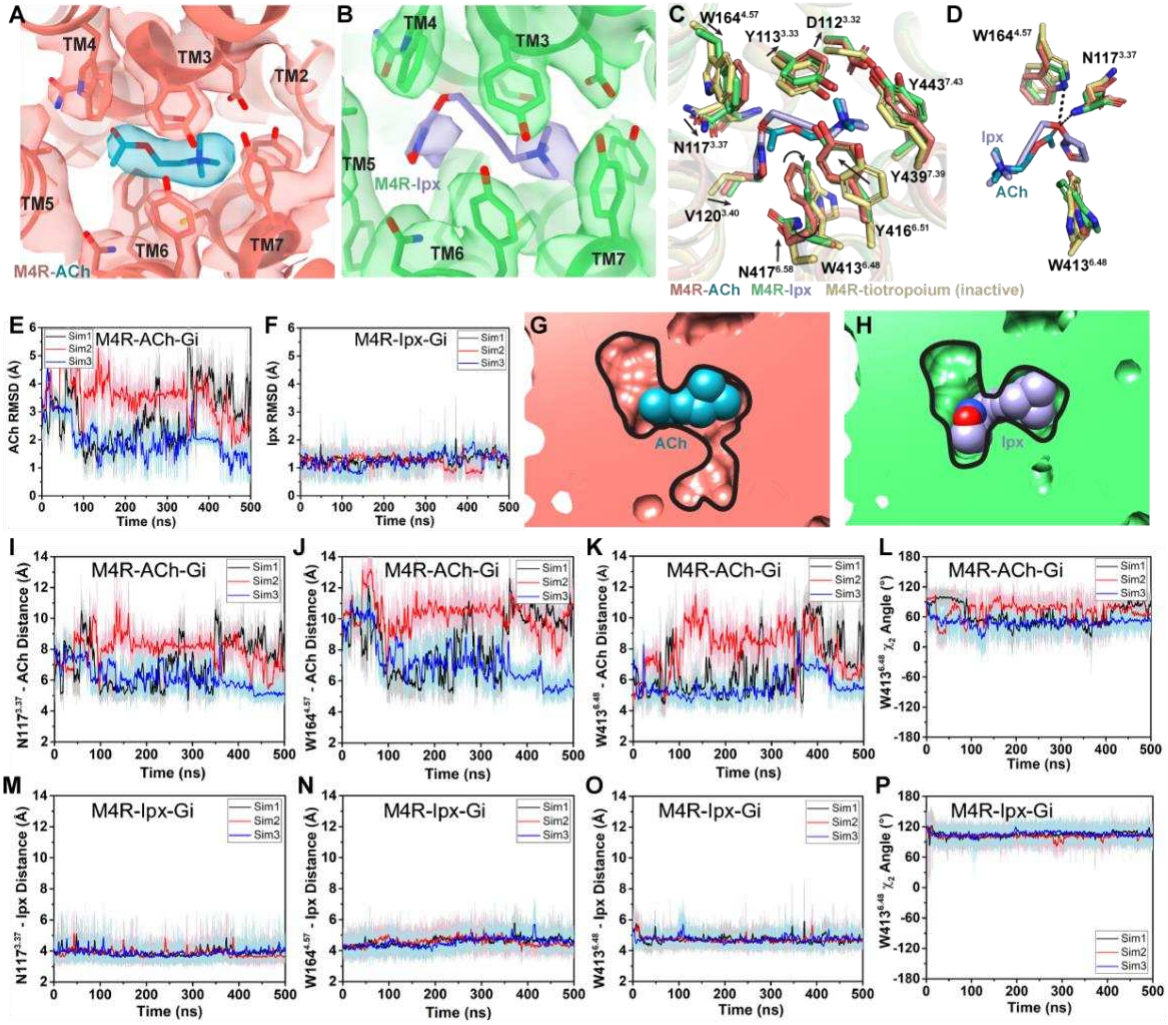

Figure 4. Interactions of ACh and Ipx with the receptor. (**A,B**) Cryo-EM density of the (A) ACh- and (**B**) Ipx-bound structures. (**C,D**) Interactions at the orthosteric binding site comparing the active state ACh- and Ipx-bound structures with the inactive state tiotropium bound structure (PDB: 5DSG). Arrows denote relative movement of residues between the inactive and active states. (**D**) Detailed interactions of ACh and Ipx. Hydrogen bonds are shown as black dashed lines. (**E-F, I-P**) Time courses from GaMD simulations of the ACh- and Ipx- bound M_4R-G_{i1} cryo-EM structures, each performed with 3 separate replicates. Individual replicate simulations are illustrated with different colours. The heading of each plot refers to the specific model used in the simulations. RMSDs of (**E**) ACh and (**F**) Ipx from simulations of the cryo-EM structures. (**G,H**) Cross-sections through the ACh- and Ipx-bound structures denoting the relative size of the binding pockets outlined in black. (**I-P**) The distances of interactions between ACh and Ipx with residues (**I, M**) $N117^{3.37}$, (**J,N**) $W164^{4.67}$, and (**K,O**) $W413^{6.48}$, and (**L,P**) the χ2 angle of $W413^{6.48}$. See **Table S3.**

Structure and dynamics of PAM binding and allosteric modulation of agonist affinity

The M_4R-G_{i1} structures of LY298 and VU154 co-bound with Ipx are very similar to the Ipx- and ACh-bound structures, as well as to prior structures of the M_2 mAChR bound to Ipx and the PAM, LY2119620 (**Figure S4**) (Kruse et al., 2013; Maeda et al., 2019). Both LY298 and VU154 bind directly above the orthosteric site in the ECV that is composed of a floor delineated by the tyrosine lid, and 'walls' formed by residues from TM2, TM6, TM7, ECL2, and ECL3 (**Figure 5A,B**). The EM density surrounding the PAM binding site and the ECV of the M_4 mAChR were clearly resolved with one exception; in the VU154-bound structure the EM density begins to weaken around the trifluoromethylsulfonyl moiety (**Figure 5A**). This was likely due to the moiety's ability to freely rotate (similarly to the alkyne bond of Ipx in the orthosteric site) and a lack of strong interactions with the receptor.

Given the overall similarities revealed by our four cryo-EM structures, we examined if there were further differences in the dynamics between the PAM-bound structures by performing a 3D multivariance analysis (3DVA) of the principal components of motion within the Ipx-, LY298-Ipx, VU154-Ipx, and ACh-bound M_4R-G_{i1} cryo-EM data sets using Cryosparc (Punjani and Fleet, 2021); a similar analysis performed previously on cryo-EM structures of class A and class B GPCRs provided important insights into the allosteric motions of extracellular domains and receptor interactions with G proteins (Josephs et al., 2021; Liang et al., 2020; Mobbs et al., 2021; Zhang et al., 2020).

In the 3DVA of the Ipx-bound complex, the M4 receptor appeared less flexible than the receptor in the ACh-bound complex (**Supplemental Videos 1-2**) consistent with Ipx having a higher binding affinity and more stable pose during the GaMD simulations (**Figure 4E,F**). The LY298-Ipx-bound complex appeared similar to the Ipx-bound complex with LY298 being bound in the ECV (**Supplemental Video 3**). In contrast, the 3DVA of the VU154 structure had more dynamic movements in the allosteric pocket that could reflect partial binding of VU154 (**Supplemental Video 4**). This observation was in line with our findings that VU154 had lower binding cooperativity (**Figure 2C**) and functional cooperativity with agonists than LY298 (**Figure 2I; S1D**). To quantify the differences from the 3DVA, we rigid body fitted and refined the respective M_4R-G_{i1} models into the first and last frames of the EM maps from each principal component of the 3DVA and then calculated the RMSD between the receptor

models from the from the first and last frames (**Figure 5C**). In agreement with our prior observations, the VU154-Ipx-bound and ACh-bound complexes had greater RMSDs with values of 0.06 and 0.09 Å respectively. Comparatively, the Ipx-bound and LY298-Ipx-bound complexes had lower RMSD values of 0.02 and 0.001 Å, respectively. The results of the 3DVA do not represent *bona fide* measures of receptor dynamics, rather they are suggestive of there being differences between the collected data sets that led to the structures. To support these findings, we compared the GaMD simulations of all four cryo-EM structures (**Table S3**). Notably, VU154 underwent considerably higher fluctuations than LY298 with RMSDs ranging from 1.5–15 Å for VU154 and 0.8–2.1 Å for LY298 relative to the cryo-EM structures (**Figure 5D,E**). Therefore, the GaMD simulations corroborate our 3DVA results and suggests that complexes bound to agonists with high affinity or co-bound with agonists and PAMs with high positive cooperativity will exhibit lower dynamic fluctuations.

To investigate why the binding of LY298 was more stable than VU154, we examined the ligand interactions with the receptor. There are three key binding interactions that are shared between both PAMs and the M_4 mAChR: 1) a three-way π-stacking interaction between F186$^{45.51}$ (ECL2 residues have been numbered 45.X denoting their position between TM4 and TM5 with X.50 being a conserved cysteine residue), the aromatic core of the PAMs, and W435$^{7.35}$; 2) a hydrogen bond between Y439$^{7.39}$ of the tyrosine lid and the primary amine of the PAMs; and 3) a hydrogen bond between Y89$^{2.61}$ and the carbonyl oxygen of the PAMs (**Figure 5F,G**). While these interactions are conserved for both PAMs in the consensus cryo-EM maps, during GaMD simulations these interactions were more stable with LY298 than VU154 (**Figure 5H-O**). The importance of these interactions was validated pharmacologically (**Figure S6; Table S4**), whereby mutation of any of these residues completely abolished the

385 binding affinity modulation mediated by LY298 and VU154 at the M_4 mAChR with both Ipx
386 and ACh as agonists.

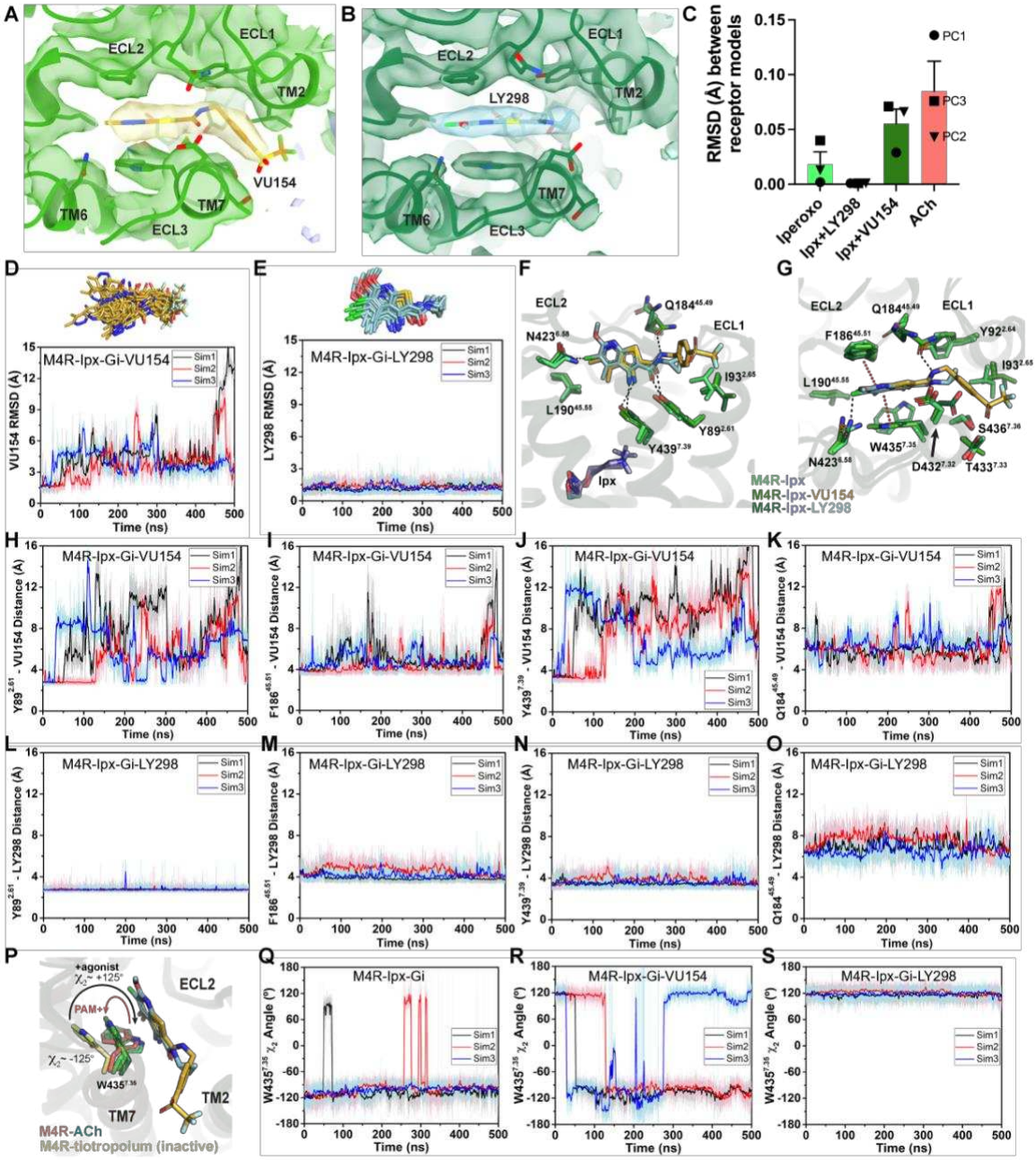

387 **Figure 5 Binding and dynamics of LY293 and VU154.** (**A,B**) Cryo-EM density of the (**A**) VU154-
388 and (**B**) LY298-binding sites. (**C**) The root-mean square deviations (RMSD) between receptor
389 models of the respective cryo-EM structures that were refined into the first and last frames
390 of the EM maps from each principal component (PC1-PC3) of the 3D variability analysis.
391 Values shown are mean ± SEM. (**D,E**) Top representative binding conformations of (**D**) VU154
392 al(**E**) LY298 obtained from structural clustering with frame populations ≥ 1% and time courses
393 of the RMSDs of each PAM relative to the cryo-EM structures. (**F,G**) Binding interactions of

VU154 and LY298 with views from the (**F**) membrane and (**G**) extracellular surface. (**H-O**) Time-courses from three 500 ns GaMD simulations using the (**H-K**) VU154- and (**L-O**) LY298-Ipx-bound cryo-EM structures. Distances between the interactions of VU154 and LY298 with residues (**H, L**) $Y89^{7.39}$, (**I,M**) $F186^{45.51}$, $Y439^{7.39}$, and $Q184^{45.49}$. (**P**) Position and χ2 angle of $W435^{7.35}$ in the tiotropium-, ACh-, Ipx-, VU154-Ipx-, and LY298-Ipx bound structures. (**Q-S**) Time courses of the $W435^{7.35}$ χ2 angle obtained from GaMD simulations in the (**Q**) I-, (**R**) VU154-Ipx-, and (S) LY298-Ipx-bound cryo-EM structures. See **Table S3.**

A potential fourth interaction was observed with residue $Q184^{45.49}$ and the amide nitrogen of the PAMs; however, the GaMD simulations suggest that this interaction is relatively weak (**Figure 5K,O**), consistent with the fact that mutation of $Q184^{45.49}$ to alanine had no effect on the binding modulation of LY298 or VU154 (**Figure S6; Table S4**). In addition, each PAM has at least one unique binding interaction with the receptor (**Figure 5F,G**). For LY298, this is an interaction between the fluorine atom and $N423^{6.58}$ that appeared to be stable during simulation and, when mutated to alanine reduced the binding modulation of LY298 (**Figure S7A**) (Thal et al., 2016). For VU154, two additional hydrogen bonding interactions were formed with $Y92^{2.64}$ and $T433^{7.33}$ (**Figure 5G**), although these interactions were fluctuating during GaMD simulations (**Figure S7B,C**). Finally, $W435^{7.35}$ is a key residue in the ECV that changes from a planar rotamer in the agonist-bound structures to a vertical rotamer that π stacks against the PAMs (**Figure 5P**). In GaMD simulations of the Ipx-bound structure, $W435^{7.35}$ is predominantly in a planar conformation that corresponds to its conformation in the cryo-EM structure (**Figure 5P,Q**). In contrast, the binding of LY298 stabilizes $W435^{7.35}$ into a vertical position (**Figure 5P,S**). However, in the VU154-bound receptor, $W435^{7.35}$ appears to alternate between the planar and vertical positions, consistent with VU154 having a less stable binding pose (**Figure 5R**). These results indicate that the binding of LY298 is more stable than VU154 due to LY298 being able to form stable binding interactions with key residues in the ECV. This provides a likely explanation for why LY298 was able to exert greater positive binding cooperativity on orthosteric agonists than VU154.

A molecular mechanism of probe dependence

As highlighted above, PAMs, LY298 and VU154, displayed stronger allosteric binding modulation with ACh than Ipx, an example of probe dependence (**Figure 2, S1D**). These

findings are in accord with previous studies where we identified probe dependence in the actions of LY298 when tested against other orthosteric agonists (Chan et al., 2008; Suratman et al., 2011). To investigate a mechanism for probe dependence at the M_4 mAChR, we performed GaMD simulations with LY298 and VU154 co-bound with ACh, by replacing Ipx with ACh in the corresponding cryo-EM structures (**Table S3** and **Figure S7**). In the absence of PAM, ACh was more dynamic than Ipx with root-mean-square fluctuations (RMSF) of 2.13 Å versus 0.88 Å, reflective of the fact Ipx binds with higher affinity than ACh (**Figure S7L**). In the presence of LY298 or VU154 the dynamics of ACh binding was decreased, with RMSFs reduced to 1.23 Å and 1.82 Å, respectively, and with LY298 having the greatest effect (**Figure S7L**). This is in line with LY298 having more cooperativity with ACh than VU154 (**Figure 2C**). In comparison to ACh, there was a modest increase in the dynamics of Ipx with the addition of LY298 or VU154, likely reflecting the fact Ipx binding to the receptor was already stable (**Figure S7D-F**). These results provide a plausible mechanism for probe dependence, at least with regards to differences in the magnitude of the allosteric effect depending on the ligand bound. Namely, PAMs manifest higher cooperativity when interacting with agonists, such as ACh, that are inherently less stable on their own when bound to the receptor, in contrast to more stable ligands such as Ipx.

Structural and dynamic insights into orthosteric and allosteric agonism

In addition to the ability to allosterically modulate the function of orthosteric ligands, it has become increasingly appreciated that allosteric ligands may display variable degrees of direct agonism in their own right, over and above any allosteric modulatory effects (Changeux and Christopoulos, 2016). Prior studies have established that the activation process of GPCRs involves conformational changes that extend from the extracellular domains through to the intracellular surface (Nygaard et al., 2009). Comparison of the active state ACh-, Ipx-, LY298-Ipx-, and VU154-Ipx-bound M_4R-G_{i1} structures to the inactive state tiotropium-bound M_4 mAChR structure (Protein Data Bank accession 5DSG) (Thal et al., 2016) thus affords an opportunity to gain new insights into the activation process mediated by multiple orthosteric agonists in the presence and absence of two different PAMs that display high (LY298) and low (VU154) degrees of direct allosteric agonism (**Figure 1F, 6A-C**).

As previously discussed, agonist binding decreases the size of the orthosteric binding site (**Figure 4G,H**). The primary driver of this decrease was the tyrosine lid residue Y416$^{6.51}$, which underwent a large rotation towards Y113$^{3.33}$ creating a hydrogen bond that seals off the tyrosine lid (**Figure 4C**). The closure of the tyrosine lid was further reinforced by a change in the rotamer of W435$^{7.35}$ to a planar position that sits parallel to the tyrosine lid allowing for a π-π interaction with Y416$^{6.51}$ and a positioning of the indole nitrogen of W435$^{7.35}$ to potentially form a hydrogen bond with the hydroxyl of Y89$^{2.61}$ (**Figure 6B**). The contraction of the orthosteric pocket by the inward movement of Y416$^{6.51}$ also led to a contraction of the ECV with a 5 Å inward movement of the top of TM6 and ECL3. As a consequence, the top of TM5 was displaced outward by 4 Å forming a new interface between TM5 and TM6 that was stabilized by a hydrogen bond between T424$^{6.59}$ and the backbone nitrogen of P193$^{5.36}$ along with aromatic interactions between F197$^{5.40}$ and F425$^{6.60}$ (**Figure 6B**). These interactions were specific to the active state structures and appear to be conserved as they were also present in the M_1 and M_2 mAChR active state structures (Maeda et al., 2019). In addition to the movements of TM5 and TM6, there was a smaller 1 Å inward movement of ECL2 (**Figure 6B**). The binding of LY298 and VU154 had minimal impact on the conformation of most ECL residues, implying that the reorganisation of residues in the ECV by orthosteric agonists contributes to the increased affinity of the PAMs (**Figure 2E**). There was a slight further inward shift of ECL2 towards the PAMs to facilitate the 3-way π-stacking interaction with F186$^{45.51}$ and W435$^{7.35}$. In addition, in the PAM-bound structures, Y89$^{2.61}$ rotated away from its position in the ACh- and Ipx-bound structures either due to a loss of an interaction with W435$^{7.35}$ or to form a better hydrogen bond with the carbonyl oxygen of the PAMs (**Figure 6B**).

Below the orthosteric binding site are several signaling motifs that are important for the activation of class A GPCRs, including the PIF motif (Rasmussen et al., 2011; Wacker et al., 2013), the Na^+ binding site (Liu et al., 2012b; White et al., 2018), the NPxxY motif (Fritze et al., 2003), and the DRY motif (**Figure 6C**) (Ballesteros et al., 2001). The conformations of these activation motifs were very similar across all four active-state M_4 mAChR structures and were consistent with the position of these motifs across other active-state class A GPCR structures (Zhou et al., 2019). Collectively, all of the described activation motifs facilitate an 11 Å outward movement of TM6 that typifies GPCR activation and creation of the G protein binding site. In comparison to the ECV residues (**Figure 6B**), beyond the rotamer toggle switch residue

W413$^{6.48}$, there are no discernible differences between the agonist and PAM-agonist-bound structures, suggesting a shared activation mechanism for residues below W413$^{6.48}$ (**Figure 6C**).

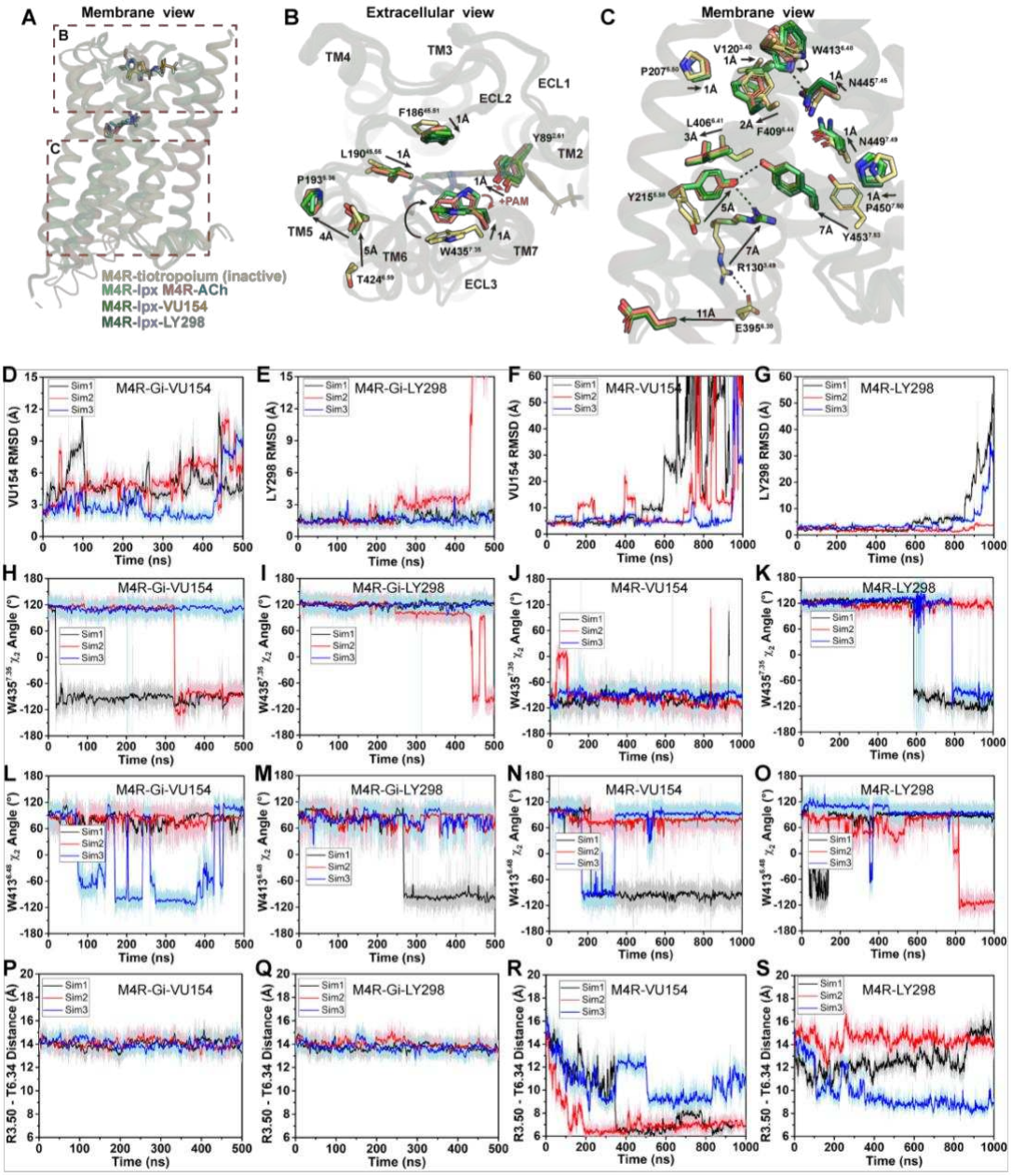

Figure 6. Structural and dynamic insights into orthosteric and allosteric agonism. (**A**) Cartoon of the receptor models indicating regions of interest for panels (**B-C)** shown within the red boxes. (**B**) View of the tiotropium-bound, agonist-bound, and PAM-agonist-bound conformations from the extracellular surface. (**C**) Membrane view of residues and activation motifs involved in signalling. (**D-S**) Time courses of (**D-G**) the PAMs RMSDs, (**H-K**) the W435$^{7.35}$ χ2 angle, (**L-O**) the W413$^{6.48}$ χ2 angle, and (**P-S**) the TM3-TM6 distance measured by distance

between R130$^{3.50}$ and T399$^{6.34}$ obtained from GaMD simulations of the M_4R-G_{i1}-VU154, M_4R-G_{i1}-LY298, M_4R-VU154, and M_4R-LY298 systems, respectively. See **Table S3**.

As indicated above, LY298 also displays robust allosteric agonism in comparison to VU154 (**Figure 2G,H**). To probe whether the allosteric agonism of LY298 could be related to its ability to better stabilize the M_4 mAChR in an active conformation in comparison to VU154, we performed additional GaMD simulations on the LY298-Ipx- and VU154-Ipx-bound M_4R-G_{i1} structures with the agonist Ipx removed (3x 500 ns) and with both Ipx and the G protein removed (3x 1,000 ns) (**Figure 6**, **Table S3**). In GaMD simulations, LY298 underwent lower RMSD fluctuations than VU154 before dissociating from the receptor (**Figure 6D-G**). Similarly, the conformations of W435$^{7.35}$ and W413$^{6.48}$ were better stabilized in the LY298-Ipx-bound systems, indicating that LY298 more strongly promotes an active receptor conformation (**Figure 6H-K**). In the presence of the G protein, both PAMs stabilised an active conformation of the receptor based on the distances between TM3 and TM6 (**Figure 6P,Q**). Upon removal of the G protein, the VU154-bound M_4 mAChR quickly transitioned towards the inactive conformation, while the LY298-bound M_4 mAChR was more resistant to deactivation in the GaMD simulations (**Figure 6R,S**). This observation supports LY298 having greater efficacy than VU154 (**Figure 2G**) as it better stabilizes the active conformation of the M_4 mAChR. Overall, the GaMD simulations show that in the absence of agonist alone, or agonist and G protein, LY298 better stabilizes activation motifs from the top of the receptor (W435$^{7.35}$) all the way down to the intracellular G protein binding pocket (DRY-TM6) providing mechanistic insights into the function of LY298 as a stronger PAM-agonist than VU154.

A molecular basis of species selectivity

One of the main advantages of allosteric modulators is the ability to selectivity target highly conserved proteins. The mAChRs are prime example where allosteric modulators have been designed to selectivity target specific subtypes. To date the only PAM-bound mAChR structures are ones with LY2119620, a PAM that has activity at both the M_2 and M_4 mAChRs. Similarly, LY298 has activity at the M_2 mAChR. However, the allosteric properties of VU154 are differentially affected by the species of the receptor (Wood et al., 2017a, 2017b). At the human M_4 mAChR, LY298 displays robust binding modulation, functional modulation, and allosteric agonism, while VU154 has comparatively weaker allosteric properties (**Figure 1,**

530 **Table S1**). Conversely, at the mouse M_4 mAChR, VU154 has a high degree of positive binding
531 modulation, functional modulation, and allosteric agonism that is comparable to LY298 at the
532 human M_4 mAChR (**Figure S7, Table S1**). Therefore, we aimed to determine if our prior
533 findings could be used to explain the selectivity of VU154 between the human and mouse
534 receptors.
535
536 The amino acid sequences of the human and mouse M_4 mAChRs are highly conserved, with
537 most of the differences occurring between the long third intracellular loop and the N- and C-
538 termini. As shown in **Figure 7A**, only three residues differ between the human and mouse M_4
539 mAChR with respect to the transmembrane domain. Specifically, residue V91 (L in mouse) at
540 the top of TM2 points into the lipid bilayer, and D432 and T433 (E and R in mouse), which are
541 located at the top of TM7 and form part of the allosteric binding site near VU154.
542
543 Previous work suggested that residues D432 and T433 were important for differences in the
544 species selectivity of LY298 (Chan et al., 2008). As such, we examined two single D432E and
545 T433R mutants and a V91L/D432E/T433R triple mutant of the human receptor, along with
546 the mouse M_4 mAChR in radioligand binding and pERK1/2 experiments using Ipx and both
547 PAMs (**Figure S8, Table S1**). For LY298, there were no statistically significant differences in
548 binding or function between species and across the mutants that were more than 3-fold in
549 effect. In contrast, VU154 had a 10-fold higher binding affinity for the Ipx-bound mouse M_4
550 mAChR (compare **Figure 2EG** with **Figure 7B**). The affinity of VU154 increased by 2.5-fold at
551 the D432E and T433R mutants and the triple mutant matched the affinity of the mouse
552 receptor (**Figure 7B**). In functional assays, similar results were observed for VU154 with Ipx at
553 the mouse M_4 mAChR, with significant increases in the efficacy (τ_B – corrected for receptor
554 expression), transduction coefficients (τ_B/K_B), and the functional modulation ($\alpha\beta$) (**Figure 7B,**
555 **S8, Table S1**). Relative to the WT M_4 mAChR, the efficacy, transduction coefficients, and
556 functional modulation of VU154 increased for all of the mutants (**Figure S8**), however, none
557 of the values fully matched the mouse receptor. Nevertheless, these results indicate that
558 V91L, D432E, and T433R play a key role in mediating the species selectivity of VU154.

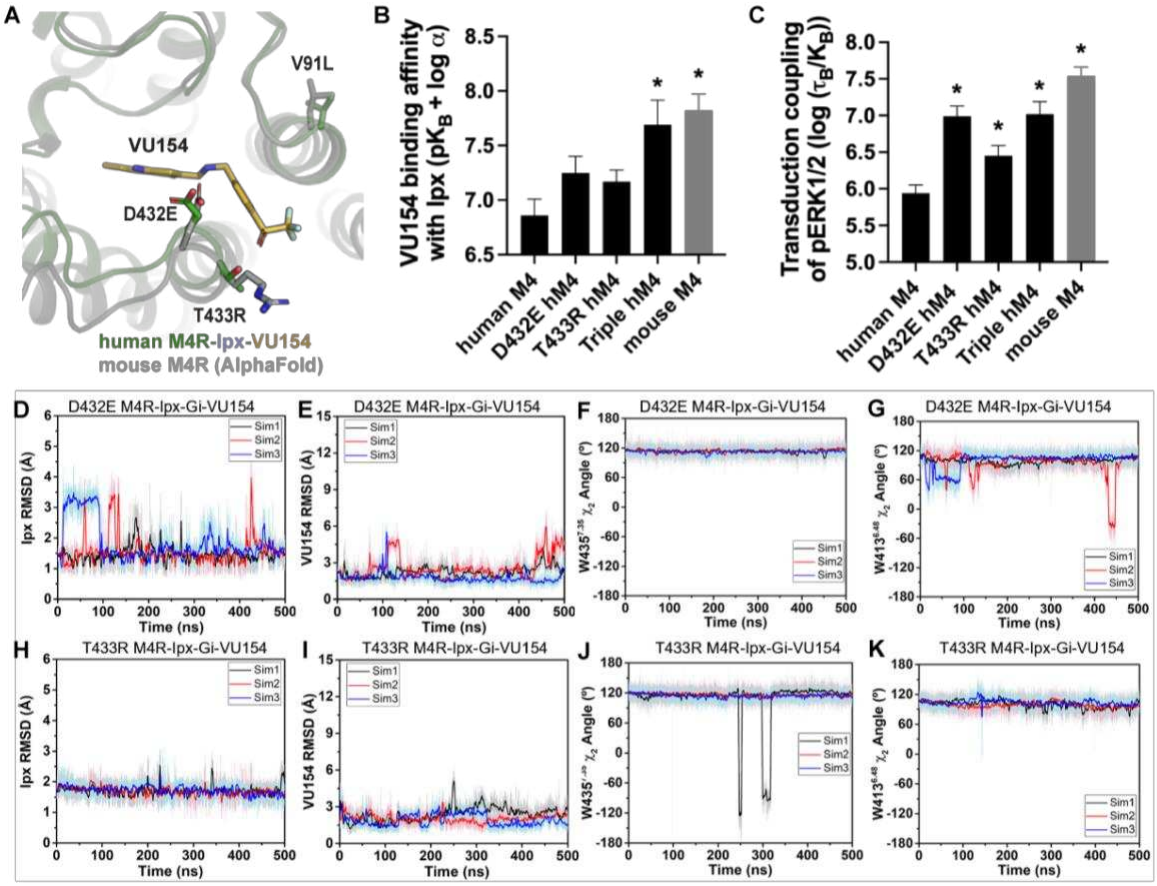

Figure 7. A molecular mechanism for the species selectivity for VU154. (**A**) Comparison of the cryo-EM structure of the human M4 mAChR bound to Ipx-VU154 with the AlphaFold model of the mouse M4 mAChR (Jumper et al., 2021; Varadi et al., 2022). The three residues that differ between species and within the core 7TM bundle from the human receptor (V91, D432, and T433) are shown as sticks along with the corresponding residues from the mouse receptor. (**B**) The binding affinity of VU154 for the Ipx-bound conformation ($pK_{B\text{-}Ipx} = pK_B + \alpha$) determined from [^{3}H]-NMS binding experiments. Values calculated with data from **Figure S8A** with propagated error. (**C**) Transduction coupling coefficients (log (τ/K)) of pERK1/2 signaling from data from **Figure S8A,E**). (**D-K**) Time courses of obtained from GaMD simulations of the (**D-G**) D432E and (**H-K**) T433R mutant M_4R-Ipx-G_{i1}-VU154 systems with (**D,H**) Ipx RMSDs, (**E,I**), VU154 RMSDs, (**F,J**) W435$^{7.35}$ χ_2 angle, and (**G,K**) W413$^{6.48}$ χ_2 angle. See **Table S4** and **Figure S8**. (**B,C**) Data shown are mean ± SEM from 3 or more experiments performed in duplicate with the pharmacological parameters determined from a global fit of the data. *Indicates statistical significance ($p < 0.05$) relative to WT as determined by a one-way ANOVA with a Dunnett's post-hoc test.

Our prior findings suggest the robust allosteric activity of LY298 at the human M_4 mAChR was due to stable interactions with the receptor (**Figure 5**). As a proof-of-principle, we questioned if GaMD simulations would produce a stable binding mode for VU154 with D432E and T433R mutations to the VU154-Ipx-bound M_4R-G_{i1} cryo-EM structure that was similar to our previously observed stable binding pose of LY298 (**Figure 5, Table S3**). Excitingly, both the D432E and T433R mutants resulted in a dynamic profile of VU154 that matched our GaMD simulations of LY298 from the LY298-Ipx-bound M_4R-G_{i1} cryo-EM structure, including stabilized VU154 binding, constrained χ_2 rotamer conformations of W435$^{7.35}$ and W413$^{6.48}$, and stable binding interactions with Y89$^{2.61}$, Y439$^{7.39}$, Q184$^{45.49}$, and F186$^{45.51}$ (**Figure 7D-K, S8, Supplemental Video 9,10**). Collectively, these findings reiterate the importance of receptor dynamics in the determination of allosteric modulator selectivity, as even subtle differences in amino acid residues between species may result in profound changes in overall stability of the same PAM-agonist-receptor complex.

Discussion

Major advances have been made in recent years in the appreciation of the role of GPCR allostery and its relevance to modern drug discovery (Changeux and Christopoulos, 2016; Wootten et al., 2013). Despite an increase in the number of reported high-resolution GPCR structures bound to allosteric ligands (Thal et al., 2018), there remains a paucity of molecular-level details about the interplay between the complex chemical and pharmacological parameters that define allostery at GPCRs. By combining detailed pharmacology studies, multiple high-resolution cryo-EM structures of the M_4 mAChR bound to two distinctly pharmacologically different agonists and PAMs, and GaMD simulations, we have now provided exquisite in-depth insights into the relationship between both structure and dynamics that govern multiple facets of GPCR allostery (**Figure 8A**).

Comparison of the ACh- and Ipx-bound M_4 mAChR structures revealed that Ipx bound in a smaller binding pocket (**Figure 4G,H**), and GaMD simulations showed that Ipx formed more stable interactions with the receptor (**Figure 4I-P**). These observations likely explained why Ipx exhibited greater than 1,000-fold higher binding affinity than ACh (**Figure 2B**), being consistent with studies of other agonists at the β_1-adrenoceptor and the M_1 mAChR (Brown et al., 2021; Warne et al., 2019) (**Figure 8B**). The observation that ACh was a more efficacious

agonist than Ipx (**Figure 2G**) yet bound with lower affinity and less stable interactions than Ipx was paradoxical. Kenakin and Onaran previously opined on the paradox between ligand binding affinity and efficacy (Kenakin and Onaran, 2002), and showed via simulations that, in general, there was a negative correlation between binding affinity and efficacy. One interpretation of these results was that the ACh-bound M_4 mAChR more readily sampled receptor conformations that engaged with the transducers (Manglik et al., 2015). Similarly, the ACh-bound M_4 mAChR may also have faster G protein turnover than Ipx due to Ipx-M_4R-Gi1 forming a more stable ternary complex (Furness et al., 2016) (**Figure 8B**). In fact, the later point was supported by Ipx having a greater transducer coupling coefficient than ACh (**Figure 2H**) and suggests that structures of GPCRs in a ternary complex (agonist-receptor-transducer) are better represented by their transducer coupling coefficients than the efficacy of the agonist with respect to the transducer mediated signalling pathway(s). Given that transducer coupling coefficients were used to calculate ligand bias, one might expect structures of GPCR ternary complexes to capture conformations associated with ligand bias. Indeed, structures of GPCRs bound to biased ligands have now been reported for many GPCRs (Liang et al., 2018b; Masureel et al., 2018; McCorvy et al., 2018; Wacker et al., 2013; Warne et al., 2012; Wingler et al., 2019). Currently, however, there is no generalizable structural basis that explains ligand bias (Seyedabadi et al., 2022) as the conformational differences are likely to be more subtle and dynamic, and therefore require the combination of techniques like NMR spectroscopy, single molecule FRET, and MD simulations to fully resolve (Cao et al., 2021; Cong et al., 2021; Gregorio et al., 2017; Huang et al., 2021; Katayama et al., 2021; Liu et al., 2012a; Solt et al., 2017; Sušac et al., 2018; Ye et al., 2016).

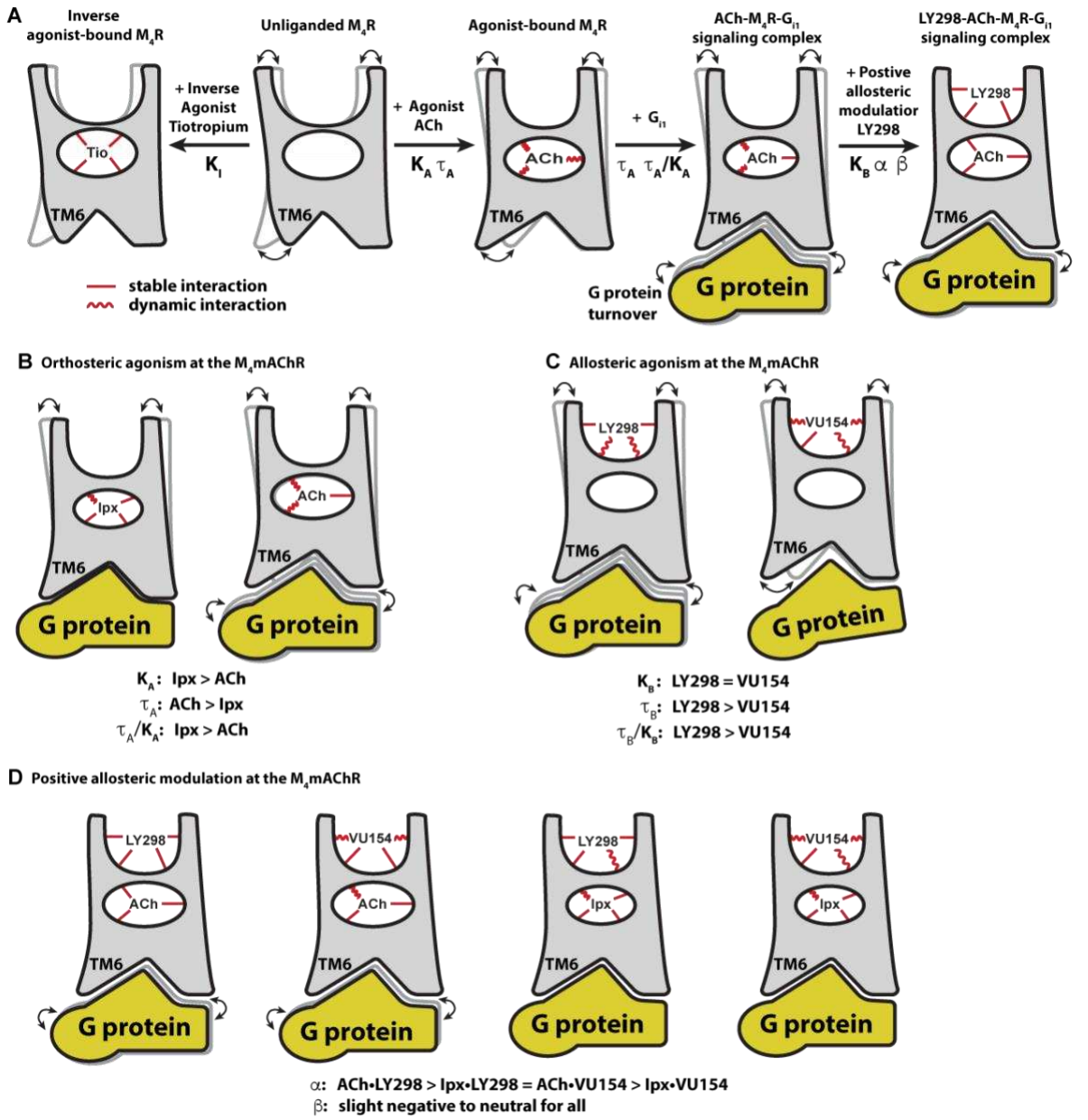

Figure 8. Conformational dynamics of the allostery at M_4 mAChR signalling complexes. (**A**) A schematic cartoon illustrating the conformational states of the ligands and the M_4 mAChR when bound to different types of ligands and transducer, along with the resulting dynamic profiles. Pharmacological parameters related to each conformational change are shown. Stable ligand-receptor interactions are denoted by a straight line and less-stable (more dynamic) interactions are denoted by a wavy line. (**B**) Ipx bound the M_4 mAChR with a higher affinity and more stability than ACh but had lower efficacy. ACh being more loosely bound and coupled to G protein may facilitate more G protein turnover accounting for its higher efficacy. (**C**) LY298 and VU154 bound to the M_4 mAChR with similar affinity for the ground of the receptor, but LY298 was found to bind more stably. LY298 had a higher efficacy than

642 VU154, suggesting that allosteric agonism at the M_4 mAChR is mediated by stabilization of
643 the ECV.(**D**) The PAMs LY298 and VU154 display robust binding modulation at the M_4 mAChR
644 with LY298 having a stronger allosteric effect. Both PAMs displayed stronger binding
645 modulation with the agonist ACh versus Ipx, an example of probe dependence. Both PAMs
646 also displayed a slight negative to neutral effect on the efficacy of the agonists, suggesting
647 that their mechanism of action is largely through binding.

648

649 This study highlighted that two PAMs with distinctly different pharmacological profiles (**Figure**
650 **1**) may bind to and stabilize receptor conformations that were very similar when viewed as
651 static structures (**Figure 5**). In contrast, the 3DVA analysis from our cryo-EM structures
652 suggested differences in the dynamics of the cryo-EM structures that were explored further
653 in GaMD simulations (**Figure 5C, Supplementary Videos 1-4**) and revealed that LY298 had a
654 more stable binding pose and interactions with the receptor than VU154 in the PAM-agonist-
655 receptor-transducer bound conformation. These observations were consistent with LY298
656 having greater positive binding cooperativity than VU154 (**Figure 2E**) and suggested that
657 GaMD simulations of PAMs bound to the M_4 mAChR could be an extremely valuable tool for
658 future drug discovery and optimization (Bhattarai and Miao, 2018).
659
660 Pharmacological analysis revealed that LY298 is a better PAM-agonist than VU154 with
661 respect to efficacy (**Figure 2G**) and transduction coefficients (**Figure 2H**) in the G_{i1} Trupath and
662 pERK1/2 signalling assays. GaMD simulations of the PAM-receptor-transducer and PAM-
663 receptor bound complexes, again showed that LY298 more stably interacted with the
664 receptor (**Figure 5**) and in the absence of G protein better stabilized the duration of the active
665 conformation of the receptor (**Figure 6**). These findings were not contradictory to our above
666 findings that ACh was more efficacious than Ipx despite having weaker interactions with the
667 receptor, because when the ground state affinity of the ligands was accounted for in the
668 transduction coupling coefficients the rank order of agonism was Ipx >> ACh ~ LY298 > VU154
669 (**Figure 2B**). Furthermore, these results were in accordance with the observations of Kenakin
670 and Onaran that ligands with the same binding affinity can also have differing efficacies (and
671 vice-versa). In addition, the mechanism of agonism for allosteric ligands that bind to the ECV
672 may differ (Xu et al., 2021). Prior work by DeVree *et al.* established that allosteric coupling of
673 G proteins to the unliganded active receptor conformation promoted closure of the ECV

674 region (DeVree et al., 2016). This allosteric coupling is reciprocal and stabilizing the ECV region
675 by PAMs likely leads to increased efficacy (**Figure 8C**).
676
677 The PAMs LY298 and VU154 also displayed stronger allosteric effects with ACh than with Ipx,
678 an observation known as probe dependence (**Figure 2C-E**). Probe dependence can have
679 substantial implications on how allosteric ligands are detected, validated, and their potential
680 therapeutic utility (Kenakin, 2005). Examples of probe dependence are not limited to studies
681 on mAChRs and have been observed across multiple receptor families (Christopoulos, 2014;
682 Gentry et al., 2015; Pani et al., 2021; Slosky et al., 2020; Wang et al., 2021b). GaMD
683 simulations comparing the PAMs co-bound to either Ipx or ACh showed that the PAMs had a
684 stabilizing effect on ACh, whereas the stability of Ipx was slightly reduced by the PAMs likely
685 because the binding of Ipx was already stable. This is a sensible explanation from
686 thermodynamic principles. Another explanation invokes the two-state receptor model
687 (Canals et al., 2011), which stipulates that the degree of positive modulation for PAMs
688 increases with an increase in the efficacy of the agonists. The pharmacology data support this
689 model, as ACh was more efficacious than Ipx and was better modulated by both PAMs (**Figure**
690 **8D**). These results again highlight the apparent paradox between ligands being more stably
691 bound to the receptor but also having lower efficacy. Supporting both observations is the fact
692 that the positive functional modulation ($\alpha\beta$) of LY298 and VU154 in G_{i1} signalling assays is
693 driven by positive binding modulation (α), as the efficacy modulation (β) of the PAMs was
694 negative to neutral (**Figure 2J, S1E**). These observations were consistent with recent studies
695 that suggest the conformational dynamics between agonist and receptor were important for
696 functional signalling (Bumbak et al., 2020; Cary et al., 2022; Deganutti et al., 2022; O'Connor
697 et al., 2015).
698
699 The findings presented here provide new insight into the allosteric signalling and allosteric
700 modulation of GPCRs by combining the analytical analysis of multiple pharmacology assays
701 along with cryo-EM structures and GaMD simulations. Overall, these results provide a
702 framework for future mechanistic studies, and ultimately, aid in the discovery, design, and
703 optimization of allosteric drugs as novel therapeutic candidates for clinical progression.
704
705

Acknowledgments

This work was supported by a Wellcome Trust Collaborative Award (201529/Z/16/Z; P.M.S., A.B.T., A.C.), the National Health and Medical Research Council of Australia (1055134, 1150083, and 1138448), the Australian Research Council (DE170100152, DP190102950, and IC200100052), and the National Institutes of Health (GM132572). P.M.S. is a Senior Principal Research Fellow (1154434), D.W. a Senior Research Fellow (1155302), D.M.T. an Early Career Research Fellow (1196951), and K.L. a Future Fellow (160100075). R.D. was supported by Takeda Science Foundation 2019 Medical Research Grant and Japan Science and Technology Agency PRESTO (18069571). This work was partially supported by the Monash University Ramaciotti Centre for cryo-electron microscopy and the Monash University MASSIVE high-performance computing facility and supercomputing resources with the XSEDE allocation award TG-MCB180049 and NERSC project M2874. We thank John Tesmer for discussion and the suggestion of calculating DAQ scores.

Author Contributions

D.M.T, A.C., P.M.S., and A.B.T. designed the overall research; Z.V. and D.M.T designed, expressed, and purified protein samples; Yi-L.L. and A.G. performed negative-stain EM; R.D. performed sample vitrification and cryo-EM imaging; M.J.B, R.D., J.M., and D.M.T processed the EM data; J.M., Z.V., and D.M.T. generated and analysed atomic models; J.W, A.B, and Y.M designed, performed, analysed GaMD simulations, and contributed to writing. V.P., V.N., K.L., W.A.C.B, E.T.W., E.K., G.T., and M.Y., generated DNA constructs and performed pharmacology experiments. D.M.T, C.V., V.P., and K.L. analysed pharmacology data. C.W.L. provided VU0467154. D.W., P.M.S, A.B.T., Y.M., A.C., and D.M.T provided supervision. D.M.T. and A.C. wrote the manuscript with contributions and input from all authors.

Competing Interests

P.M.S, D.W., and A.C. are shareholders of Septurna Inc.

Data and materials availability

All data generated or analysed during this study are included in the manuscript. Structural data has been deposited in the Protein Data Bank (PDB) and Electron Microscopy Data Bank (EMDB) under the following codes:

1) **M4R–G_{i1}-Ipx** **PDB: 7TRK** **EMD-26099**
2) **M4R–G_{i1}-Ipx-LY298** **PDB: 7TRP** **EMD-26100**
3) **M4R–G_{i1}-Ipx-VU154** **PDB: 7TRQ** **EMD-26101**
4) **M4R–G_{i1}-ACh** **PDB: 7TRS** **EMD-26102**

References

Ballesteros, J.A., and Weinstein, H. (1995). [19] Integrated methods for the construction of three-dimensional models and computational probing of structure-function relations in G protein-coupled receptors. In Methods in Neurosciences, S.C. Sealfon, ed. (Academic Press), pp. 366–428.

Ballesteros, J.A., Jensen, A.D., Liapakis, G., Rasmussen, S.G., Shi, L., Gether, U., and Javitch, J.A. (2001). Activation of the beta 2-adrenergic receptor involves disruption of an ionic lock between the cytoplasmic ends of transmembrane segments 3 and 6. J Biol Chem *276*, 29171–29177. https://doi.org/10.1074/jbc.M103747200.

Berizzi, A.E., Gentry, P.R., Rueda, P., Den Hoedt, S., Sexton, P.M., Langmead, C.J., and Christopoulos, A. (2016). Molecular Mechanisms of Action of M5 Muscarinic Acetylcholine Receptor Allosteric Modulators. Mol Pharmacol *90*, 427–436. https://doi.org/10.1124/mol.116.104182.

Berman, H., Henrick, K., and Nakamura, H. (2003). Announcing the worldwide Protein Data Bank. Nat Struct Biol *10*, 980. https://doi.org/10.1038/nsb1203-980.

Bhattarai, A., and Miao, Y. (2018). Gaussian accelerated molecular dynamics for elucidation of drug pathways. Expert Opin Drug Discov *13*, 1055–1065. https://doi.org/10.1080/17460441.2018.1538207.

Black, J.W., and Leff, P. (1983). Operational models of pharmacological agonism. Proc R Soc Lond B Biol Sci *220*, 141–162. https://doi.org/10.1098/rspb.1983.0093.

Brown, A.J.H., Bradley, S.J., Marshall, F.H., Brown, G.A., Bennett, K.A., Brown, J., Cansfield, J.E., Cross, D.M., de Graaf, C., Hudson, B.D., et al. (2021). From structure to clinic: Design of a muscarinic M1 receptor agonist with potential to treatment of Alzheimer's disease. Cell *184*, 5886-5901.e22. https://doi.org/10.1016/j.cell.2021.11.001.

Bubser, M., Bridges, T.M., Dencker, D., Gould, R.W., Grannan, M., Noetzel, M.J., Lamsal, A., Niswender, C.M., Daniels, J.S., Poslusney, M.S., et al. (2014). Selective activation of M4 muscarinic acetylcholine receptors reverses MK-801-induced behavioral impairments and enhances associative learning in rodents. ACS Chem Neurosci *5*, 920–942. https://doi.org/10.1021/cn500128b.

Bumbak, F., Thomas, T., Noonan-Williams, B.J., Vaid, T.M., Yan, F., Whitehead, A.R., Bruell, S., Kocan, M., Tan, X., Johnson, M.A., et al. (2020). Conformational Changes in Tyrosine 11 of Neurotensin Are Required to Activate the Neurotensin Receptor 1. ACS Pharmacol Transl Sci *3*, 690–705. https://doi.org/10.1021/acsptsci.0c00026.

Burger, W.A.C., Sexton, P.M., Christopoulos, A., and Thal, D.M. (2018). Toward an understanding of the structural basis of allostery in muscarinic acetylcholine receptors. J Gen Physiol *150*, 1360–1372. https://doi.org/10.1085/jgp.201711979.

Bymaster, F.P., Carter, P.A., Yamada, M., Gomeza, J., Wess, J., Hamilton, S.E., Nathanson, N.M., McKinzie, D.L., and Felder, C.C. (2003). Role of specific muscarinic receptor subtypes

779 in cholinergic parasympathomimetic responses, in vivo phosphoinositide hydrolysis, and
780 pilocarpine-induced seizure activity. Eur J Neurosci *17*, 1403–1410.
781 https://doi.org/10.1046/j.1460-9568.2003.02588.x.

782 Canals, M., Sexton, P.M., and Christopoulos, A. (2011). Allostery in GPCRs: "MWC" revisited.
783 Trends Biochem Sci *36*, 663–672. https://doi.org/10.1016/j.tibs.2011.08.005.

784 Cao, A.-M., Quast, R.B., Fatemi, F., Rondard, P., Pin, J.-P., and Margeat, E. (2021). Allosteric
785 modulators enhance agonist efficacy by increasing the residence time of a GPCR in the
786 active state. Nat Commun *12*, 5426. https://doi.org/10.1038/s41467-021-25620-5.

787 Cary, B.P., Deganutti, G., Zhao, P., Truong, T.T., Piper, S.J., Liu, X., Belousoff, M.J., Danev, R.,
788 Sexton, P.M., Wootten, D., et al. (2022). Structural and functional diversity among agonist-
789 bound states of the GLP-1 receptor. Nat Chem Biol *18*, 256–263.
790 https://doi.org/10.1038/s41589-021-00945-w.

791 Casañal, A., Lohkamp, B., and Emsley, P. (2020). Current developments in Coot for
792 macromolecular model building of Electron Cryo-microscopy and Crystallographic Data.
793 Protein Sci *29*, 1069–1078. https://doi.org/10.1002/pro.3791.

794 Chan, W.Y., McKinzie, D.L., Bose, S., Mitchell, S.N., Witkin, J.M., Thompson, R.C.,
795 Christopoulos, A., Lazareno, S., Birdsall, N.J.M., Bymaster, F.P., et al. (2008). Allosteric
796 modulation of the muscarinic M4 receptor as an approach to treating schizophrenia. Proc
797 Natl Acad Sci U S A *105*, 10978–10983. https://doi.org/10.1073/pnas.0800567105.

798 Changeux, J.-P., and Christopoulos, A. (2016). Allosteric Modulation as a Unifying
799 Mechanism for Receptor Function and Regulation. Cell *166*, 1084–1102.
800 https://doi.org/10.1016/j.cell.2016.08.015.

801 Christopoulos, A. (2014). Advances in G protein-coupled receptor allostery: from function to
802 structure. Mol Pharmacol *86*, 463–478. https://doi.org/10.1124/mol.114.094342.

803 Christopoulos, A., and Kenakin, T. (2002). G Protein-Coupled Receptor Allosterism and
804 Complexing. Pharmacol Rev *54*, 323–374. https://doi.org/10.1124/pr.54.2.323.

805 Cong, X., Maurel, D., Déméné, H., Vasiliauskaité-Brooks, I., Hagelberger, J., Peysson, F.,
806 Saint-Paul, J., Golebiowski, J., Granier, S., and Sounier, R. (2021). Molecular insights into the
807 biased signaling mechanism of the μ-opioid receptor. Molecular Cell S1097276521006110.
808 https://doi.org/10.1016/j.molcel.2021.07.033.

809 Conn, P.J., Jones, C.K., and Lindsley, C.W. (2009). Subtype-selective allosteric modulators of
810 muscarinic receptors for the treatment of CNS disorders. Trends Pharmacol Sci *30*, 148–155.
811 https://doi.org/10.1016/j.tips.2008.12.002.

812 Croll, T.I. (2018). ISOLDE: a physically realistic environment for model building into low-
813 resolution electron-density maps. Acta Crystallogr D Struct Biol *74*, 519–530.
814 https://doi.org/10.1107/S2059798318002425.

Danev, R., Belousoff, M., Liang, Y.-L., Zhang, X., Eisenstein, F., Wootten, D., and Sexton, P.M. (2021). Routine sub-2.5 Å cryo-EM structure determination of GPCRs. Nat Commun *12*, 4333. https://doi.org/10.1038/s41467-021-24650-3.

Darden, T., York, D., and Pedersen, L. (1993). Particle mesh Ewald: An N·log(N) method for Ewald sums in large systems. J. Chem. Phys. *98*, 10089–10092. https://doi.org/10.1063/1.464397.

Deganutti, G., Liang, Y.-L., Zhang, X., Khoshouei, M., Clydesdale, L., Belousoff, M.J., Venugopal, H., Truong, T.T., Glukhova, A., Keller, A.N., et al. (2022). Dynamics of GLP-1R peptide agonist engagement are correlated with kinetics of G protein activation. Nat Commun *13*, 92. https://doi.org/10.1038/s41467-021-27760-0.

Dencker, D., Wörtwein, G., Weikop, P., Jeon, J., Thomsen, M., Sager, T.N., Mørk, A., Woldbye, D.P.D., Wess, J., and Fink-Jensen, A. (2011). Involvement of a subpopulation of neuronal M4 muscarinic acetylcholine receptors in the antipsychotic-like effects of the M1/M4 preferring muscarinic receptor agonist xanomeline. J Neurosci *31*, 5905–5908. https://doi.org/10.1523/JNEUROSCI.0370-11.2011.

DeVree, B.T., Mahoney, J.P., Vélez-Ruiz, G.A., Rasmussen, S.G.F., Kuszak, A.J., Edwald, E., Fung, J.-J., Manglik, A., Masureel, M., Du, Y., et al. (2016). Allosteric coupling from G protein to the agonist-binding pocket in GPCRs. Nature *535*, 182–186. https://doi.org/10.1038/nature18324.

Draper-Joyce, C.J., Bhola, R., Wang, J., Bhattarai, A., Nguyen, A.T.N., Cowie-Kent, I., O'Sullivan, K., Chia, L.Y., Venugopal, H., Valant, C., et al. (2021). Positive allosteric mechanisms of adenosine A1 receptor-mediated analgesia. Nature https://doi.org/10.1038/s41586-021-03897-2.

Dror, R.O., Arlow, D.H., Maragakis, P., Mildorf, T.J., Pan, A.C., Xu, H., Borhani, D.W., and Shaw, D.E. (2011). Activation mechanism of the β2-adrenergic receptor. Proc Natl Acad Sci U S A *108*, 18684–18689. https://doi.org/10.1073/pnas.1110499108.

Dror, R.O., Mildorf, T.J., Hilger, D., Manglik, A., Borhani, D.W., Arlow, D.H., Philippsen, A., Villanueva, N., Yang, Z., Lerch, M.T., et al. (2015). SIGNAL TRANSDUCTION. Structural basis for nucleotide exchange in heterotrimeric G proteins. Science *348*, 1361–1365. https://doi.org/10.1126/science.aaa5264.

Ehlert, F.J. (1988). Estimation of the affinities of allosteric ligands using radioligand binding and pharmacological null methods. Mol Pharmacol *33*, 187–194. .

Foster, D.J., Wilson, J.M., Remke, D.H., Mahmood, M.S., Uddin, M.J., Wess, J., Patel, S., Marnett, L.J., Niswender, C.M., Jones, C.K., et al. (2016). Antipsychotic-like Effects of M4 Positive Allosteric Modulators Are Mediated by CB2 Receptor-Dependent Inhibition of Dopamine Release. Neuron *91*, 1244–1252. https://doi.org/10.1016/j.neuron.2016.08.017.

Fritze, O., Filipek, S., Kuksa, V., Palczewski, K., Hofmann, K.P., and Ernst, O.P. (2003). Role of the conserved NPxxY(x)5,6F motif in the rhodopsin ground state and during activation. Proc Natl Acad Sci U S A *100*, 2290–2295. https://doi.org/10.1073/pnas.0435715100.

Furness, S.G.B., Liang, Y.-L., Nowell, C.J., Halls, M.L., Wookey, P.J., Dal Maso, E., Inoue, A., Christopoulos, A., Wootten, D., and Sexton, P.M. (2016). Ligand-Dependent Modulation of G Protein Conformation Alters Drug Efficacy. Cell *167*, 739-749.e11. https://doi.org/10.1016/j.cell.2016.09.021.

Gentry, P.R., Kokubo, M., Bridges, T.M., Noetzel, M.J., Cho, H.P., Lamsal, A., Smith, E., Chase, P., Hodder, P.S., Niswender, C.M., et al. (2014). Development of a highly potent, novel M5 positive allosteric modulator (PAM) demonstrating CNS exposure: 1-((1H-indazol-5-yl)sulfoneyl)-N-ethyl-N-(2-(trifluoromethyl)benzyl)piperidine-4-carboxamide (ML380). J Med Chem *57*, 7804–7810. https://doi.org/10.1021/jm500995y.

Gentry, P.R., Sexton, P.M., and Christopoulos, A. (2015). Novel Allosteric Modulators of G Protein-coupled Receptors. J Biol Chem *290*, 19478–19488. https://doi.org/10.1074/jbc.R115.662759.

Gregorio, G.G., Masureel, M., Hilger, D., Terry, D.S., Juette, M., Zhao, H., Zhou, Z., Perez-Aguilar, J.M., Hauge, M., Mathiasen, S., et al. (2017). Single-molecule analysis of ligand efficacy in β2AR-G-protein activation. Nature *547*, 68–73. https://doi.org/10.1038/nature22354.

Haga, K., Kruse, A.C., Asada, H., Yurugi-Kobayashi, T., Shiroishi, M., Zhang, C., Weis, W.I., Okada, T., Kobilka, B.K., Haga, T., et al. (2012). Structure of the human M2 muscarinic acetylcholine receptor bound to an antagonist. Nature *482*, 547–551. https://doi.org/10.1038/nature10753.

Huang, J., Rauscher, S., Nawrocki, G., Ran, T., Feig, M., de Groot, B.L., Grubmüller, H., and MacKerell, A.D. (2017). CHARMM36m: an improved force field for folded and intrinsically disordered proteins. Nat Methods *14*, 71–73. https://doi.org/10.1038/nmeth.4067.

Huang, S.K., Pandey, A., Tran, D.P., Villanueva, N.L., Kitao, A., Sunahara, R.K., Sljoka, A., and Prosser, R.S. (2021). Delineating the conformational landscape of the adenosine A2A receptor during G protein coupling. Cell *184*, 1884-1894.e14. https://doi.org/10.1016/j.cell.2021.02.041.

Humphrey, W., Dalke, A., and Schulten, K. (1996). VMD: visual molecular dynamics. J Mol Graph *14*, 33–38, 27–28. https://doi.org/10.1016/0263-7855(96)00018-5.

Josephs, T.M., Belousoff, M.J., Liang, Y.-L., Piper, S.J., Cao, J., Garama, D.J., Leach, K., Gregory, K.J., Christopoulos, A., Hay, D.L., et al. (2021). Structure and dynamics of the CGRP receptor in apo and peptide-bound forms. Science *372*, eabf7258. https://doi.org/10.1126/science.abf7258.

Jumper, J., Evans, R., Pritzel, A., Green, T., Figurnov, M., Ronneberger, O., Tunyasuvunakool, K., Bates, R., Žídek, A., Potapenko, A., et al. (2021). Highly accurate protein structure prediction with AlphaFold. Nature *596*, 583–589. https://doi.org/10.1038/s41586-021-03819-2.

Katayama, K., Suzuki, K., Suno, R., Kise, R., Tsujimoto, H., Iwata, S., Inoue, A., Kobayashi, T., and Kandori, H. (2021). Vibrational spectroscopy analysis of ligand efficacy in human M2

muscarinic acetylcholine receptor (M2R). Commun Biol *4*, 1321. https://doi.org/10.1038/s42003-021-02836-1.

Kenakin, T. (2005). New concepts in drug discovery: collateral efficacy and permissive antagonism. Nat Rev Drug Discov *4*, 919–927. https://doi.org/10.1038/nrd1875.

Kenakin, T.P. (2012). Biased signalling and allosteric machines: new vistas and challenges for drug discovery. Br J Pharmacol *165*, 1659–1669. https://doi.org/10.1111/j.1476-5381.2011.01749.x.

Kenakin, T., and Onaran, O. (2002). The ligand paradox between affinity and efficacy: can you be there and not make a difference? Trends Pharmacol Sci *23*, 275–280. https://doi.org/10.1016/s0165-6147(02)02036-9.

Kenakin, T.P., Watson, C., Muniz-Medina, V., Christopoulos, A., and Novick, S. (2012). A simple method for quantifying functional selectivity and agonist bias. ACS Chem Neurosci *3*, 193–203. https://doi.org/10.1021/cn200111m.

Klauda, J.B., Venable, R.M., Freites, J.A., O'Connor, J.W., Tobias, D.J., Mondragon-Ramirez, C., Vorobyov, I., MacKerell, A.D., and Pastor, R.W. (2010). Update of the CHARMM all-atom additive force field for lipids: validation on six lipid types. J Phys Chem B *114*, 7830–7843. https://doi.org/10.1021/jp101759q.

Kruse, A.C., Hu, J., Pan, A.C., Arlow, D.H., Rosenbaum, D.M., Rosemond, E., Green, H.F., Liu, T., Chae, P.S., Dror, R.O., et al. (2012). Structure and dynamics of the M3 muscarinic acetylcholine receptor. Nature *482*, 552–556. https://doi.org/10.1038/nature10867.

Kruse, A.C., Ring, A.M., Manglik, A., Hu, J., Hu, K., Eitel, K., Hübner, H., Pardon, E., Valant, C., Sexton, P.M., et al. (2013). Activation and allosteric modulation of a muscarinic acetylcholine receptor. Nature *504*, 101–106. https://doi.org/10.1038/nature12735.

Kumar, A., Yoluk, O., and MacKerell, A.D. (2020). FFParam: Standalone package for CHARMM additive and Drude polarizable force field parametrization of small molecules. J Comput Chem *41*, 958–970. https://doi.org/10.1002/jcc.26138.

Leach, K., Sexton, P.M., and Christopoulos, A. (2007). Allosteric GPCR modulators: taking advantage of permissive receptor pharmacology. Trends Pharmacol Sci *28*, 382–389. https://doi.org/10.1016/j.tips.2007.06.004.

Leach, K., Loiacono, R.E., Felder, C.C., McKinzie, D.L., Mogg, A., Shaw, D.B., Sexton, P.M., and Christopoulos, A. (2010). Molecular mechanisms of action and in vivo validation of an M4 muscarinic acetylcholine receptor allosteric modulator with potential antipsychotic properties. Neuropsychopharmacology *35*, 855–869. https://doi.org/10.1038/npp.2009.194.

Leach, K., Davey, A.E., Felder, C.C., Sexton, P.M., and Christopoulos, A. (2011). The role of transmembrane domain 3 in the actions of orthosteric, allosteric, and atypical agonists of the M4 muscarinic acetylcholine receptor. Mol Pharmacol *79*, 855–865. https://doi.org/10.1124/mol.111.070938.

Liang, Y.-L., Zhao, P., Draper-Joyce, C., Baltos, J.-A., Glukhova, A., Truong, T.T., May, L.T., Christopoulos, A., Wootten, D., Sexton, P.M., et al. (2018a). Dominant Negative G Proteins Enhance Formation and Purification of Agonist-GPCR-G Protein Complexes for Structure Determination. ACS Pharmacol Transl Sci *1*, 12–20. https://doi.org/10.1021/acsptsci.8b00017.

Liang, Y.-L., Khoshouei, M., Glukhova, A., Furness, S.G.B., Zhao, P., Clydesdale, L., Koole, C., Truong, T.T., Thal, D.M., Lei, S., et al. (2018b). Phase-plate cryo-EM structure of a biased agonist-bound human GLP-1 receptor-Gs complex. Nature *555*, 121–125. https://doi.org/10.1038/nature25773.

Liang, Y.-L., Belousoff, M.J., Fletcher, M.M., Zhang, X., Khoshouei, M., Deganutti, G., Koole, C., Furness, S.G.B., Miller, L.J., Hay, D.L., et al. (2020). Structure and Dynamics of Adrenomedullin Receptors AM1 and AM2 Reveal Key Mechanisms in the Control of Receptor Phenotype by Receptor Activity-Modifying Proteins. ACS Pharmacol Transl Sci *3*, 263–284. https://doi.org/10.1021/acsptsci.9b00080.

Liebschner, D., Afonine, P.V., Baker, M.L., Bunkóczi, G., Chen, V.B., Croll, T.I., Hintze, B., Hung, L.W., Jain, S., McCoy, A.J., et al. (2019). Macromolecular structure determination using X-rays, neutrons and electrons: recent developments in Phenix. Acta Crystallogr D Struct Biol *75*, 861–877. https://doi.org/10.1107/S2059798319011471.

Liu, J.J., Horst, R., Katritch, V., Stevens, R.C., and Wüthrich, K. (2012a). Biased signaling pathways in β2-adrenergic receptor characterized by 19F-NMR. Science *335*, 1106–1110. https://doi.org/10.1126/science.1215802.

Liu, W., Chun, E., Thompson, A.A., Chubukov, P., Xu, F., Katritch, V., Han, G.W., Roth, C.B., Heitman, L.H., IJzerman, A.P., et al. (2012b). Structural Basis for Allosteric Regulation of GPCRs by Sodium Ions. Science *337*, 232–236. https://doi.org/10.1126/science.1219218.

Maeda, S., Koehl, A., Matile, H., Hu, H., Hilger, D., Schertler, G.F.X., Manglik, A., Skiniotis, G., Dawson, R.J.P., and Kobilka, B.K. (2018). Development of an antibody fragment that stabilizes GPCR/G-protein complexes. Nat Commun *9*, 3712. https://doi.org/10.1038/s41467-018-06002-w.

Maeda, S., Qu, Q., Robertson, M.J., Skiniotis, G., and Kobilka, B.K. (2019). Structures of the M1 and M2 muscarinic acetylcholine receptor/G-protein complexes. Science *364*, 552–557. https://doi.org/10.1126/science.aaw5188.

Manglik, A., Kim, T.H., Masureel, M., Altenbach, C., Yang, Z., Hilger, D., Lerch, M.T., Kobilka, T.S., Thian, F.S., Hubbell, W.L., et al. (2015). Structural Insights into the Dynamic Process of β2-Adrenergic Receptor Signaling. Cell *161*, 1101–1111. https://doi.org/10.1016/j.cell.2015.04.043.

Marlo, J.E., Niswender, C.M., Days, E.L., Bridges, T.M., Xiang, Y., Rodriguez, A.L., Shirey, J.K., Brady, A.E., Nalywajko, T., Luo, Q., et al. (2009). Discovery and Characterization of Novel Allosteric Potentiators of M1 Muscarinic Receptors Reveals Multiple Modes of Activity. Mol Pharmacol *75*, 577–588. https://doi.org/10.1124/mol.108.052886.

970 Masureel, M., Zou, Y., Picard, L.-P., van der Westhuizen, E., Mahoney, J.P., Rodrigues,
971 J.P.G.L.M., Mildorf, T.J., Dror, R.O., Shaw, D.E., Bouvier, M., et al. (2018). Structural insights
972 into binding specificity, efficacy and bias of a β2AR partial agonist. Nat Chem Biol *14*, 1059–
973 1066. https://doi.org/10.1038/s41589-018-0145-x.

974 McCorvy, J.D., Wacker, D., Wang, S., Agegnehu, B., Liu, J., Lansu, K., Tribo, A.R., Olsen, R.H.J.,
975 Che, T., Jin, J., et al. (2018). Structural determinants of 5-HT2B receptor activation and
976 biased agonism. Nat Struct Mol Biol *25*, 787–796. https://doi.org/10.1038/s41594-018-
977 0116-7.

978 Miao, Y., and McCammon, J.A. (2016). Graded activation and free energy landscapes of a
979 muscarinic G-protein-coupled receptor. Proc Natl Acad Sci U S A *113*, 12162–12167.
980 https://doi.org/10.1073/pnas.1614538113.

981 Miao, Y., and McCammon, J.A. (2017). Gaussian Accelerated Molecular Dynamics: Theory,
982 Implementation, and Applications. Annu Rep Comput Chem *13*, 231–278.
983 https://doi.org/10.1016/bs.arcc.2017.06.005.

984 Miao, Y., and McCammon, J.A. (2018). Mechanism of the G-protein mimetic nanobody
985 binding to a muscarinic G-protein-coupled receptor. Proc Natl Acad Sci U S A *115*, 3036–
986 3041. https://doi.org/10.1073/pnas.1800756115.

987 Miao, Y., Sinko, W., Pierce, L., Bucher, D., Walker, R.C., and McCammon, J.A. (2014).
988 Improved Reweighting of Accelerated Molecular Dynamics Simulations for Free Energy
989 Calculation. J Chem Theory Comput *10*, 2677–2689. https://doi.org/10.1021/ct500090q.

990 Miao, Y., Feher, V.A., and McCammon, J.A. (2015). Gaussian Accelerated Molecular
991 Dynamics: Unconstrained Enhanced Sampling and Free Energy Calculation. J. Chem. Theory
992 Comput. *11*, 3584–3595. https://doi.org/10.1021/acs.jctc.5b00436.

993 Mobbs, J.I., Belousoff, M.J., Harikumar, K.G., Piper, S.J., Xu, X., Furness, S.G.B., Venugopal,
994 H., Christopoulos, A., Danev, R., Wootten, D., et al. (2021). Structures of the human
995 cholecystokinin 1 (CCK1) receptor bound to Gs and Gq mimetic proteins provide insight into
996 mechanisms of G protein selectivity. PLoS Biol *19*, e3001295.
997 https://doi.org/10.1371/journal.pbio.3001295.

998 Nawaratne, V., Leach, K., Felder, C.C., Sexton, P.M., and Christopoulos, A. (2010). Structural
999 determinants of allosteric agonism and modulation at the M4 muscarinic acetylcholine
1000 receptor: identification of ligand-specific and global activation mechanisms. J Biol Chem *285*,
1001 19012–19021. https://doi.org/10.1074/jbc.M110.125096.

1002 Nygaard, R., Frimurer, T.M., Holst, B., Rosenkilde, M.M., and Schwartz, T.W. (2009). Ligand
1003 binding and micro-switches in 7TM receptor structures. Trends Pharmacol Sci *30*, 249–259.
1004 https://doi.org/10.1016/j.tips.2009.02.006.

1005 O'Connor, C., White, K.L., Doncescu, N., Didenko, T., Roth, B.L., Czaplicki, G., Stevens, R.C.,
1006 Wüthrich, K., and Milon, A. (2015). NMR structure and dynamics of the agonist dynorphin
1007 peptide bound to the human kappa opioid receptor. Proc Natl Acad Sci U S A *112*, 11852–
1008 11857. https://doi.org/10.1073/pnas.1510117112.

1009 Olsen, R.H.J., DiBerto, J.F., English, J.G., Glaudin, A.M., Krumm, B.E., Slocum, S.T., Che, T.,
1010 Gavin, A.C., McCorvy, J.D., Roth, B.L., et al. (2020). TRUPATH, an open-source biosensor
1011 platform for interrogating the GPCR transducerome. Nat Chem Biol *16*, 841–849.
1012 https://doi.org/10.1038/s41589-020-0535-8.

1013 Pani, B., Ahn, S., Rambarat, P.K., Vege, S., Kahsai, A.W., Liu, A., Valan, B.N., Staus, D.P.,
1014 Costa, T., and Lefkowitz, R.J. (2021). Unique Positive Cooperativity Between the β-Arrestin-
1015 Biased β-Blocker Carvedilol and a Small Molecule Positive Allosteric Modulator of the β2-
1016 Adrenergic Receptor. Mol Pharmacol *100*, 513–525.
1017 https://doi.org/10.1124/molpharm.121.000363.

1018 Pettersen, E.F., Goddard, T.D., Huang, C.C., Couch, G.S., Greenblatt, D.M., Meng, E.C., and
1019 Ferrin, T.E. (2004). UCSF Chimera--a visualization system for exploratory research and
1020 analysis. J Comput Chem *25*, 1605–1612. https://doi.org/10.1002/jcc.20084.

1021 Pettersen, E.F., Goddard, T.D., Huang, C.C., Meng, E.C., Couch, G.S., Croll, T.I., Morris, J.H.,
1022 and Ferrin, T.E. (2021). UCSF ChimeraX: Structure visualization for researchers, educators,
1023 and developers. Protein Sci *30*, 70–82. https://doi.org/10.1002/pro.3943.

1024 Phillips, J.C., Braun, R., Wang, W., Gumbart, J., Tajkhorshid, E., Villa, E., Chipot, C., Skeel,
1025 R.D., Kalé, L., and Schulten, K. (2005). Scalable molecular dynamics with NAMD. J Comput
1026 Chem *26*, 1781–1802. https://doi.org/10.1002/jcc.20289.

1027 Punjani, A., and Fleet, D.J. (2021). 3D variability analysis: Resolving continuous flexibility and
1028 discrete heterogeneity from single particle cryo-EM. J Struct Biol *213*, 107702.
1029 https://doi.org/10.1016/j.jsb.2021.107702.

1030 Qi, X., Liu, H., Thompson, B., McDonald, J., Zhang, C., and Li, X. (2019). Cryo-EM structure of
1031 oxysterol-bound human Smoothened coupled to a heterotrimeric Gi. Nature *571*, 279–283.
1032 https://doi.org/10.1038/s41586-019-1286-0.

1033 Rasmussen, S.G.F., Choi, H.-J., Fung, J.J., Pardon, E., Casarosa, P., Chae, P.S., DeVree, B.T.,
1034 Rosenbaum, D.M., Thian, F.S., Kobilka, T.S., et al. (2011). Structure of a nanobody-stabilized
1035 active state of the β2 adrenoceptor. Nature *469*, 175–180.
1036 https://doi.org/10.1038/nature09648.

1037 Roe, D.R., and Cheatham, T.E. (2013). PTRAJ and CPPTRAJ: Software for Processing and
1038 Analysis of Molecular Dynamics Trajectory Data. J Chem Theory Comput *9*, 3084–3095.
1039 https://doi.org/10.1021/ct400341p.

1040 Ryckaert, J.-P., Ciccotti, G., and Berendsen, H.J.C. (1977). Numerical integration of the
1041 cartesian equations of motion of a system with constraints: molecular dynamics of n-
1042 alkanes. Journal of Computational Physics *23*, 327–341. https://doi.org/10.1016/0021-
1043 9991(77)90098-5.

1044 Schrage, R., Seemann, W.K., Klöckner, J., Dallanoce, C., Racké, K., Kostenis, E., De Amici, M.,
1045 Holzgrabe, U., and Mohr, K. (2013). Agonists with supraphysiological efficacy at the
1046 muscarinic M2 ACh receptor. Br J Pharmacol *169*, 357–370.
1047 https://doi.org/10.1111/bph.12003.

1048 Seyedabadi, M., Gharghabi, M., Gurevich, E.V., and Gurevich, V.V. (2022). Structural basis of
1049 GPCR coupling to distinct signal transducers: implications for biased signaling. Trends
1050 Biochem Sci *47*, 570–581. https://doi.org/10.1016/j.tibs.2022.03.009.

1051 Shi, L., Liapakis, G., Xu, R., Guarnieri, F., Ballesteros, J.A., and Javitch, J.A. (2002). Beta2
1052 adrenergic receptor activation. Modulation of the proline kink in transmembrane 6 by a
1053 rotamer toggle switch. J Biol Chem *277*, 40989–40996.
1054 https://doi.org/10.1074/jbc.M206801200.

1055 Slosky, L.M., Bai, Y., Toth, K., Ray, C., Rochelle, L.K., Badea, A., Chandrasekhar, R., Pogorelov,
1056 V.M., Abraham, D.M., Atluri, N., et al. (2020). β-Arrestin-Biased Allosteric Modulator of
1057 NTSR1 Selectively Attenuates Addictive Behaviors. Cell *181*, 1364-1379.e14.
1058 https://doi.org/10.1016/j.cell.2020.04.053.

1059 Slosky, L.M., Caron, M.G., and Barak, L.S. (2021). Biased Allosteric Modulators: New
1060 Frontiers in GPCR Drug Discovery. Trends in Pharmacological Sciences *42*, 283–299.
1061 https://doi.org/10.1016/j.tips.2020.12.005.

1062 Solt, A.S., Bostock, M.J., Shrestha, B., Kumar, P., Warne, T., Tate, C.G., and Nietlispach, D.
1063 (2017). Insight into partial agonism by observing multiple equilibria for ligand-bound and Gs-
1064 mimetic nanobody-bound β1-adrenergic receptor. Nat Commun *8*, 1795.
1065 https://doi.org/10.1038/s41467-017-02008-y.

1066 Staus, D.P., Hu, H., Robertson, M.J., Kleinhenz, A.L.W., Wingler, L.M., Capel, W.D., Latorraca,
1067 N.R., Lefkowitz, R.J., and Skiniotis, G. (2020). Structure of the M2 muscarinic receptor-β-
1068 arrestin complex in a lipid nanodisc. Nature *579*, 297–302. https://doi.org/10.1038/s41586-
1069 020-1954-0.

1070 Suratman, S., Leach, K., Sexton, P., Felder, C., Loiacono, R., and Christopoulos, A. (2011).
1071 Impact of species variability and “probe-dependence” on the detection and in vivo
1072 validation of allosteric modulation at the M4 muscarinic acetylcholine receptor. Br J
1073 Pharmacol *162*, 1659–1670. https://doi.org/10.1111/j.1476-5381.2010.01184.x.

1074 Sušac, L., Eddy, M.T., Didenko, T., Stevens, R.C., and Wüthrich, K. (2018). A2A adenosine
1075 receptor functional states characterized by 19F-NMR. Proc Natl Acad Sci U S A *115*, 12733–
1076 12738. https://doi.org/10.1073/pnas.1813649115.

1077 Terashi, G., Wang, X., Maddhuri Venkata Subramaniya, S.R., Tesmer, J.J.G., and Kihara, D.
1078 (2022). Residue-wise local quality estimation for protein models from cryo-EM maps. Nat
1079 Methods *19*, 1116–1125. https://doi.org/10.1038/s41592-022-01574-4.

1080 Thal, D.M., Sun, B., Feng, D., Nawaratne, V., Leach, K., Felder, C.C., Bures, M.G., Evans, D.A.,
1081 Weis, W.I., Bachhawat, P., et al. (2016). Crystal structures of the M1 and M4 muscarinic
1082 acetylcholine receptors. Nature *531*, 335–340. https://doi.org/10.1038/nature17188.

1083 Thal, D.M., Glukhova, A., Sexton, P.M., and Christopoulos, A. (2018). Structural insights into
1084 G-protein-coupled receptor allostery. Nature *559*, 45–53. https://doi.org/10.1038/s41586-
1085 018-0259-z.

Tian, W., Chen, C., Lei, X., Zhao, J., and Liang, J. (2018). CASTp 3.0: computed atlas of surface topography of proteins. Nucleic Acids Res *46*, W363–W367. https://doi.org/10.1093/nar/gky473.

Tzavara, E.T., Bymaster, F.P., Davis, R.J., Wade, M.R., Perry, K.W., Wess, J., McKinzie, D.L., Felder, C., and Nomikos, G.G. (2004). M4 muscarinic receptors regulate the dynamics of cholinergic and dopaminergic neurotransmission: relevance to the pathophysiology and treatment of related CNS pathologies. FASEB J *18*, 1410–1412. https://doi.org/10.1096/fj.04-1575fje.

Valant, C., Felder, C.C., Sexton, P.M., and Christopoulos, A. (2012). Probe dependence in the allosteric modulation of a G protein-coupled receptor: implications for detection and validation of allosteric ligand effects. Mol Pharmacol *81*, 41–52. https://doi.org/10.1124/mol.111.074872.

Vanommeslaeghe, K., and MacKerell, A.D. (2012). Automation of the CHARMM General Force Field (CGenFF) I: bond perception and atom typing. J Chem Inf Model *52*, 3144–3154. https://doi.org/10.1021/ci300363c.

Vanommeslaeghe, K., and MacKerell, A.D. (2015). CHARMM additive and polarizable force fields for biophysics and computer-aided drug design. Biochim Biophys Acta *1850*, 861–871. https://doi.org/10.1016/j.bbagen.2014.08.004.

Vanommeslaeghe, K., Raman, E.P., and MacKerell, A.D. (2012). Automation of the CHARMM General Force Field (CGenFF) II: assignment of bonded parameters and partial atomic charges. J Chem Inf Model *52*, 3155–3168. https://doi.org/10.1021/ci3003649.

Varadi, M., Anyango, S., Deshpande, M., Nair, S., Natassia, C., Yordanova, G., Yuan, D., Stroe, O., Wood, G., Laydon, A., et al. (2022). AlphaFold Protein Structure Database: massively expanding the structural coverage of protein-sequence space with high-accuracy models. Nucleic Acids Res *50*, D439–D444. https://doi.org/10.1093/nar/gkab1061.

Vuckovic, Z., Gentry, P.R., Berizzi, A.E., Hirata, K., Varghese, S., Thompson, G., van der Westhuizen, E.T., Burger, W.A.C., Rahmani, R., Valant, C., et al. (2019). Crystal structure of the M5 muscarinic acetylcholine receptor. Proc Natl Acad Sci U S A *116*, 26001–26007. https://doi.org/10.1073/pnas.1914446116.

Wacker, D., Wang, C., Katritch, V., Han, G.W., Huang, X.-P., Vardy, E., McCorvy, J.D., Jiang, Y., Chu, M., Siu, F.Y., et al. (2013). Structural features for functional selectivity at serotonin receptors. Science *340*, 615–619. https://doi.org/10.1126/science.1232808.

Wagner, T., Merino, F., Stabrin, M., Moriya, T., Antoni, C., Apelbaum, A., Hagel, P., Sitsel, O., Raisch, T., Prumbaum, D., et al. (2019). SPHIRE-crYOLO is a fast and accurate fully automated particle picker for cryo-EM. Commun Biol *2*, 218. https://doi.org/10.1038/s42003-019-0437-z.

Wang, J., Arantes, P.R., Bhattarai, A., Hsu, R.V., Pawnikar, S., Huang, Y.-M.M., Palermo, G., and Miao, Y. (2021a). Gaussian accelerated molecular dynamics (GaMD): principles and

applications. Wiley Interdiscip Rev Comput Mol Sci *11*, e1521. https://doi.org/10.1002/wcms.1521.

Wang, J., Pani, B., Gokhan, I., Xiong, X., Kahsai, A.W., Jiang, H., Ahn, S., Lefkowitz, R.J., and Rockman, H.A. (2021b). β-Arrestin-Biased Allosteric Modulator Potentiates Carvedilol-Stimulated β Adrenergic Receptor Cardioprotection. Mol Pharmacol *100*, 568–579. https://doi.org/10.1124/molpharm.121.000359.

Wang, J., Wu, M., Chen, Z., Wu, L., Wang, T., Cao, D., Wang, H., Liu, S., Xu, Y., Li, F., et al. (2022). The unconventional activation of the muscarinic acetylcholine receptor M4R by diverse ligands. Nat Commun *13*, 2855. https://doi.org/10.1038/s41467-022-30595-y.

Warne, T., Edwards, P.C., Leslie, A.G.W., and Tate, C.G. (2012). Crystal structures of a stabilized β1-adrenoceptor bound to the biased agonists bucindolol and carvedilol. Structure *20*, 841–849. https://doi.org/10.1016/j.str.2012.03.014.

Warne, T., Edwards, P.C., Doré, A.S., Leslie, A.G.W., and Tate, C.G. (2019). Molecular basis for high-affinity agonist binding in GPCRs. Science *364*, 775–778. https://doi.org/10.1126/science.aau5595.

White, K.L., Eddy, M.T., Gao, Z.-G., Han, G.W., Lian, T., Deary, A., Patel, N., Jacobson, K.A., Katritch, V., and Stevens, R.C. (2018). Structural Connection between Activation Microswitch and Allosteric Sodium Site in GPCR Signaling. Structure *26*, 259-269.e5. https://doi.org/10.1016/j.str.2017.12.013.

Williams, C.J., Headd, J.J., Moriarty, N.W., Prisant, M.G., Videau, L.L., Deis, L.N., Verma, V., Keedy, D.A., Hintze, B.J., Chen, V.B., et al. (2018). MolProbity: More and better reference data for improved all-atom structure validation. Protein Sci *27*, 293–315. https://doi.org/10.1002/pro.3330.

Wingler, L.M., Elgeti, M., Hilger, D., Latorraca, N.R., Lerch, M.T., Staus, D.P., Dror, R.O., Kobilka, B.K., Hubbell, W.L., and Lefkowitz, R.J. (2019). Angiotensin Analogs with Divergent Bias Stabilize Distinct Receptor Conformations. Cell *176*, 468-478.e11. https://doi.org/10.1016/j.cell.2018.12.005.

Wood, M.R., Noetzel, M.J., Poslusney, M.S., Melancon, B.J., Tarr, J.C., Lamsal, A., Chang, S., Luscombe, V.B., Weiner, R.L., Cho, H.P., et al. (2017a). Challenges in the development of an M4 PAM in vivo tool compound: The discovery of VU0467154 and unexpected DMPK profiles of close analogs. Bioorg Med Chem Lett *27*, 171–175. https://doi.org/10.1016/j.bmcl.2016.11.086.

Wood, M.R., Noetzel, M.J., Melancon, B.J., Poslusney, M.S., Nance, K.D., Hurtado, M.A., Luscombe, V.B., Weiner, R.L., Rodriguez, A.L., Lamsal, A., et al. (2017b). Discovery of VU0467485/AZ13713945: An M4 PAM Evaluated as a Preclinical Candidate for the Treatment of Schizophrenia. ACS Med Chem Lett *8*, 233–238. https://doi.org/10.1021/acsmedchemlett.6b00461.

Wootten, D., Christopoulos, A., and Sexton, P.M. (2013). Emerging paradigms in GPCR allostery: implications for drug discovery. Nat Rev Drug Discov *12*, 630–644. https://doi.org/10.1038/nrd4052.

Xu, J., Hu, Y., Kaindl, J., Risel, P., Hübner, H., Maeda, S., Niu, X., Li, H., Gmeiner, P., Jin, C., et al. (2019). Conformational Complexity and Dynamics in a Muscarinic Receptor Revealed by NMR Spectroscopy. Mol Cell *75*, 53-65.e7. https://doi.org/10.1016/j.molcel.2019.04.028.

Xu, J., Hübner, H., Hu, Y., Niu, X., Gmeiner, P., Jin, C., and Kobilka, B. (2021). An allosteric ligand stabilizes distinct conformations in the M2 muscarinic acetylcholine receptor. 2021.02.14.431178. https://doi.org/10.1101/2021.02.14.431178.

Ye, L., Van Eps, N., Zimmer, M., Ernst, O.P., and Prosser, R.S. (2016). Activation of the A2A adenosine G-protein-coupled receptor by conformational selection. Nature *533*, 265–268. https://doi.org/10.1038/nature17668.

Zhang, K. (2016). Gctf: Real-time CTF determination and correction. J Struct Biol *193*, 1–12. https://doi.org/10.1016/j.jsb.2015.11.003.

Zhang, X., Belousoff, M.J., Zhao, P., Kooistra, A.J., Truong, T.T., Ang, S.Y., Underwood, C.R., Egebjerg, T., Šenel, P., Stewart, G.D., et al. (2020). Differential GLP-1R Binding and Activation by Peptide and Non-peptide Agonists. Molecular Cell *80*, 485-500.e7. https://doi.org/10.1016/j.molcel.2020.09.020.

Zheng, S.Q., Palovcak, E., Armache, J.-P., Verba, K.A., Cheng, Y., and Agard, D.A. (2017). MotionCor2 - anisotropic correction of beam-induced motion for improved cryo-electron microscopy. Nat Methods *14*, 331–332. https://doi.org/10.1038/nmeth.4193.

Zhou, Q., Yang, D., Wu, M., Guo, Y., Guo, W., Zhong, L., Cai, X., Dai, A., Jang, W., Shakhnovich, E.I., et al. (2019). Common activation mechanism of class A GPCRs. Elife *8*, e50279. https://doi.org/10.7554/eLife.50279.

Zivanov, J., Nakane, T., Forsberg, B.O., Kimanius, D., Hagen, W.J., Lindahl, E., and Scheres, S.H. (2018). New tools for automated high-resolution cryo-EM structure determination in RELION-3. Elife *7*, e42166. https://doi.org/10.7554/eLife.42166.

Materials and Methods

Key Resources Table

Reagent type (species) or resource	Designation	Source or reference	Additional information
antibody	anti-FLAG M1 (mouse IgG2a)	Gift from Prof. Brian Kobilka (PMID 17962520)	Antibody used for purification of FLAG-tagged M4 mAChR.
strain, strain background (*E. coli*)	DH5α	New England Biolabs	
strain, strain background (*E. coli*)	DH10bac	Thermo-Fisher Scientific	
cell line (*Spodoptera frugiperda*)	Sf9	Expression Systems	
cell line (*Trichoplusia ni*)	Tni	Expression Systems	
cell line (Chinese hamster ovary)	Flp-In CHO human M4 mAChR WT	PMID: 26958838	
cell line (Chinese hamster ovary)	CHO K1 mouse M4 mAChR WT	PMID: 21198541	
cell line (Chinese hamster ovary)	Flp-In CHO human M4 mAChR D432E	This study	pEF5-FRT-V5-DEST plasmid
cell line (Chinese hamster ovary)	Flp-In CHO human M4 mAChR T433R	This study	pEF5-FRT-V5-DEST plasmid
cell line (Chinese hamster ovary)	Flp-In CHO human M4 mAChR V91L, D432E, T433R	This study	pEF5-FRT-V5-DEST plasmid
cell line (Chinese hamster ovary)	Flp-In CHO human M4 mAChR Y89A	PMID: 26958838	
cell line (Chinese hamster ovary)	Flp-In CHO human M4 mAChR Q184A	PMID: 26958838	
cell line (Chinese hamster ovary)	Flp-In CHO human M4 mAChR F186A	PMID: 20406819	
cell line (Chinese hamster ovary)	Flp-In CHO human M4 mAChR W435A	PMID: 26958838	
cell line (Chinese hamster ovary)	Flp-In CHO human M4 mAChR W439A	PMID: 20406819	
cell line (*Homo sapiens*)	HEK293A	Thermo-Fisher Scientific	
recombinant DNA reagent	human FLAG-M4Δi3-His	This study	pVL1392 vector
recombinant DNA reagent	human Gαi1 dominant negative mutant	PMID: 32193322	pFastBac vector
recombinant DNA reagent	human Gβ1γ2	Gift from Prof. Brian Kobilka (PMID 24256733)	pVL1392 vector
recombinant DNA reagent	scFv16	PMID: 30213947	pFastBac vector
recombinant DNA reagent	pcDNA5/FRT/TO-GAlphai1-RLuc8	Gift from Prof. Bryan Roth (PMID 32367019)	TRUPATH assay
recombinant DNA reagent	pcDNA3.1-Beta3	Gift from Prof. Bryan Roth (PMID 32367019)	TRUPATH assay
recombinant DNA reagent	pcDNA3.1-GGamma9-GFP2	Gift from Prof. Bryan Roth (PMID 32367019)	TRUPATH assay
chemical compound, drug	Acetylcholine	Sigma-Aldrich	
chemical compound, drug	Iperoxo	Sigma-Aldrich	
chemical compound, drug	LY2033298	Sigma-Aldrich	
chemical compound, drug	VU0467154	Gift from Prof. Craig Lindsley (PMID 25137629)	PMID 25137629
chemical compound, drug	Prolume Purple	Nanolight Technology	

chemical compound, drug	[3H]-NMS	PerkinElmer	
chemical compound, drug	Polyethylenimine (PEI)	Sigma-Aldrich	
chemical compound, drug	Atropine	Sigma-Aldrich	
commercial assay or kit	AlphaScreen® SureFire® p-ERK 1/2 (Thr202/Tyr204) Assay Kits	PerkinElmer	
software, algorithm	Prism 8.0	GraphPad	
software, algorithm	Pymol	Schrödinger	
software, algorithm	GaMD	PMID: 26300708	
software, algorithm	AMBER20	https://ambermd.org	
software, algorithm	CPPTRAJ	PMID: 26300708	
software, algorithm	PyReweighting	PMID: 25061441	
software, algorithm	Phenix suite	PMID: 20124702	
software, algorithm	Coot	PMID: 31730249	
software, algorithm	Chimera	PMID: 15264254	
software, algorithm	Chimera X	PMID: 32881101	
software, algorithm	cryoSPARC	PMID: 28165473	
software, algorithm	Relion 3.1	PMID: 30412051	
software, algorithm	Motioncor2	PMID: 28250466	
software, algorithm	GCTF	PMID: 26592709	
software, algorithm	crYOLO	PMID: 31240256	
software, algorithm	ISOLDE	PMID: 29872003	
software, algorithm	Molprobity	PMID: 29067766	
software, algorithm	DAQ Score	PMID: 35953671	

Bacterial strains

DH5α (New England Biolabs) and DH10bac () *E. coli* cells were grown in LB at 37°C.

Insect cell culture

Tni and Sf9 cells (Expression Systems) were maintained in ESF-921 media (Expression Systems) at 27°C.

Mammalian cell culture

Flp-In Chinese hamster ovary (CHO) (Thermo-Fisher Scientific) cells stably expressing human M_4 mAChR or mutant constructs were maintained in Dulbecco's modified Eagle's medium (DMEM, Invitrogen) containing 5% fetal bovine serum (FBS; ThermoTrace) and 0.6 μg/ml of

Hygromycin (Roche) in a humidified incubator (37°C, 5% CO_2, 95% O_2). HEK293A cells were grown in DMEM supplemented with 5% FBS at 37°C in 5% CO_2.

Radioligand binding assays

Flp-In CHO cells stably expressing M_4 mAChR constructs were seeded at 10,000 cells/well in 96-well white clear bottom isoplates (Greiner Bio-one) and allowed to adhere overnight at 37°C, 5% CO_2, and 95% O_2. Saturation binding assay was performed to quantify the receptor expression and equilibrium dissociation constant of the radioligand [^{3}H]-NMS (PerkinElmer, specific activity 80 Ci/mmol). Briefly, plates were washed once with phosphate-buffered saline (PBS) and incubated overnight at room temperature (RT) with 0.01-10 nM [^{3}H]-NMS in Hanks's balanced salt solution (HBSS)/10 mM HEPES (pH 7.4) in a final volume of 100 µl. For binding interaction assays, cells were incubated overnight at RT with a specific concentration of [^{3}H]-NMS (pK_D determined at each receptor in saturation binding) and various concentrations of ACh or iperoxo (Ipx) in the absence or presence of increasing concentrations of each allosteric modulator. In all cases, nonspecific binding was determined by the coaddition of 10 µM atropine (Sigma). The following day, the assays were terminated by washing the plates twice with ice-cold 0.9% NaCl to remove the unbound radioligand. Cells were solubilised in 100 µl per well of Ultima Gold (PerkinElmer), and radioactivity was measured with a MicroBeta plate reader (PerkinElmer).

G protein activation assay

Upon 60-80% confluence, HEK293A cells were transfected transiently using polyethylenimine (PEI, Polysciences) and 10 ng per well of each of pcDNA3.1-hM4 mAChR (WT or mutant), pcDNA5/FRT/TO-Gα_{i1}-RLuc8, pcDNA3.1-β_3, and pcDNA3.1-Gγ_9-GFP2 at a ratio of 1:1:1:1 ratio with 40 ng of total DNA per well. Cells were plated at 30,000 cells per well into 96-well Greiner CELLSTAR white-walled plates (Sigma Aldrich). 48 hrs later, cells were washed with 200 µL phosphate buffer saline (PBS) and replaced with 70 µL of 1x HBSS with 10 mM HEPES. Cells were incubated for 30 min at 37°C before addition of 10 µL of 1.3 µM Prolume Purple coelenterazine (Nanolight technology). Cells were further incubated for 10 min at 37C° before BRET measurements were performed on a PHERAstar plate reader (BMG Labtech) using 410/80-nm and 515/30-nm filters. Baseline measurements were taken for 8 min before addition of drugs or vehicle to give a final assay volume of 100 µL and further reading for 30

min. BRET signal was calculated as the ratio of 515/30-nm emission over 410/80-nm emission. The ratio was vehicle corrected using the initial 8 min of baseline measurements and then baseline corrected again using the vehicle-treated wells. Data were normalized using the maximum agonist response to allow for grouping of results using an area under the curve analysis in Prism. Data were analysed at timepoints of 4, 10, and 30 min yielding similar results.

Phospho-ERK1/2 assay

The level of phosphorylated extracellular signal-regulated protein kinase 1/2 (pERK1/2) was detected using the AlphaScreen^{TM} SureFire Kit (PerkinElmer Life and Analytical Sciences). Briefly, FlpIn CHO cells stably expressing the receptor were seeded into transparent 96-well plates at a density of 20,000 cells/well and grown overnight at 37^{o}C, 5% CO_2. Cells were washed with PBS and incubated in serum-free DMEM at 37^{o}C for 4 hr to allow FBS-stimulated pERK1/2 levels to subside. Cells were stimulated with increasing concentrations of ACh or Ipx in the absence or presence of increasing concentrations of the allosteric modulator at 37^{o}C for 5 min (the time required to maximally promote ERK phosphorylation for each ligand at each M_4 mAChR construct in the initial time-course study; data not shown). For all experiments, stimulation with 10% (*v/v*) FBS for 5 min was used as a positive control. The reaction was terminated by the removal of media and lysis of cells with 50 μl of the SureFire lysis buffer (TGR Biosciences). Plates were then agitated for 5 min and 5 μl of the cell lysate was transferred to a white 384-well ProxiPlate (Greiner Bio-one) followed by the addition of 5 μl of the detection buffer (a mixture of activation buffer: reaction buffer: acceptor beads: donor beads at a ratio of 50:200:1:1). Plates were incubated in the dark for 1 hr at 37^{o}C followed by measurement of fluorescence using an Envision plate reader (PerkinElmer) with standard AlphaScreen^{TM} settings. Data were normalised to the maximal response mediated by 10 μM ACh, Ipx or 10% FBS.

Purification of scFv16

Tni insect cells were infected with scFv16 baculovirus at a density of 4 million cells per mL and harvested at 60 hrs post infection by centrifugation for 10 min at 10,000xg. The supernatant was pH balanced to pH 7.5 by the addition of Tris pH 7.5, and 5 mM $CaCl_2$ was added to

quench any chelating agents, then left to stir for 1.5 hrs at RT. The supernatant was then centrifuged at 30,000xg for 15 min to remove any precipitates. 5 mL of EDTA resistant Ni resin (Cytivia) was added and incubated for 2 hrs at 4°C while stirring. Resin was collected in a glass column and washed with 20 column volumes (CVs) of high salt buffer (20 mM HEPES pH 7.5, 500 mM NaCl, 20 mM imidazole) followed by 20 CVs of low salt buffer (20 mM HEPES pH 7.5, 100 mM NaCl, 20 mM Imidazole). Protein was then eluted using 8 CV of elution buffer (20 mM HEPES pH 7.5, 100 mM NaCl, 250 mM imidazole) until no more protein was detected using Bradford reagent (Bio-Rad Laboratories). Protein was concentrated using a 10-kDa Amicon filter device (Millipore) and aliquoted into 1 mg aliquots for further use.

Expression and purification of M_4R-G_{i1}-scFv16 complexes

The human M_4 mAChR with residues 242 to 387 of the third intracellular loop removed and the N-terminal glycosylation sites (N3, N9, N13) mutated to D was expressed in Sf9 insect cells, and human DN$G_{\alpha i1}$ and His6-tagged human $G_{\beta 1\gamma 2}$ were co-expressed in Tni insect cells. Cell cultures were grown to a density of 4 million cell per ml for Sf9 cells and 3.6 million per ml for Tni cells and then infected with either M_4 mAChR baculovirus or both $G_{\alpha i1}$ and $G_{\beta 1\gamma 2}$ baculovirus, at a ratio of 1:1. M_4 mAChR expression was supplemented with 10 mM atropine. Cultures were grown at 27°C and harvested by centrifugation 60-72 hr (48 h for Hi5 cells) post infection. Cells were frozen and stored at -80°C for later use. 1-2 L of the frozen cells were used for each purification.

Cells expressing M_4 mAChR were thawed at RT and then dounced in the solubilization buffer containing: 20 mM HEPES pH 7.5, 10% glycerol, 750 mM NaCl, 5 mM $MgCl_2$, 5 mM $CaCl_2$, 0.5% LMNG, 0.02% CHS, 10 µM atropine and cOmplete protease inhibitor cocktail (Roche) until homogenous. The receptor was solubilized for 2 hrs at 4°C while stirring. The insoluble material was removed by centrifugation at 30,000xg for 30 min followed by filtering the supernatant and batch-binding immobilization to M1 anti-flag affinity resin, previously equilibrated with high salt buffer, for 1 hr at RT. The resin with immobilized receptor was then washed using a peristaltic pump for 30 min at 2 ml/min with high salt buffer: 20 mM HEPES pH 7.5, 750 mM NaCl, 5 mM $MgCl_2$, 5 mM $CaCl_2$, 0.5% lauryl maltose neopentyl glycol (LMNG, Anatrace), 0.02% cholesterol hemisuccinate (CHS, Anatrace) followed by low salt buffer: 20 mM HEPES pH 7.5, 100 mM NaCl, 5 mM $MgCl_2$, 5 mM $CaCl_2$, 0.5% LMNG, 0.02% CHS and an

agonist (5 µM Ipx, 1µM Ipx with 10 µM VU154, or 100 µM ACh). While the receptor was immobilised on anti-FLAG resin, the DNGα_{i1} cell pellet was thawed, dounced, and solubilised in the solubilisation buffer containing: 20 mM HEPES pH 7.5, 100 mM NaCl, 5 mM $MgCl_2$, 5 mM $CaCl_2$, 0.5% LMNG, 0.02% CHS, apyrase (5 units), and cOmplete Protease Inhibitor Cocktail. DNGα_{i1} was solubilized for 2 hrs at 4°C followed by the centrifugation at 30,000xg for 30 min to remove the insoluble material. Supernatant was filtered through a glass fibre filter (Millipore) and then added to the receptor bound to anti-Flag resin. Apyrase (5 units), scFv16, and agonist (either 1 µM Ipx, 1 µM Ipx with 10 µM VU154, or 100 µM ACh) were added and incubated for 1 hr at RT with gentle mixing. The anti-FLAG resin was then loaded onto a glass column and washed with approximately 20 CVs of washing buffer: 20 mM HEPES pH 7.4, 100 mM NaCl, 5 mM $MgCl_2$, 5 mM $CaCl_2$, 0.01% LMNG, 0.001% CHS, agonist (1 µM Ipx, 1 µM Ipx with 10 µM VU154, or 100 µM ACh). Complex was eluted with size-exclusion chromatography (SEC) buffer: 20 mM HEPES pH 7.5, 100 mM NaCl, 5 mM $MgCl_2$, 0.01% LMNG, 0.001% CHS and agonist (1 µM Ipx, or 1 µM Ipx with 10 µM VU154, or 100 µM ACh) with the addition of 10 mM EGTA and 0.1 mg/mL FLAG peptide. After the elution an additional 1-2 mg of scFv16 was added, and shortly incubated on ice before concentrating using a 100-kDa Amicon filter to a final volume of 500 µL. The sample was filtered using a 0.22 µm filter followed by SEC using a Superdex 200 increase 10/300 column (Cytivia) using SEC buffer. For the ACh- and VU154-Ipx-bound samples, the fractions containing protein were concentrated again and re-run over SEC using a buffer with half the amount of detergent in order to remove empty micelles. Samples were concentrated and flash frozen using liquid nitrogen. In case of the LY298-Ipx-bound sample, the sample was purified with 1 µM Ipx only. After SEC, the sample was then split in half, where one half was incubated with approximately 1.6 µM LY298 at 4°C overnight, and then concentrated and flash frozen in liquid nitrogen.

EM sample preparation and data acquisition

Samples (3 µL) were applied to glow-discharged Quantifoil R1.2/1.3 Cu/Rh 200 mesh grids (Quantifoil) (M4R-G_{i1}-Ipx and M4R-G_{i1}-Ipx-LY298) or UltrAuFoil R1.2/1.3 Au 300 mesh grids (Quantifoil) (M4R-G_{i1}-Ipx-VU154 and M4R-G_{i1}-Ach) and were vitrified on a Vitrobot Mark IV (Thermo Fisher Scientific) set to 4°C and 100 % humidity and 10 s blot time. Data were collected on a Titan Krios G3i 300 kV electron microscope (Themo Fisher Scientific) equipped with GIF Quantum energy filter and K3 detector (Gatan). Data acquisition was performed in

EFTEM NanoProbe mode with a 50 µM C2 aperture at an indicated magnification of ×105,000 with zero-loss slit width of 25 eV. The data were collected automatically with homemade scripts for SerialEM performing a 9-hole beam-image shift acquisition scheme with one exposure in the centre of each hole. Experimental parameters specific to each collected data set is listed in **Table S2**.

Image processing

Specific details for the processing of each cryo-EM data set are shown in **Figure S1**. Image frames for each movie were motion corrected using MotionCor2 (Zheng et al., 2017) and contrast transfer function (CTF)-estimated using GCTF (Zhang, 2016). Particles were picked from corrected micrographs using crYOLO (Wagner et al., 2019) or RELION-3.1 software (Zivanov et al., 2018) followed by reference-free 2D and 3D classifications. Particles within bad classes were removed and remaining particles subjected to further analysis. Resulting particles were subjected to Bayesian polishing, CTF refinement, 3D auto-refinement in RELION, followed by another round of 3D classification and 3D refinement that yielded the final maps (Zivanov et al., 2018). Local resolution was determined from RELION using half-reconstructions as input maps. Due to the high degree of conformational flexibility between the receptor and G protein, a further local refinement was performed in cryoSPARC for the ACh-bound M_4R-complex. A receptor focused map was generated (2.75 Å) which was used to generate a PDB model of the ACh-bound M_4R.

Model building and refinement

An initial M_4R template model was generated from our prior modelling studies of the M_4 mAChR that was based on an active state M_2 mAChR structure (PBD: 4MQT) (Kruse et al., 2013). An initial model for dominant negative $G\alpha_{i1}G\beta_1G\gamma_2$ was from a structure in complex with Smoothend (PDB: 6OT0) (Qi et al., 2019) and scFv16 from the X-ray crystal structure in complex with heterotrimeric G protein (PDB: 6CRK) (Maeda et al., 2018). Models were fit into EM maps using UCSF Chimera (Pettersen et al., 2004), and then rigid-body-fit using PHENIX (Liebschner et al., 2019), followed by iterative rounds of model rebuilding in Coot (Casañal et al., 2020) and ISOLDE (Croll, 2018), and real-space refinement in PHENIX. Restrains for all ligands were generated from the GRADE server, https://grade.globalphasing.org. Model validation was performed with Molprobity (Williams et al., 2018) and the wwPDB validation

server (Berman et al., 2003). Figures were generated using UCSF Chimera (Pettersen et al., 2004), Chimera X (Pettersen et al., 2021), and PyMOL (Schrödinger).

Cryo-EM 3D variability analysis

3D variability analysis (3DVAR) was performed to access and visualize the dynamics within the cryo-EM datasets of the M_4 mAChR complexes, as previously described using cryoSPARC (Punjani and Fleet, 2021). The polished particle stacks were imported into cryoSPARC, followed by 2D classification and 3D refinement using the respective low pass filtered RELION consensus maps as an initial model. 3DVA was analysed in three components with 20 volume frames of data per component of motion. Output files were visualized using UCSF Chimera (Pettersen et al., 2004).

Gaussian accelerated molecular dynamics (GaMD). GaMD enhances the conformational sampling of biomolecules by adding a harmonic boost potential to reduce the system energy barriers (Miao et al., 2015). When the system potential $V(\vec{r})$ is lower than a reference energy E, the modified potential $V^*(\vec{r})$ of the system is calculated as:

$$V^*(\vec{r}) = V(\vec{r}) + \Delta V(\vec{r})$$

$$\Delta V(\vec{r}) = \begin{cases} \frac{1}{2}k\left(E - V(\vec{r})\right)^2, & V(\vec{r}) < E \\ 0, & V(\vec{r}) \geq E, \end{cases} \quad (1)$$

Where k is the harmonic force constant. The two adjustable parameters E and k are automatically determined on three enhanced sampling principles. First, for any two arbitrary potential values $v_1(\vec{r})$ and $v_2(\vec{r})$ found on the original energy surface, if $V_1(\vec{r}) < V_2(\vec{r})$, ΔV should be a monotonic function that does not change the relative order of the biased potential values; i.e., $V_1^*(\vec{r}) < V_2^*(\vec{r})$. Second, if $V_1(\vec{r}) < V_2(\vec{r})$, the potential difference observed on the smoothened energy surface should be smaller than that of the original; i.e., $V_2^*(\vec{r}) - V_1^*(\vec{r}) < V_2(\vec{r}) - V_1(\vec{r})$. By combining the first two criteria and plugging in the formula of $V^*(\vec{r})$ and ΔV, we obtain

$$V_{max} \leq E \leq V_{min} + \frac{1}{k}, \quad (2)$$

Where V_{min} and V_{max} are the system minimum and maximum potential energies. To ensure that Eq. 2 is valid, k has to satisfy: $k \leq 1/(V_{max} - V_{min})$. Let us define: $k = k_0 \cdot 1/(V_{max} - V_{min})$, then $0 < k_0 \leq 1$. Third, the standard deviation (SD) of ΔV needs to be

small enough (i.e. narrow distribution) to ensure accurate reweighting using cumulant expansion to the second order: $\sigma_{\Delta V} = k(E - V_{avg})\sigma_V \leq \sigma_0$, where V_{avg} and σ_V are the average and SD of $\Delta V$with σ_0 as a user-specified upper limit (e.g., $10k_BT$) for accurate reweighting. When E is set to the lower bound $E = V_{max}$ according to Eq. 2, k_0 can be calculated as

$$k_0 = \min(1.0, k_0') = min\left(1.0, \frac{\sigma_0}{\sigma_V} \cdot \frac{V_{max} - V_{min}}{V_{max} - V_{avg}}\right), \quad \textbf{(3)}$$

Alternatively, when the threshold energy E is set to its upper bound $E = V_{min} + 1/k$, $k_0$is set to:

$$k_0 = k_0'' \equiv \left(1 - \frac{\sigma_0}{\sigma_V}\right) \cdot \frac{V_{max} - V_{min}}{V_{avg} - V_{min}}, \quad \textbf{(4)}$$

If $k_0''$is calculated between 0 and 1. Otherwise, $k_0$is calculated using Eq. 3.

Energetic Reweighting of GaMD Simulations. For energetic reweighting of GaMD simulations to calculate potential of mean force (PMF), the probability distribution along a reaction coordinate is written as $p^*(A)$. Given the boost potential $\Delta V(r)$ of each frame, $p^*(A)$ can be reweighted to recover the canonical ensemble distribution $p(A)$, as:

$$p(A_j) = p^*(A_j) \frac{\langle e^{\beta \Delta V(r)} \rangle_j}{\sum_{i=1}^{M} \langle p^*(A_i) e^{\beta \Delta V(r)} \rangle_i}, \; j = 1, \ldots, M, \quad \textbf{(5)}$$

where *M* is the number of bins, $\beta = k_BT$ and $\langle e^{\beta \Delta V(r)} \rangle_j$ is the ensemble-averaged Boltzmann factor of $\Delta V(r)$ for simulation frames found in the j^{th} bin. The ensemble-averaged reweighting factor can be approximated using cumulant expansion:

$$\langle e^{\beta \Delta V(r)} \rangle = exp\left\{\sum_{k=1}^{\infty} \frac{\beta^k}{k!} C_k\right\}, \quad \textbf{(6)}$$

where the first two cumulants are given by:

$$\begin{aligned} C_1 &= \langle \Delta V \rangle, \\ C_2 &= \langle \Delta V^2 \rangle - \langle \Delta V \rangle^2 = \sigma_v^2. \end{aligned} \quad \textbf{(7)}$$

The boost potential obtained from GaMD simulations usually follows near-Gaussian distribution (Miao and McCammon, 2017). Cumulant expansion to the second order thus provides a good approximation for computing the reweighting factor (Miao et al., 2014, 2015). The reweighted free energy $F(A) = -k_BT \ln p(A)$ is calculated as:

$$F(A) = F^*(A) - \sum_{k=1}^{2} \frac{\beta^k}{k!} C_k + F_c, \quad \textbf{(8)}$$

where $F^*(A) = -k_B T \ln p^*(A)$ is the modified free energy obtained from GaMD simulation and F_c is a constant.

System Setup. The M_4R-ACh-G_{i1}, M_4R-Ipx-G_{i1}, M_4R-Ipx-G_{i1}-VU154 and M_4R-Ipx-G_{i1}-LY298 cryo-EM structures were used for setting up simulation systems. The scFv16 in the cryo-EM structures was omitted in all simulations. The initial structures of single mutant D432E and T433R mutant of M_4R-Ipx-G_{i1}-VU154 were obtained by mutating the corresponding residues in the M_4R-Ipx-G_{i1}-VU154 cryo-EM structure. The initial structures of M_4R-ACh-G_{i1}-VU154 and M_4R-ACh-G_{i1}-LY298 were obtained from M_4R-Ipx-G_{i1}-VU154 and M_4R-Ipx-G_{i1}-LY298 cryo-EM structures by replacing Ipx with ACh through alignment of receptors to the M4R-ACh-G_{i1} cryo-EM structure. The initial structures of M_4R-G_{i1}-VU154 and M_4R-G_{i1}-LY298 were obtained by removing the corresponding Ipx agonist from the M_4R-Ipx-G_{i1}-VU154 and M_4R-Ipx-G_{i1}-LY298 cryo-EM structures. The initial structures of M_4R-VU154 and M_4R-LY298 were obtained by removing the corresponding Ipx agonist and G_{i1} protein from the M_4R-Ipx-G_{i1}-VU154 and M_4R-Ipx-G_{i1}-LY298 cryo-EM structures. According to previous findings, intracellular loop (ICL) 3 is highly flexible and removal of ICL3 does not appear to affect GPCR function (Dror et al., 2011, 2015). The ICL3 was thus omitted as in the current GaMD simulations. Similar as previous study, helical domains of the G_{i1} protein missing in the cryo-EM structures were not included in the simulation models. This was based on earlier simulation of the β_2AR-G_s complex, which showed that the helical domain fluctuated substantially (Dror et al., 2015). All chain termini were capped with neutral groups (acetyl and methylamide). All the disulphide bonds in the complexes (i.e., Cys108$^{3.25}$-Cys185^{45x50} and Cys426^{ECL3}-Cys429^{ECL3} in the M4R) that were resolved in the cryo-EM structures were maintained in the simulations. Using the *psfgen* plugin in VMD (Humphrey et al., 1996), missing atoms in protein residues were added and all protein residues were set to the standard CHARMM protonation states at neutral pH. For each of the complex systems, the receptor was inserted into a palmitoyl-oleoyl-phosphatidyl-choline (POPC) bilayer with all overlapping lipid molecules removed using the membrane plugin in VMD. The system charges were then neutralized at 0.15M NaCl using the *solvate* plugin in VMD (Humphrey et al., 1996). The simulation systems were summarized in **Table S3**.

Simulation Protocol. The CHARMM36M parameter set (Huang et al., 2017; Klauda et al., 2010; Vanommeslaeghe and MacKerell, 2015) was used for the M_4 mAChRs, G_{i1} proteins, and

POPC lipids. Force field parameters of agonists ACh and Ipx, PAMs LY298 and VU154 were obtained from the CHARMM ParamChem web server (Vanommeslaeghe and MacKerell, 2012; Vanommeslaeghe et al., 2012). Force field parameters with high penalty were optimized with FFParm (Kumar et al., 2020). GaMD simulations of these systems followed a similar protocol used in previous studies of GPCRs (Draper-Joyce et al., 2021; Miao and McCammon, 2016, 2018). For each of the complex systems, initial energy minimization, thermalization, and 20ns cMD equilibration were performed using NAMD2.12 (Phillips et al., 2005). A cutoff distance of 12 Å was used for the van der Waals and short-range electrostatic interactions and the long-range electrostatic interactions were computed with the particle-mesh Ewald summation method (Darden et al., 1993). A 2-fs integration time step was used for all MD simulations and a multiple-time-stepping algorithm was used with bonded and short-range non-bonded interactions computed every time step and long-range electrostatic interactions every two-time steps. The SHAKE algorithm (Ryckaert et al., 1977) was applied to all hydrogen-containing bonds. The NAMD simulation started with equilibration of the lipid tails. With all other atoms fixed, the lipid tails were energy minimized for 1,000 steps using the conjugate gradient algorithm and melted with a constant number, volume, and temperature (NVT) run for 0.5 ns at 310 K. The twelve systems were further equilibrated using a constant number, pressure, and temperature (NPT) run at 1 atm and 310 K for 10 ns with 5 kcal/(mol· $Å^2$) harmonic position restraints applied to the protein and ligand atoms. Final equilibration of each system was performed using a NPT run at 1 atm pressure and 310 K for 0.5 ns with all atoms unrestrained. After energy minimization and system equilibration, conventional MD simulations were performed on each system for 20 ns at 1 atm pressure and 310 K with a constant ratio constraint applied on the lipid bilayer in the X-Y plane.

With the NAMD output structure, along with the system topology and CHARMM36M force field files, the *ParmEd* tool in the AMBER package was used to convert the simulation files into the AMBER format. The GaMD module implemented in the GPU version of AMBER20 (Case et al. 2020) was then applied to perform the GaMD simulation. GaMD simulations of systems with G_{i1} protein (M_4R-ACh-G_{i1}, M_4R-Ipx-G_{i1}, M_4R-Ipx-G_{i1}-VU154, M_4R-Ipx-G_{i1}-LY298, M_4R-ACh-G_{i1}-VU154, M_4R-ACh-G_{i1}-LY298, single mutant D432E and T433R mutants of M_4R-Ipx-G_{i1}-VU154) included a 8-ns short cMD simulation used to collect the potential statistics for calculating GaMD acceleration parameters, a 48-ns equilibration after adding the boost

potential, and finally three independent 500-ns GaMD production simulations with randomized initial atomic velocities. The average and SD of the system potential energies were calculated every 800,000 steps (1.6 ns). GaMD simulations of M_4R-VU154 and M_4R-LY298 included a 2.4-ns short cMD simulation used to collect the potential statistics for calculating GaMD acceleration parameters, a 48-ns equilibration after adding the boost potential, and finally three independent 1000-ns GaMD production simulations with randomized initial atomic velocities. The average and SD of the system potential energies were calculated every 240,000 steps (0.48 ns). All GaMD simulations were run at the "dual-boost" level by setting the reference energy to the lower bound. One boost potential is applied to the dihedral energetic term and the other to the total potential energetic term. The upper limit of the boost potential SD, σ_0 was set to 6.0 kcal/mol for both the dihedral and the total potential energetic terms. Similar temperature and pressure parameters were used as in the NAMD simulations.

Simulation Analysis. CPPTRAJ (Roe and Cheatham, 2013) and VMD (Humphrey et al., 1996) were used to analyze the GaMD simulations. The root-mean square deviations (RMSDs) of the agonist ACh and Ipx, PAM VU154 and LY298 relative to the simulation starting structures, the interactions between receptor and agonists/PAMs, distances between the receptor TM3 and TM6 intracellular ends were selected as reaction coordinates. Particularly, distances were calculated between the Cα atoms of residues Arg$^{3.50}$ and Thr$^{6.30}$, N atom of residue N117$^{3.37}$ and carbon atom (C5) in the acetyl group of ACh or oxygen atom (O09) in the ether bond of Ipx, NE1 atom of residue W164$^{4.67}$ and carbon atom (C5) in the acetyl group of ACh or oxygen atom (O09) in the ether bond of Ipx, indole ring of residue W413$^{6.48}$ and acetyl group of ACh or heterocyclic isoazoline group of Ipx, OH atom of residue Y89$^{2.61}$ and oxygen atom in the amide group of VU154/LY298, benzene ring of residue F186$^{45.51}$ and aromatic core of the PAMs VU154/LY298, OH atom of residue Y439$^{7.39}$ and nitrogen atoms in the amine group of the PAMs VU154/LY298, CD atom of residue Q184$^{45.49}$ and nitrogen atom in the amide group of VU154/LY298, CG atom of residue N423$^{6.58}$ and chlorine atom in PAM LY298, OH atom of residue Y92$^{2.64}$ and nitrogen atom in the amide group of VU154, OG1 atom of residue T433$^{7.33}$ and sulfur atom in the trifluoromethylsulfonyl group of VU154. In addition, the χ2 angle of residue W413$^{6.48}$ and W435$^{7.35}$ were calculated. Time courses of these reaction coordinates obtained from the GaMD simulation were plotted in **Figures 4,5,6,7, S4, and S7**. The

PyReweighting (Miao et al., 2014) toolkit was applied to reweight GaMD simulations to recover the original free energy or potential of mean force (PMF) profiles of the simulation systems. PMF profiles were computed using the combined trajectories from all the three independent 500 ns GaMD simulations for each system. A bin size of 1.0 Å was used for RMSD. The cutoff was set to 500 frames for 2D PMF calculations. The 2D PMF profiles were obtained for wildtype M_4R-Ipx-G_{i1}-LY298, M_4R-Ipx-G_{i1}-VU154, and the D432E and T433R single mutants of the M_4R-Ipx-G_{i1}-VU154 system regarding the RMSDs of the agonist Ipx and the RMSDs of the PAMs relative to the cryo-EM conformation (**Fig S7**).

Data analysis

All pharmacological data was fit using GraphPad Prism 9.2.0. Saturation binding experiments to determine B_{max} and pK_d values were determined as previously described (Leach et al., 2011; Nawaratne et al., 2010; Thal et al., 2016). Detailed equations and analysis details can be found in **Appendix 1**. Interaction inhibition binding curves between [^{3}H]-NMS, agonists (ACh or Ipx), and PAMs (LY298 or VU154) were analysed using the allosteric ternary complex model to calculate binding affinity values for each ligand (pK_A – for ACh/Ipx and pK_B for LY298/VU154) and the degree of binding modulation between agonist and PAM (log α) (Christopoulos and Kenakin, 2002). The pK_B values for LY298 and VU154 were determined from global fits of the ACh and Ipx curves to generate one pK_B value per ligand (Ehlert, 1988; Leach et al., 2011; Nawaratne et al., 2010; Thal et al., 2016). All pERK1/2 and TruPath assays were analyzed using the operational model allosterism and agonism to determine values of orthosteric (τ_A) or allosteric efficacy (τ_B) and the functional modulation (log $\alpha\beta$) between the agonists and PAMs (Leach et al., 2011; Nawaratne et al., 2010). Binding affinities of the agonists and the PAMs were fixed to values determined from equilibrium binding assays. The τ_B values for LY298 and VU154 were determined from global fits of the ACh and Ipx curves (when possible) to generate one value per ligand. For comparison between WT human M_4 mAChR and other M_4 mAChR constructs the log τ values were corrected (denoted log τ_C) by normalizing to B_{max} values from saturation binding experiments (Leach et al., 2011; Nawaratne et al., 2010; Thal et al., 2016). All affinity, potency, and cooperativity values were estimated as logarithms, and statistical analysis between WT and mutant M_4 mAChR were determined by one-way ANOVA using a Dunnett's post-hoc test with a value of $P < 0.05$ considered as significant in this study.

1548

1549

Supplemental Figures

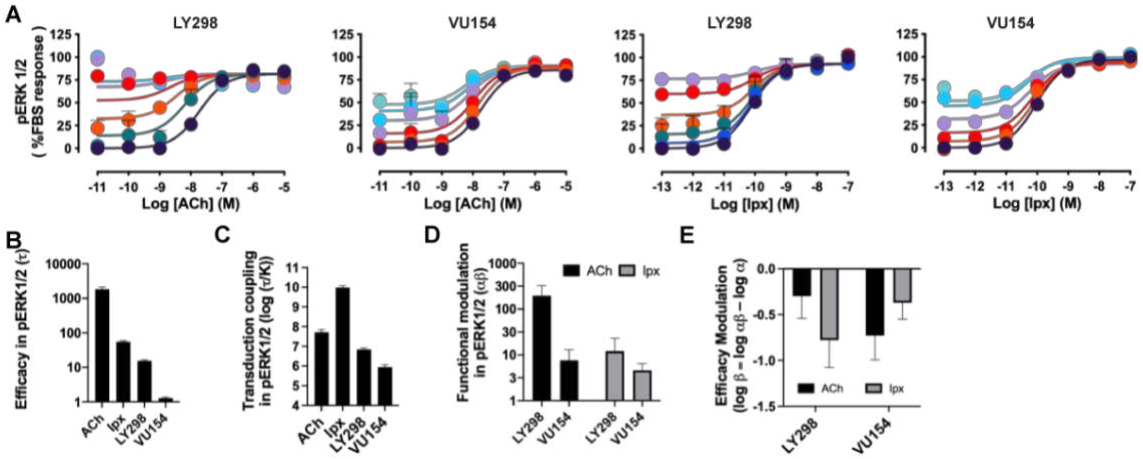

Figure S1. Pharmacological characterization of the PAMs, LY298 and VU154, with ACh and Ipx in pERK1/2 signaling assays, Related to Figure 2. (**A**) Concentration response curves of interactions between the orthosteric and allosteric ligands at the human M_4 mAChR in the pERK1/2 signaling assay.(**B-E**) Quantification of data from (**A**) and (**Figure 2A**) to calculate (**B**) the signaling efficacy (τ_A and τ_B) and (**C**) the transduction coupling coefficients (log (τ/K)) of each ligand, (**D**) the functional cooperativity ($\alpha\beta$) between ligands, and (**E**) the efficacy modulation (β) between ligands. All data are mean ± SEM of 3 or more independent experiments performed in duplicate or triplicate with the pharmacological parameters determined from a global fit of the data. The error in (**E**) was propagated using the square root of the sum of the squares. See **Table S1**.

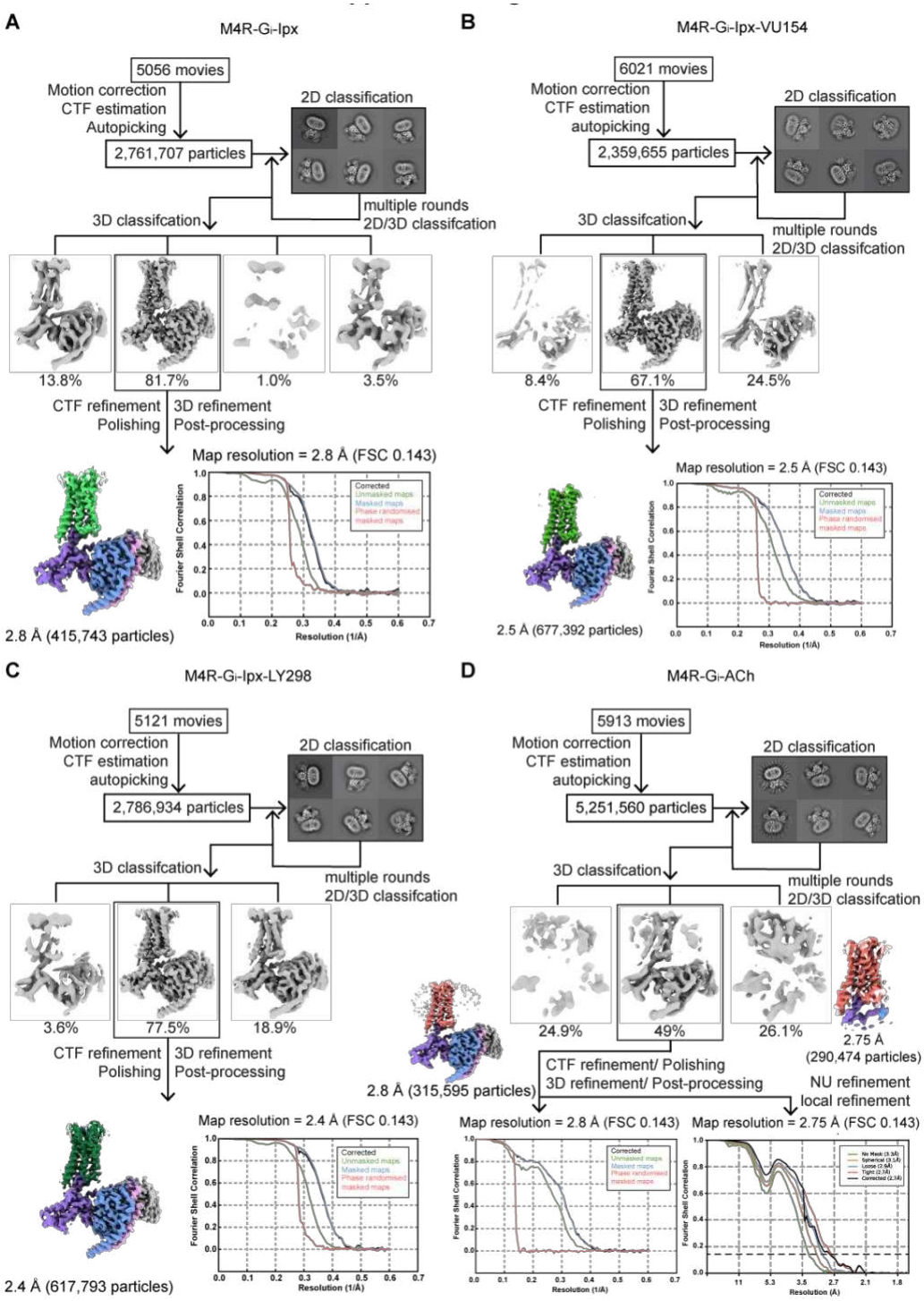

Figure S2. Cryo-EM data processing and analysis, Related to Figure 3. (**A-D**) Flow chart of cryo-EM data processing of the (**A**) Ipx-, (**B**) VU154-Ipx-, (**C**) LY298-Ipx-, and (**D**) ACh-bound M_4 mAChR complexes with G_{i1}-scFv16 including particle selections, 2D and 3D classifications, EM density map, and the Fourier shell correlation (FSC) curves.

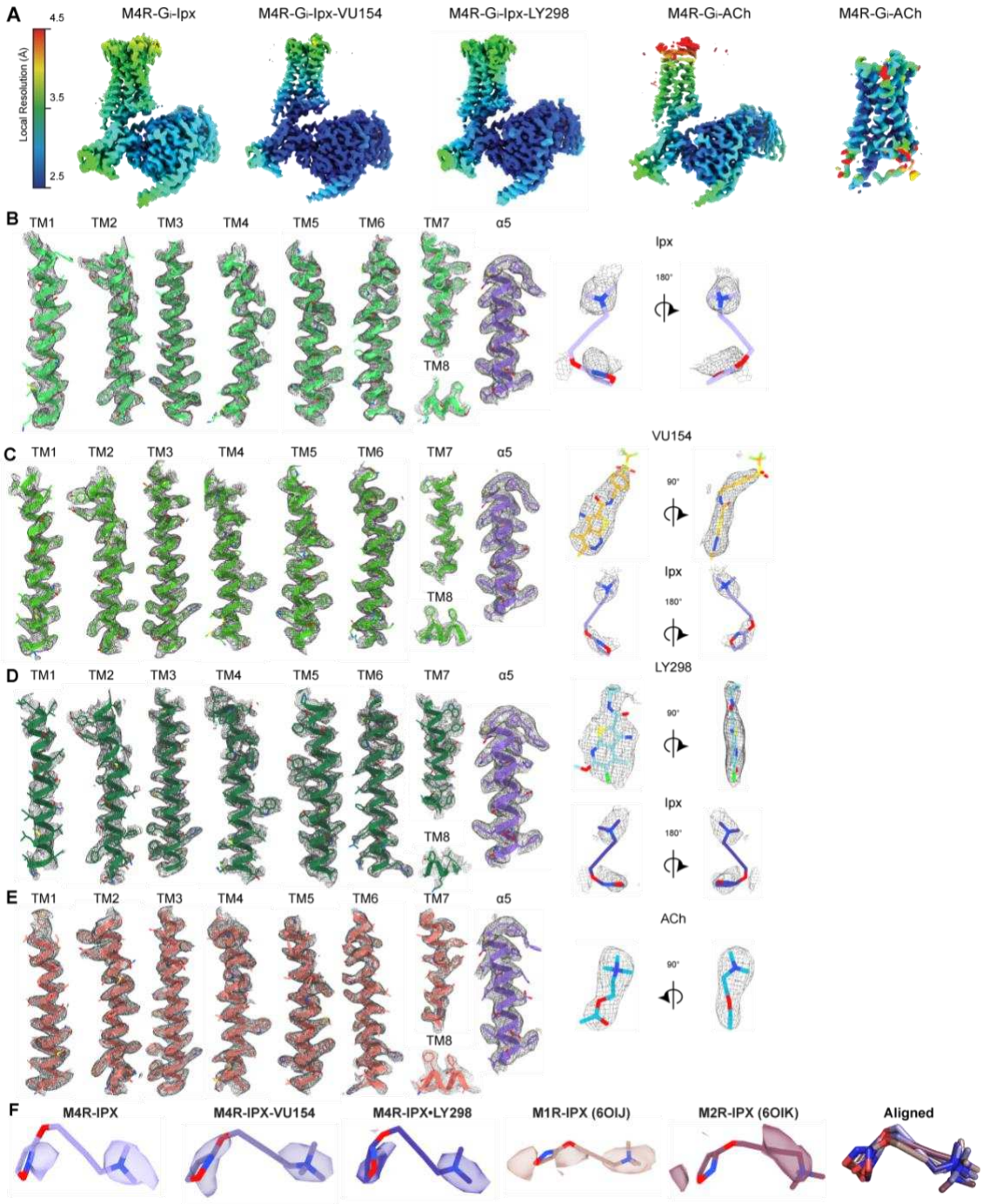

Figure S3. Cryo-EM density maps, Related to Figures 3–4. (**A**) EM maps coloured by local resolution. (**B-E**) Representative EM density and modelling for the 7 transmembrane (TM) helices, the C-terminus of $G\alpha_{i1}$, and ligands for the (**B**) Ipx-, (**C**) VU154-Ipx-, (**D**) LY298-Ipx-, and (**E**) ACh-bound M_4 mAChR complexes. (**F**) Comparison of the EM-density of Ipx from other mAChR structures with included Protein Data Bank (PDB) accession codes.

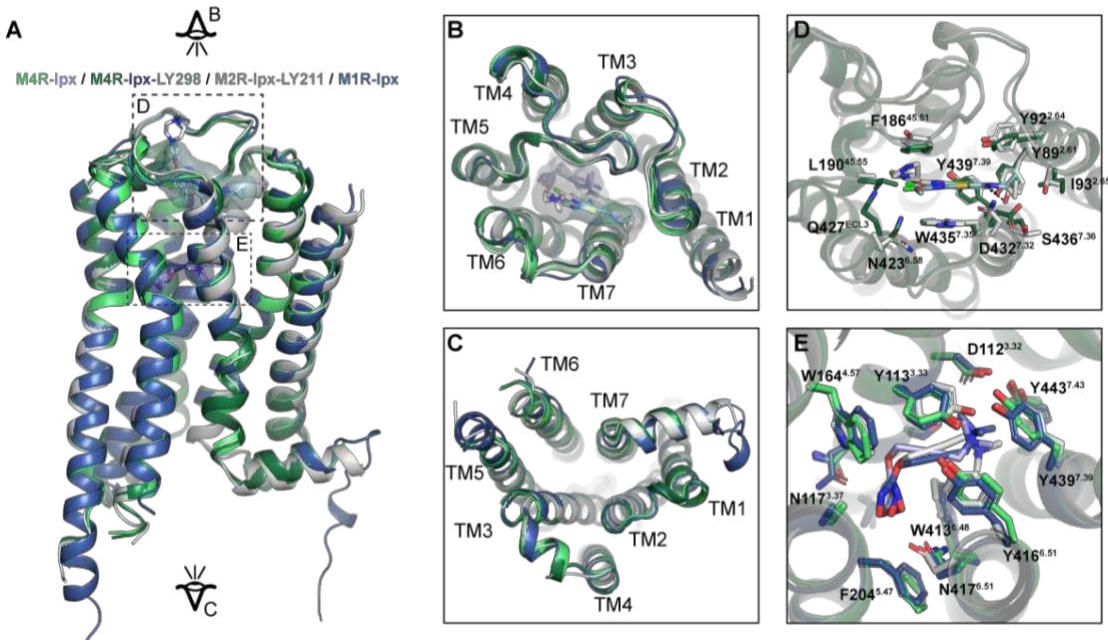

Figure S4. Comparison of active state mAChR structures. (**A**) Comparison of the Ipx- and LY298-Ipx-bound M_4 mAChR structures to the prior structures of Ipx-bound M_1 mAChR and LY2119620-Ipx-bound M_2 mAChR cryo-EM structures. Protein Data Bank (PDB) accession codes for the M_1 mAChR (PDB: 6OIJ) and the M_2 mAChR (PDB: 6OIK). (**B,C**) Views from the (**B**) extracellular and (**C**) intracellular surfaces. (**D**) Comparison of the binding pose of LY2119620 at the M_2 mAChR and LY2033298 at the M_4 mAChR. (**E**) Comparison of the Ipx binding site residues.

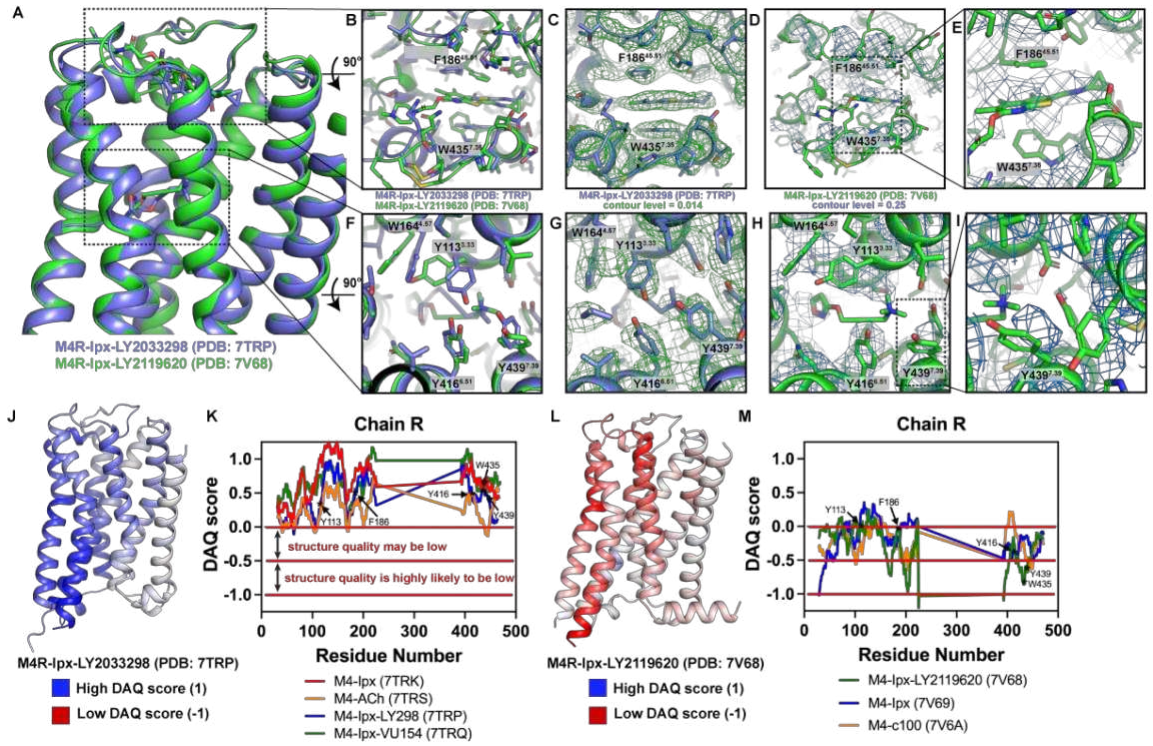

Figure S5. Comparison of active state M_4 mAChR structures. (**A**) Comparison of LY298-Ipx bound M_4 mAChR structure (PDB: 7TRP, coloured blue) to the LY2119620-Ipx bound M_4 mAChR structure (PDB: 7V68, coloured green) (Wang et al., 2022). (**B-E**) View of the allosteric binding site from the top of the receptor. (**B**) Comparison of key allosteric residues $F186^{45.51}$ and $W435^{7.35}$ showing different positions of the residues between M_4 mAChR structures. (**C**) Overlay of the EM map (EMD-26100, coloured green) onto the LY298-Ipx bound M_4 mAChR structure contoured at 0.014 in Pymol. (**D-E**) Overlay of the EM map (EMD-31738, coloured blue) onto the LY2119620-Ipx bound M_4 mAChR structure contoured at 0.25 in Pymol with a close-up of the allosteric residues in (**E**) showing a lack of clear density and mismodelled residues. (**F-I**) View of the orthosteric binding site from the top of the receptor. (**F**) Comparison of key orthosteric binding site residues. (**G**) Related to (**C**) with view from orthosteric site. (**H-I**) Related to (**D**) with view from orthosteric site with a close-up (**I**) of orthosteric residues that are mismodelled or lacking clear density. (**J-M**) DAQ-score provides an estimation of the local quality of protein models from cryo-EM maps on a per residue basis. DAQ-scores were determined from the DAQ web server using the recommended default settings (Terashi et al., 2022).(**J,L**) DAQ scores from the analysis of (J) the LY298-Ipx-M_4R-G_{i1} complex and (L) the LY2119620-Ipx-M_4R-G_{i1} complex mapped onto the cartoon of the receptor chain and colour coded by score. A DAQ-score that is positive (coloured blue at

values of 1) indicates a correct assignment. A DAQ-score near 0 (colored white) indicates a position in the map that lacks a distinct density pattern for the assigned amino acid. DAQ-scores less than 0 (colored red at -1) indicate a position that could be misassigned or poorly fit. (**K**) DAQ scores for all four M_4 mAChR structures reported in this manuscript with DAQ scores of each Cα atom plotted for each residue. Key orthosteric and allosteric residues are denoted by asterisks. Nearly every residue has a value above 0. (**M**) Similar to K, but for all three M_4 mAChR structures reported in (Wang et al., 2022). Very few residues have a score above 0, indicating potential issues with the model and maps.

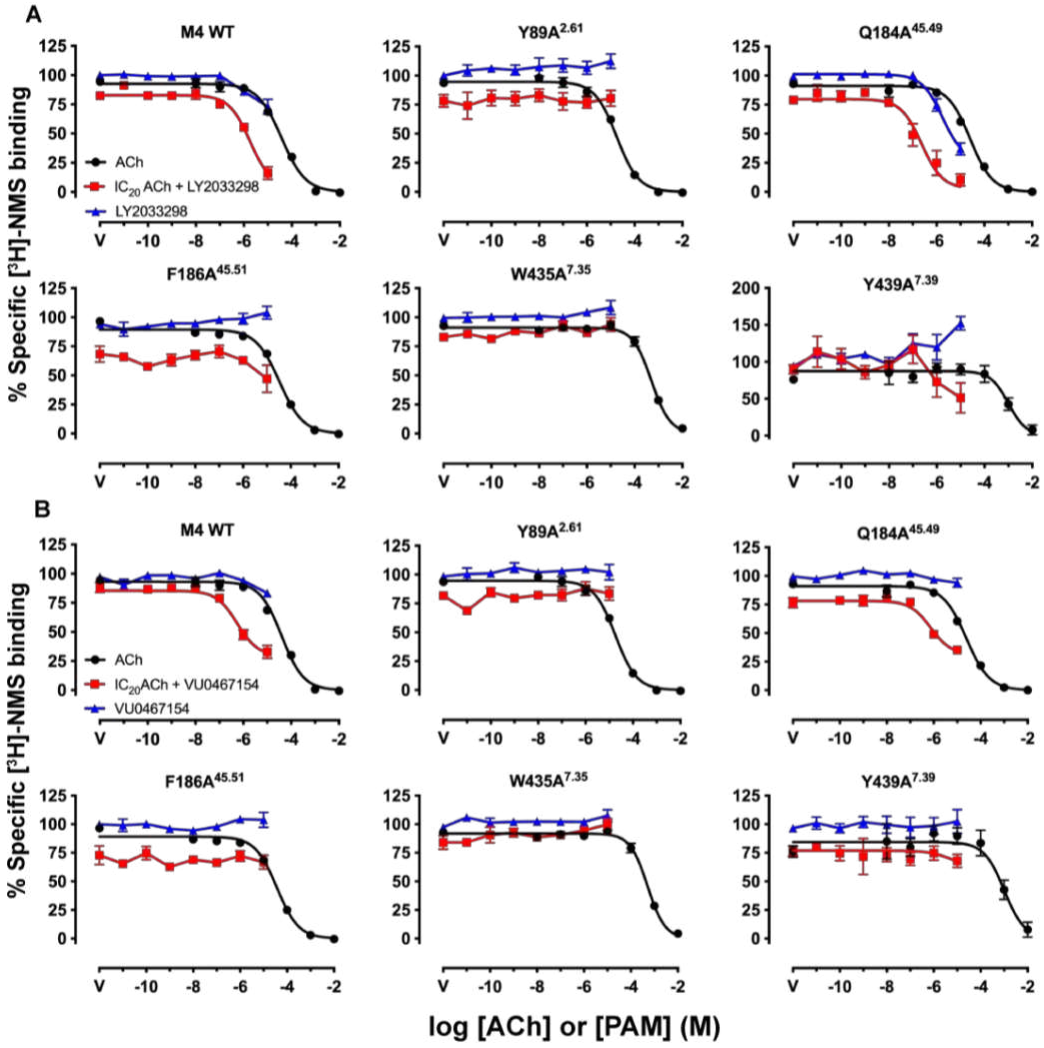

Figure S6. Key residues for the binding of LY298 and VU154 at the human M4 mAChR, Related to Figure 4. (**A,B**) Competition binding with a fixed concentration of [^{3}H]-NMS and increasing concentrations of ACh (black circles), (**A**) LY298 or (**B**) VU154 (blue circles), and LY298 or VU154 in the presence of an IC_{20} concentration of ACh (red squares). Curves drawn through the points represent a global fit of an extended ternary complex model. Data points represent the mean ± SEM of 3 or more independent experiments performed in duplicate. Similar data were observed for competition binding with Ipx instead of ACh. See **Table S4**.

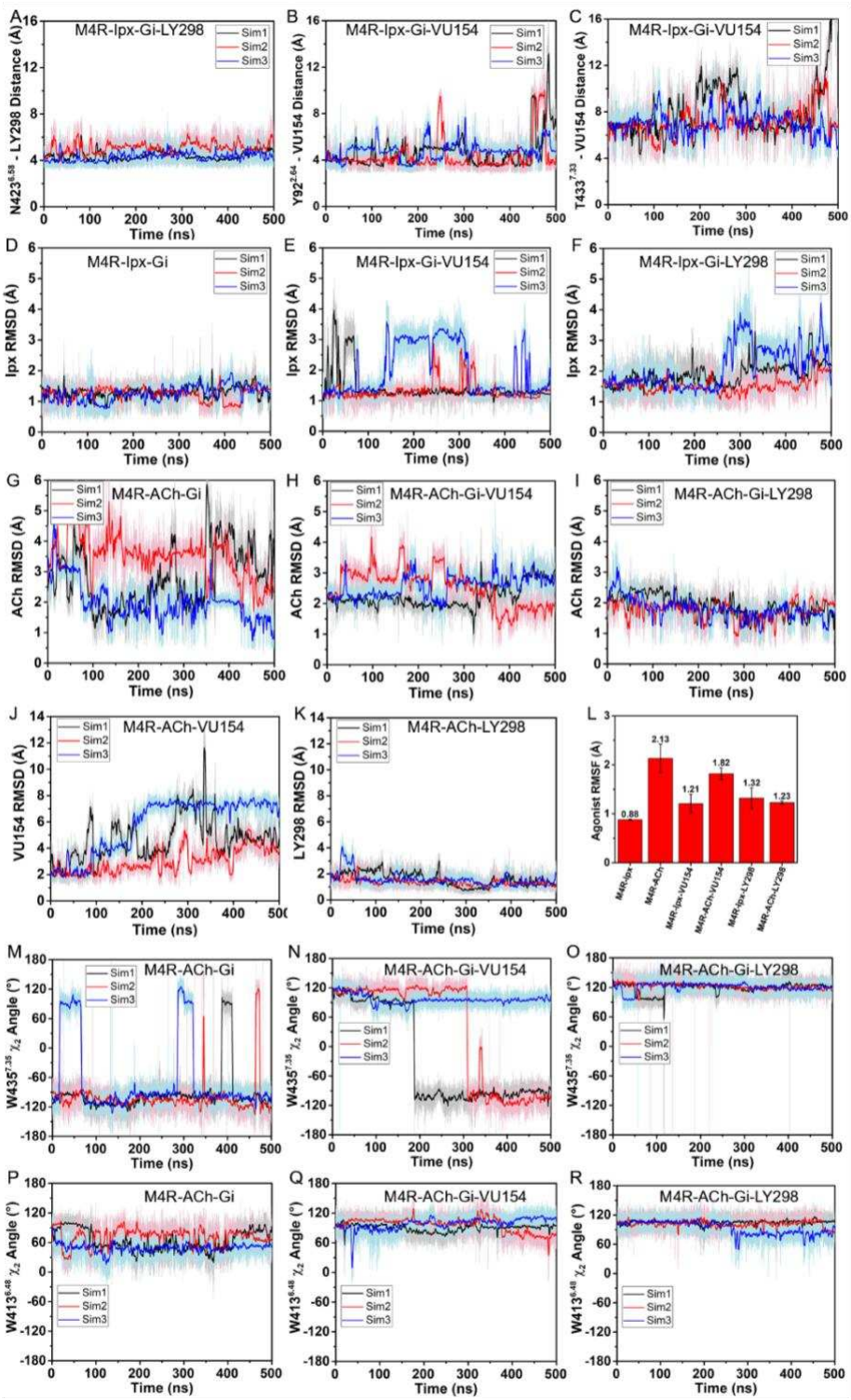

Figure S7. GaMD Simulations, Related to Figures 4–6 (**A-R**) Time courses from GaMD simulations, each performed with 3 separate replicates. Individual replicate simulations are illustrated with different colours. The heading of each plot refers to the specific model used in the simulations. See **Table S2**. (**A**) Distance between $N423^{6.58}$ and the fluorine atom of LY298 from GAMD simulations of the LY298-Ipx-M4R-G_{i1} structure. (**B,C**) Distance between

(**B**) $Y92^{2.64}$ and (**C**) $T433^{7.33}$ to VU154 from GAMD simulations of the VU154-Ipx-M4R-G_{i1} structure. (**D-F**) RMSDs of Ipx from simulations of the cryo-EM structures. (**G-I**) RMSDs of ACh from simulations of the (**G**) cryo-EM structure or (**H,I**) PAM docked models. (**J,K**) RMSDs of VU154 and LY298 from the ACh-bound M4 mAChR simulations. (**L**) Bar graph of the root mean fluctuations of the agonists Ipx or ACh across the GaMD simulations of the M_4-G_{i1} complexes with or without the PAMs. Values shown are mean ± SEM, n=3. (**M-R**) Time course of the ACh-bound M_4-G_{i1} simulations illustrating variances in the (**M-O**) $W435^{7.35}$ χ_2 angle and (**P-R**) the $W413^{6.48}$ χ_2 angle.

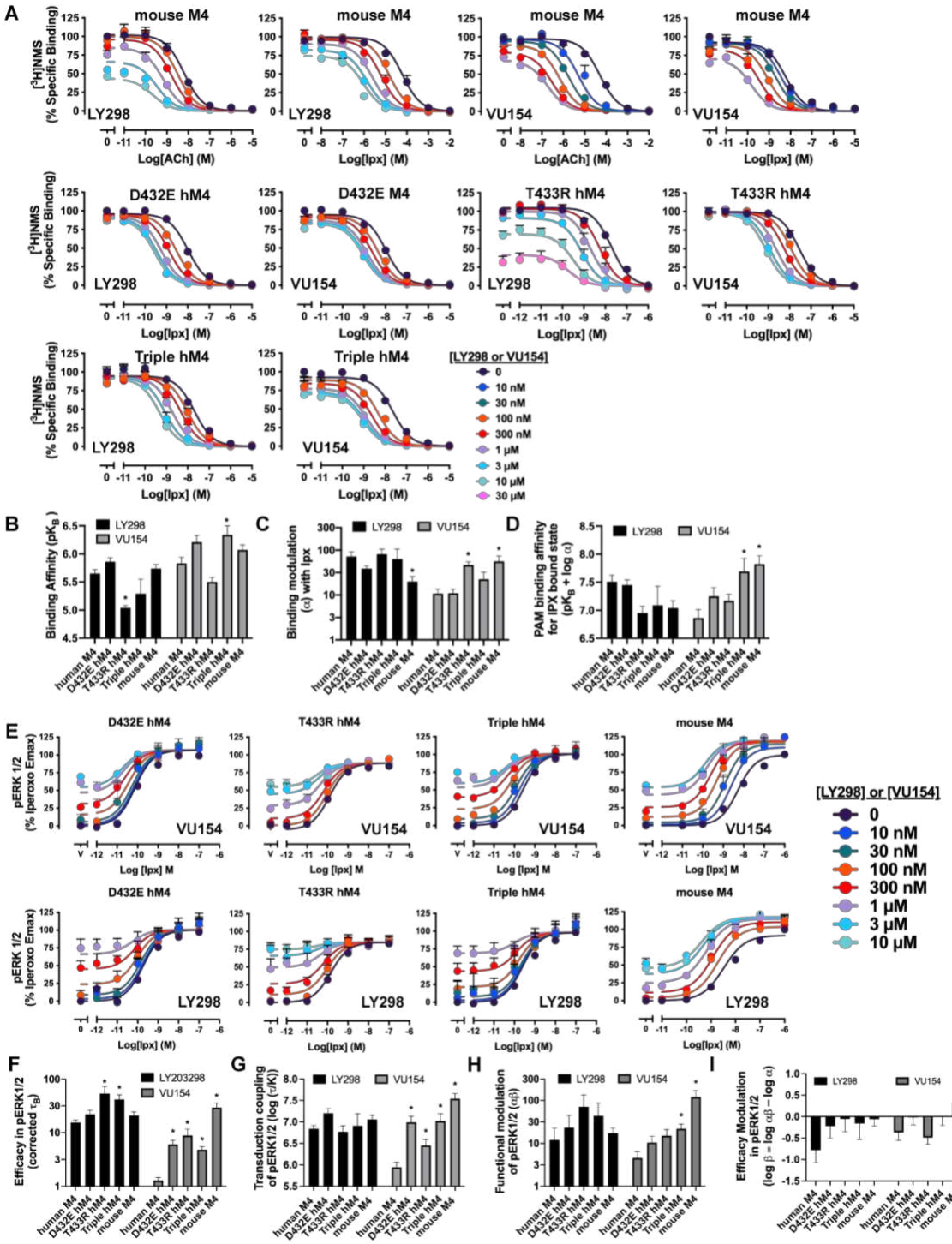

Figure S8. Concentration response curves, Related to Figure 7. (**A**) Concentration response curves the orthosteric and allosteric ligands in [^{3}H]-NMS binding assays at the mouse M_4 mAChR, D432E, T433R, and the V91L, D432E, T433R triple mutant of the human M_4 mAChR. (**B-D**) Quantification of data from (**A**) to calculate (**B**) equilibrium binding affinities (pK_B) of the PAMs, (**C**) the degree of binding modulation (α) between Ipx and PAMs, and the modified affinities (**D**) αK_B. See **Table S4**. (**E**) Concentration response curves of an interaction between

ACh and LY298 in pERK1/2 at the mouse M_4 mAChR, D432E, T433R, and the V91L, D432E, T433R triple mutant of the human M_4 mAChR. (**F-I**) Quantification of data from (**A,E**) to calculate (**F**) the signaling efficacy (τ_A and τ_B) and (**G**) the transduction coupling coefficients (log (τ/K)) of each ligand, (**H**) the functional cooperativity ($\alpha\beta$) between ligands, and (**I**) the efficacy modulation (β) between ligands. All data are mean ± SEM of 3 or more independent experiments performed in duplicate or triplicate with the pharmacological parameters determined from a global fit of the data. The error in (**D,I**) was propagated using the square root of the sum of the squares. *Indicates statistical significance ($p < 0.05$) relative to WT as determined by a one-way ANOVA with a Dunnett's post-hoc test. See **Table S1**.

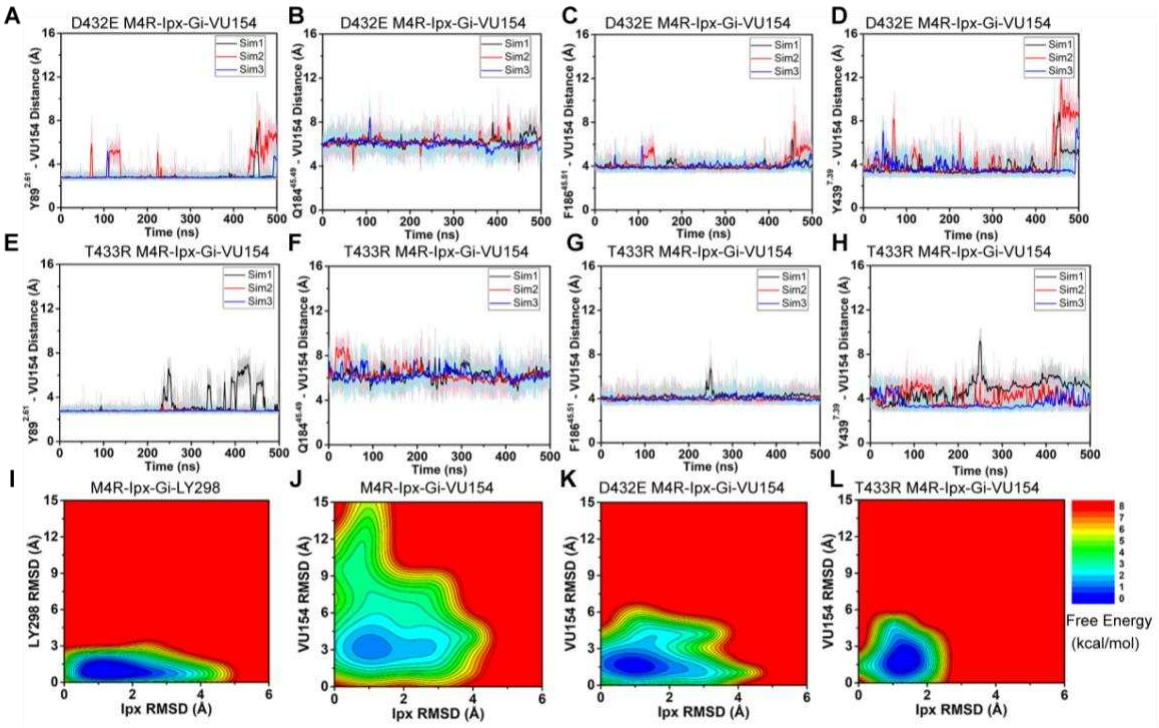

1656

1657 **Figure S9. GaMD Simulations of D432E and T433R human M4 mAChR mutants, Related to**

1658 **Figure 7.** (**A-H**) Time courses obtained from GaMD simulations of the (**E-H**) D432E and (**I-L**)

1659 T433R mutant M_4R-Ipx-G_{i1}-VU154 systems with (**A,E**) $Y89^{2.61}$ – VU154 distance, (**B,F**) $Q184^{45.49}$

1660 – VU154 distance, (**C,G**) $F186^{45.51}$ – VU154 distance, and (**D,H**) $Y439^{7.39}$ – VU154 distance.

1661 (**I-L**) 2D free energy profile of the RMSDs of LY298 and VU154 with Ipx. See **Table S3**.

1662

Table S1. Pharmacological parameters from radioligand binding and functional experiments.

[^{3}H]-NMS saturation binding on stable M_4 mAChR CHO cells						
Constructs		Sites per cell[a]		pK_D[b]		
Human WT M_4 mAChR		598,111 ± 43,067 (7)		9.76 ± 0.05 (7)		
Mouse WT M_4 mAChR		21,027 ± 2,188 (3)		9.76 ± 0.05 (3)		
Human D432E M_4 mAChR		126,377 ± 10,066 (3)		9.60 ± 0.07 (3)		
Human T433R M_4 mAChR		157,442 ± 36,658 (6)		9.64 ± 0.09 (6)		
Human V91L, D432E, T433R M_4 mAChR		205,771 ± 20,975 (4)		9.58 ± 0.08 (4)		
[^{3}H]-NMS interaction binding assays between ACh or Ipx and LY298 or VU154 on stable M_4 mAChR constructs in Flp-In CHO cells						
Constructs	PAM	pK_i ACh[c]	pK_i Ipx[c]	pK_B PAM[c]	log α_{ACh}[d]	log α_{Ipx}[d]
Human WT M_4 mAChR	LY298	4.50 ± 0.06 (4)	8.30 ± 0.06 (4)	5.65 ± 0.07 (8)[e]	2.59 ± 0.10 (4)	1.86 ± 0.10 (4)
	VU154	4.40 ± 0.09 (4)	8.19 ± 0.06 (8)	5.83 ± 0.11 (12)[e]	1.61 ± 0.13 (4)	1.03 ± 0.10 (8)
Mouse WT M_4 mAChR	LY298	4.52 ± 0.07 (4)	8.55 ± 0.06 (4)	5.74 ± 0.07 (8)[e]	1.78 ± 0.10 (4)	1.30 ± 0.11 (4)*
	VU154	4.59 ± 0.06 (4)	8.57 ± 0.06 (3)	6.07 ± 0.09 (7)[e]	2.43 ± 0.10 (4)	1.75 ± 0.12 (3)*
Human D432E M_4 mAChR	LY298	N.T.	8.28 ± 0.04 (5)	5.86 ± 0.07 (5)	N.T.	1.59 ± 0.06 (5)
	VU154	N.T.	8.27 ± 0.06 (6)	6.21 ± 0.12 (6)	N.T.	1.04 ± 0.09 (6)
Human T433R M_4 mAChR	LY298	N.T.	8.05 ± 0.08 (5)	5.04 ± 0.04 (5)*	N.T.	1.91 ± 0.11 (5)
	VU154	N.T.	7.88 ± 0.04 (5)	5.50 ± 0.08 (5)	N.T.	1.67 ± 0.07 (5)*
Human V91L, D432E, T433R M_4 mAChR	LY298	N.T.	7.95 ± 0.10 (4)	5.29 ± 0.26 (4)	N.T.	1.80 ± 0.22 (4)
	VU154	N.T.	7.89 ± 0.12 (4)	6.34 ± 0.16 (4)*	N.T.	1.35 ± 0.16 (4)
$G\alpha_{i1}$ activation (TruPath) interaction assays between ACh or Ipx and LY298 or VU154 on transiently expressed M_4 mAChR constructs in HEK293A cells							
Constructs	PAM	log τ ACh[f]	log τ Ipx[f]	pK_B PAM[c]	log τ PAM[f]	log $\alpha\beta_{ACh}$[g]	log $\alpha\beta_{Ipx}$[g]
Human WT M_4 mAChR	LY298	2.71 ± 0.14 (4)	1.49 ± 0.12 (4)	= 5.65	1.02 ± 0.03 (8)[e]	2.01 ± 0.14 (4)	1.96 ± 0.16 (4)
	VU154			= 5.83	-0.55 ± 0.08 (8)[e]	1.22 ± 0.13 (4)	0.20 ± 0.13 (4)
pERK1/2 interaction assays between ACh or Ipx and LY298 or VU154 on stable M_4 mAChR constructs in Flp-In CHO cells							
Constructs	PAM	log τ ACh[f]	log τ Ipx[f]	pK_B PAM[c]	log τ_C PAM[h]	log $\alpha\beta_{ACh}$[g]	log $\alpha\beta_{Ipx}$[g]
Human WT M_4 mAChR	LY298	3.27 ± 0.06 (8)[e]	1.74 ± 0.03 (16)[e]	= 5.65	1.19 ± 0.05 (12)[f]	2.29 ± 0.22 (4)	1.08 ± 0.28 (8)
	VU154			= 5.83	0.11 ± 0.05 (12)[f]	0.88 ± 0.23 (4)	0.66 ± 0.15 (8)
Mouse WT M_4 mAChR	LY298	N.T.	N.D.	= 5.74	1.32 ± 0.07 (5)	N.T.	1.24 ± 0.12 (4)
	VU154	N.T.	N.D.	= 6.07	1.47 ± 0.08 (5)*	N.T.	2.08 ± 0.15 (5)*
Human D432E M_4 mAChR	LY298	N.T.	N.D.	= 5.86	1.34 ± 0.08 (5)	N.T.	1.37 ± 0.28 (5)
	VU154	N.T.	N.D.	= 6.21	0.78 ± 0.08 (5)*	N.T.	1.02 ± 0.15 (5)
Human T433R M_4 mAChR	LY298	N.T.	N.D.	= 5.04	1.73 ± 0.13 (5)*	N.T.	1.85 ± 0.28 (5)
	VU154	N.T.	N.D.	= 5.50	0.95 ± 0.12 (5)*	N.T.	1.18 ± 0.14 (5)
Human V91L, D432E, T433R M_4 mAChR	LY298	N.T.	N.D.	= 5.29	1.62 ± 0.09 (5)*	N.T.	1.64 ± 0.30 (5)
	VU154	N.T.	N.D.	= 6.34	0.68 ± 0.06 (5)*	N.T.	1.34 ± 0.11 (5)*

Values represent the mean ± s.e.m. with the number of independent experiments shown in parenthesis. N.T. = not tested.N.D.= Not determined.

[a] Number of [^{3}H]-NMS binding sites per cell

[b] Negative logarithm of the radioligand equilibrium dissociation constant

[c] Negative logarithm of the orthosteric (pK_i) or allosteric (pK_B) equilibrium dissociation constant

[d] Logarithm of the binding cooperativity factor between the agonist (ACh or Ipx) and the PAM (LY298 or VU154)

[e] Parameter was determined in a shared global analysis between agonists.

[f] Logarithm of the operational efficacy parameter determined using the Operational Model of Agonism.

[g] Logarithm of the functional cooperativity factor between the agonist (ACh or Ipx) and the PAM (LY298 or VU154)

[h] log τ_C = logarithm of the operational efficacy parameter corrected for receptor expression (methods in Appendix 1)

* Values from pK_B PAM, log α_{Ipx}, log τ_C PAM, and log $\alpha\beta_{Ipx}$ that are significantly different from human WT M_4 mAChR ($p < 0.05$) calculated by a one-way ANOVA with a Dunnett's post-hoc test.

Table S2. Cryo-EM data collection, refinement, and validation statistics

	M4R-G_{i1}-Ipx	M4R-G_{i1}-Ipx-LY298	M4R-G_{i1}-Ipx-VU154	M4R-G_{i1}-ACh
Data Collection & Refinement				
EMD code	26099	26100	26101	26102
Micrographs	5056	5121	6021	5913
Electron Dose (e^-/A^2)	66	66	59.5	53.6
Voltage (kV)	300	300	300	300
Pixel size (Å)	0.83	0.83	0.83	0.83
Spot Size				
Exposure time	4	4	3	5
Movie frames	76	76	75	71
K3 CDS mode	No	No	No	Yes
Defocus range (μm)	0.5-1.5	0.5-1.5	0.5-1.5	0.5-1.5
Symmetry imposed	C1	C1	C1	C1
Particles (final map)	415,743	617,793	677,392	315,595
Resolution @0.143 FSC (Å)	2.8	2.4	2.5	2.8
Refinement				
$CC_{map-model}$	0.87	0.87	0.88	0.82
Map sharpening B factor ($Å^2$)	-80.9	-60.8	-46.6	-85.1
Model Quality				
PDB code	7TRK	7TRP	7TRQ	7TRS
R.M.S. deviations				
Bond length (Å)	0.004	0.004	0.005	0.006
Bond angles (°)	0.849	0.811	0.826	0.773
Ramachandran				
Favoured (%)	98.38	99.14	98.02	98.10
Outliers (%)	0	0	0	0
Rotamer outliers (%)	0.11	0.21	0	0
C-beta deviations (%)	0	0	0	0
Clashscore	2.69	2.62	2.26	4.08
MolProbity score	1.06	1.05	1.00	1.19

1681 **Table S3: GaMD simulations of the M_4 mAChR**

System	Method
M4-G_{i1}-Ipx (cryo-EM structure)	GaMD (3 x 500 ns)
M4-G_{i1}-Ipx-VU154 (cryo-EM structure)	GaMD (3 x 500 ns)
M4-G_{i1}-Ipx-LY298 (cryo-EM structure)	GaMD (3 x 500 ns)
M4-G_{i1}-ACh (cryo-EM structure)	GaMD (3 x 500 ns)
M4-D432E-G_{i1}-Ipx-VU154	GaMD (3 x 500 ns)
M4-T433R-G_{i1}-Ipx-VU154	GaMD (3 x 500 ns)
M4-G_{i1}-ACh-VU154	GaMD (3 x 500 ns)
M4-G_{i1}-ACh-LY298	GaMD (3 x 500 ns)
M4-G_{i1}-VU154	GaMD (3 x 500 ns)
M4-G_{i1}-LY298	GaMD (3 x 500 ns)
M4-VU154	GaMD (3 x 1,000 ns)
M4-LY298	GaMD (3 x 1,000 ns)

1682
1683

Table S4. Pharmacological parameters of LY298 and VU154 at key M_4 mAChR mutants.

[^{3}H]-NMS saturation binding on stable M_4 mAChR Flp-In CHO cells		
Constructs	Sites per cell[a]	pK_D[b]
Human WT M_4 mAChR (from Table S1)	598,111 ± 43,067 (7)	9.76 ± 0.05 (7)
$Y89A^{2.61}$	32,674 ± 4,174 (4)	9.88 ± 0.06 (4)
$Q184A^{45.49}$	88,728 ± 3,056 (3)	9.99 ± 0.06 (3)
$F186A^{45.51}$	36,907 ± 4,170 (4)	9.75 ± 0.16 (4)
$W435A^{7.35}$	34,861 ± 3,510 (3)	9.81 ± 0.22 (3)
$Y439A^{7.39}$	42,690 ± 4,547 (3)	8.31 ± 0.14 (3)

[^{3}H]-NMS interaction binding assays between ACh or Ipx and LY298 or VU154 on stable M_4 mAChR constructs in Flp-In CHO cells							
Constructs	PAM	pK_i ACh[c]	pK_i Ipx[c]	pK_B PAM[c]	log α_{ACh}[d]	log α_{Ipx}[d]	log α_{NMS}[e]
Human WT M_4	LY298	5.09 ± 0.07 (7)	8.54 ± 0.04 (11)	=5.65	1.57 ± 0.11	1.71 ± 0.09	= 0
	VU154	5.06 ± 0.05 (7)	8.54 ± 0.03 (11)	=5.83	1.44 ± 0.07	1.11 ± 0.06	= 0
$Y89A^{2.61}$	LY298	5.25 ± 0.05 (6)	8.48 ± 0.05 (6)	N.D.	N.D.	N.D.	N.D.
	VU154	5.27 ± 0.05 (6)	8.47 ± 0.05 (6)	N.D.	N.D.	N.D.	N.D.
$Q184A^{45.49}$	LY298	5.24 ± 0.06 (6)	8.74 ± 0.04 (10)	6.23 ± 0.06	1.28 ± 0.13	1.27 ± 0.11	-1.10 ± 0.07
	VU154	5.28 ± 0.05 (6)	8.69 ± 0.04 (10)	5.87 ± 0.17	1.07 ± 0.09	0.81 ± 0.07	= 0
$F186A^{45.51}$	LY298	4.91 ± 0.05 (6)	8.12 ± 0.05 (8)	N.D.	N.D.	N.D.	N.D.
	VU154	4.91 ± 0.05 (6)	8.12 ± 0.05 (8)	N.D.	N.D.	N.D.	N.D.
$W435^{7.35}$	LY298	3.79 ± 0.07 (7)	6.88 ± 0.07 (7)	N.D.	N.D.	N.D.	N.D.
	VU154	3.79 ± 0.07 (7)	6.88 ± 0.07 (7)	N.D.	N.D.	N.D.	N.D.
$Y439A^{7.39}$	LY298	3.23 ± 0.22 (8)	5.36 ± 0.25 (8)	N.D.	N.D.	N.D.	N.D.
	VU154	3.23 ± 0.22 (8)	5.36 ± 0.25 (8)	N.D.	N.D.	N.D.	N.D.

Values represent the mean ± s.e.m. with the number of independent experiments shown in parenthesis. N.D. = Not determined.
[a] Number of [^{3}H]-NMS binding sites per cell
[b] Negative logarithm of the radioligand equilibrium dissociation constant
[c] Negative logarithm of the orthosteric (pK_i) or allosteric (pK_B) equilibrium dissociation constant. pK_i values for ACh and Ipx are shared at each M4 mAChR construct. pK_B values for the PAMs at Q184A are shared across the agonist data sets.
[d] Logarithm of the binding cooperativity factor between the agonist (ACh or Ipx) and the PAM (LY298 or VU154)
[e] Logarithm of the binding cooperativity factor between the [^{3}H]-NMS and the PAM (LY298 or VU154)

Supplementary Video 1. 3D variability analysis of the Ipx-M_4R-G_{i1} cryo-EM structure
Supplementary Video 2. 3D variability analysis of the ACh-M_4R- G_{i1} cryo-EM structure
Supplementary Video 3. 3D variability analysis of the LY298-Ipx-M_4R- G_{i1} cryo-EM structure
Supplementary Video 4. 3D variability analysis of the VU154-Ipx-M_4R- G_{i1} cryo-EM structure
Supplementary Video 5. Movie from one Ipx-M_4R-G_{i1} GaMD simulation
Supplementary Video 6. Movie from one LY298-Ipx-M_4R-G_{i1} GaMD simulation
Supplementary Video 7. Movie from one VU154-Ipx-M_4R-G_{i1} GaMD simulation
Supplementary Video 8. Movie from one ACh-M_4R-G_{i1} GaMD simulation
Supplementary Video 9. Movie from one VU154-Ipx-M_4R(D432E)-G_{i1} GaMD simulation
Supplementary Video 10. Movie from one VU154-Ipx-M4R(T433R)-G_{i1} GaMD simulation